EXPLORING POLY(2, 5)BENZIMIDAZOLE ENHANCED WITH CARBON NANOTUBES FOR SPACE APPLICATIONS

by

Lionel Fabian Fourie

A thesis submitted in fulfilment of the requirements for the degree of

Doctor Philosophiae in the Department of Physics and Astronomy,

University of the Western Cape.

Supervisor: Dr. L. C. Square

Co-Supervisor: Prof. C. J. Arendse

December 2023

Declaration of Authorship

I declare that this thesis titled, *'EXPLORING POLY(2, 5)BENZIMIDAZOLE EN-HANCED WITH CARBON NANOTUBES FOR SPACE APPLICATIONS'* and the work presented in it are my own, that it has not been submitted for any degree or examination in any other university, and that all the sources I have used or quoted have been indicated and acknowledged as complete references.

Signed: _____

Date: December 2023
_____

i

"A lesson without pain is meaningless. For you cannot gain anything without sacrificing something else in return, but once you have overcome it and made it your own... you will gain an irreplaceable fullmetal heart."

Hiromu Arakawa

Abstract

EXPLORING POLY(2, 5)BENZIMIDAZOLE ENHANCED WITH CARBON NANOTUBES FOR SPACE APPLICATIONS

KEYWORDS: Poly(2, 5)benzimidazole (ABPBI), Carbon Nanotubes (CNT), Polymer Nanocomposites, Proton Radiation Shielding, Low Earth Orbit (LEO).

This work explores using polymeric materials for space radiation shielding in low-earth orbit. Shielding against radiation is essential on any space mission. Low atomic number materials, such as hydrogen, have shown to be effective in shielding ionising radiation. However, compared to metallic alloys, these materials suffer from relatively low mechanical and thermal properties, which limit their application. Aluminium (Al) enjoyed wide use in space applications as a structural and radiation shielding material. However, weight and secondary radiation generation issues have made its use as a shielding material less viable on modern space missions where cost and safety play a crucial role in planning these missions. On modern space missions, conventional shielding materials include Al alloys, high-density polyethylene, and water. The disadvantages include low thermal properties, high atomic numbers, and complex maintenance systems. This lead to exploring other materials that can mitigate some of these drawbacks.

A proposed approach to replacing high atomic number metals is deploying hydrogen-rich polymers enhanced with nanofiller materials to form polymer nanocomposites. Polymers enhanced with nanofillers can achieve improved physical properties while providing adequate radiation shielding functions at a lower weight with less secondary radiation generation. This forms the bases of this research. This work used poly(2, 5)benzimidazole/multi-walled carbon nanotube (ABPBI/MWCNT) nanocomposites. These were fabricated and evaluated for their proton radiation shielding capabilities in the low-earth orbit (LEO) region of space. The radiation shielding effectiveness of the ABPBI/MWCNT nanocomposites was experimentally evaluated by comparing their proton transmission properties and their secondary neutron generation to that of pristine ABPBI.

The results indicated that adding MWCNTs to the ABPBI polymer matrix further reduced the secondary neutrons generated by the pristine ABPBI. In addition, the depth profile showed that proton penetration into the bulk of the composite decreased as

iii

the MWCNT weight percentage loading increased. The MWCNT-loaded composites showed improved resistance to proton radiation-induced damage compared to the pristine ABPBI membrane. This was evident from the visible damage observed in the SEM micrographs for the pre-and post-irradiation ABPBI membranes. Furthermore, composites containing MWCNTs displayed improved thermal stability over the pristine ABPBI for both pre-and post-irradiation composites. The overall characteristics presented have shown ABPBI/MWCNT nanocomposites warrant consideration as an effective material for low-earth orbit applications in the space industry.

Acknowledgements

I extend my gratitude to the following individuals and organisations, without whom the completion of this thesis might not have been achievable:

Dr. Lynndle Square from the Centre for Space Research at NWU, for her excellent supervision, guidance, encouragement, and most importantly, her support through some of the lowest points in this journey.

Prof Christopher Arendse (UWC), who acted as co-supervisor, for his guidance and support.

To Prof. Mandla Msimanga and the wonderful team at iThemba LABS in Johannesburg your warm welcome and hospitality during the ion beam experiments made all the difference.

The staff at the Department of Physics and Astronomy your ongoing support was truly appreciated as I worked on this project.

My family, both immediate and extended, deserves a huge thank you for always being there with their support and motivation.

I can't forget to mention my friends and colleagues at UWC Siphesihle, Norman, Siphelo (Captain), and Natasha your companionship made this journey more manageable.

A special shoutout to the rest of the NWU Team, Ernst and Solly your contributions are bound to make waves in this field.

Gratitude to the National Research Foundation (NRF), the University of the Western Cape, and the North-West University for the financial support that made this study possible.

Contents

List of Figures

List of Tables

Abbreviations

A	Atomic Weight
ABPBI	Poly(2, 5)benzimidazole
Al	Aluminium
CADAR	Cluster Apparatus for Device Applications Research
CCP	Capacitively Coupled Plasma
CME	Coronal Mass Ejection
CNT	Carbon Nanotubes
DABA	3,4-Diaminobenzoic Acid
DSC	Differential Scanning Calorimetry
EEDF	Electron Energy Distribution Function
FTIR	Fourier Transform Infrared Spectroscopy
GCR	Galactic Cosmic Radiation
GEO	Geosynchronous Earth Orbit
HDPE	High-density Polyethylene
HT	High Temperature
HZE	High energy and atomic number particles
ICP	Inductively Coupled Plasma
ISS	International Space Station
LEO	Low Earth Orbit
LDPE	Low-density Polyethylene
MBU	Multi Bit Upset
MEO	Medium Earth Orbit
MSA	Methanesulfonic Acid
MWCNT	Multi-walled Carbon Nanotubes
PBI	Polybenzimidazole

PECVD	Plasma-Enhanced Chemical Vapour Deposition
PEI	Polyetherimide
PPA	Poly Phosphoric Acid
PSU	Polysulfone
RF	Radio Frequency
SEB	Single Event Burnout
SEE	Single Event Effects
SEFI	Single Event Functional Interrupt
SEGR	Single Event Gate Rupture
SEL	Single Event Latchup
SEM	Scanning Electron Microscopy
SEU	Single Event Upsets
SHE	Single Hard Errors
SPE	Solar Particle Events
SRIM	Stopping and Range of Ions in Matter
SWCNT	Single-walled Carbon Nanotubes
$\mathbf{T}_d$	Decomposition Temperature
$\mathbf{T}_e$	Electron Temperature
$\mathbf{T}_g$	Glass Transition Temperature
TGA	Thermogravimetric Analysis
TID	Total Ionising Dose
TRIM	Transport of Ions in Matter
UHMW-HDPE	Ultra-high Molecular Weight High-density Polyethylene
wt. %	Weight Percentage
XRD	X-ray Diffraction
Z	Atomic Number

Dedicated to the Fourie Family.

Chapter 1

Introduction

1.1 Background and Motivation

The outer Earth space environment is dynamic, filled with ionising radiation and other energetic particles. These radiation particles mainly stem from galactic cosmic radiation (GCR), solar particle events (SPE), and trapped radiation. The most significant challenge is protecting the astronauts and hardware in the spacecraft during space missions for extended periods[5]. Exposure to ionising radiation over long periods can lead to immediate severe or delayed health hazards on human-crewed space missions[19–21]. Moreover, ionising radiation-induced damage to the electronic components of a spacecraft, such as displacement damage (atomic displacement in a device due to collisions between the atoms in the device and the energetic radiative particles) or single event effects, is mainly irreversible[22]. Among the ionising radiation particles, protons have been identified as the primary concern in space applications due to their general density and propensity to produce secondary ionising radiation[22, 23]. A material with a high electron density can shield it against proton irradiation[23].

Another concerning member of the ionising radiation family is high energy and atomic mass particles (HZE). Current radiation shielding technologies provide little to no protection against HZEs. These particles pass through the radiation shields, unaffected, subsequently depositing their energies into bio tissues and electronic devices[24]. When shielding materials are employed to protect against these ionising radiation sources, interactions between the primary radiation particle and the atoms of the shielding materials can produce a significant amount of secondary radiation that may be more harmful. This secondary radiation is generated by nuclear reactions in atoms of shielding material due to collisions with ionising radiation. With neutrons and photons being among the types of secondary radiation generated, this generation can initiate an electromagnetic

1

cascade that could render the shielding material ineffective[23]. However, interactions between radiation and matter can vary significantly depending on the primary radiation's kinetic energy, charge, and collision angle[24, 25]. This results in small amounts of radiation seeping into the payload regardless of the type of shielding material used. Consequently, an acceptable radiation dose limit should be established for astronauts and equipment before undertaking space missions[6, 25, 26]. Thus, the selected shielding material should maintain the radiation dose as far below this limit as possible. By the principles for shielding ionising radiation[7, 27], a shielding material is considered adequate if: (1) It has a high electron density; (2) It produces fewer secondary radiations; (3) It is lightweight to reduce transportation costs. After considering these three considerations, low atomic number (low-Z) materials have attracted broader interest in space radiation shielding materials design.

Most of the radiation shielding structures and materials onboard modern spacecraft are made of aluminium (Al)[28, 29]. Widely used on the International Space Station (ISS), Al radiation shielding structures are widely considered the standard reference material for these applications as they provide adequate shielding and structural functions. For a long time, space missions were carried out by governmental agencies such as NASA. Consequently, they held the final say on the materials used in spacecraft. However, with the increased interest in conducting space activities shown by commercial (private) companies, they have invested heavily in researching and developing materials that could make space activities more profitable. Several groups in the commercial space industry are planning to deliver payloads to the ISS as part of NASA's plan to increase the number of available suborbital spacecraft[30]. Most companies signed up for this endeavour have shown long-term interest in "space tourism"[31]. The success of the private sector in this area will play a crucial role in developing the infrastructure needed for safe, reliable, and affordable commercial space travel. Moreover, since most space tourism missions are expected to be suborbital or in low earth orbit (LEO), the research into shielding materials specifically for this region of space would be extremely valuable.

In LEO, spacecraft, space stations, satellites and astronauts are subject to increased radiation levels due to energetic particles trapped by the earth's magnetic field, solar flares and GCR. Therefore, evaluating the risks associated with extended radiation exposures in this region is essential. As such, new radiation shielding materials have been proposed to help mitigate the risks of radiation exposure in the LEO environment. A class of materials with high hydrogen content, such as inorganic compounds, water, and liquid hydrogen, have been investigated as possible replacements for the conventional Al shielding material[32]. However, safety-related and feasibility issues have led to most of these materials is regarded as unusable as radiation shielding structures[33]. This

conclusion leads to the study of various polymer compounds having high hydrogen contents as possible shielding materials to mitigate the effects of radiation exposure[34]. Pure polymers such as high-density polyethylene (HDPE), which are composed of low-Z components (hydrogen), made it an attractive candidate for space radiation shielding applications[19, 25, 35, 36]. However, having poorer mechanical strength and thermal properties than its Al counterpart meant that HDPE could only be used as an associated shielding layer in conjunction with Al[37, 38]. Consequently, other advanced pure polymers such as polyetherimide (PEI), polysulfone (PSU), and polyimide were investigated for space radiation shielding applications[19, 35, 37]. Although these polymers had improved mechanical and thermal properties, they failed to provide comparable radiation shielding effectiveness to HDPE[36]. As such, in this work, we attempt to ascertain the feasibility of using poly(2, 5)benzimidazole (ABPBI) as a radiation shielding material, which inherently has better thermal and mechanical properties than HDPE. Moreover, in the works by Gaier *et al.* and Muisener *et al.*[39, 40], both groups advocate for including a nano-filler material to improve the thermal stability, mechanical strength, radiation resistance, and shielding effectiveness of the underlying polymer matrix.

Various nano-filler materials were proposed in their work. However, a consensus was reached that carbon based filler materials, specifically carbon nanotubes (CNTs), warrant more investigation in radiation shielding applications. This stems from the CNTs having high mechanical and thermal properties and a negative coefficient of thermal expansion[41]. Studies by Li *et al.* and Najafi *et al.* have shown evidence of enhancement of a polymer's proton and electron shielding efficiencies by adding CNTs into its polymer matrix [26, 42]. They also found that CNTs with multiple walls provided increased stability to radiation-induced damage, which advocates for using multi-walled carbon nanotubes (MWCNTs).

Adding CNTs, or MWCNTs, to a polymer matrix forms a class of compounds known as nanocomposites. These nanocomposite materials are known for having the desired mechanical and thermal properties required for consideration as a radiation shielding material. However, compared to metallic counterparts such as Al, polymer-based nanocomposites cannot perform as stand-alone radiation shielding structures due to their poorer mechanical integrity. These can, at the very least, be used as an associate layer of the radiation structure that can significantly increase the shielding effectiveness of the structure at a greatly reduced weight.

In this work, the polymer poly(2, 5)benzimidazole (ABPBI) is reinforced with multi-walled carbon nanotubes (MWCNT) to form ABPBI/MWCNT nanocomposites. To date, polymer-based multifunctional nanocomposites for radiation shielding applications have garnered limited attention from researchers. However, with this work, we would like

to emphasise the potential of polymer nanocomposites as radiation-shielding materials. The ABPBI/MWCNT nanocomposites are evaluated for their proton radiation shielding effectiveness in the LEO environment.

1.2 Research Scope

This work focuses primarily on exploring the possibility of using the poly(2, 5)benzimidazole reinforced with multi-walled carbon nanotubes (ABPBI/MWCNT) polymer composite as a proton radiation shielding material in the low earth orbit (LEO) environment. Summarised in this section are the objectives of the research work.

1.2.1 Polymer and Polymer nanocomposite fabrication

This study aims to ascertain the compatibility of the MWCNTs with the polymer matrix of ABPBI through the fabrication of polymer nanocomposite membranes. Pristine, 1% and 3% ABPBI/MWCNT membranes were fabricated, and their properties were compared. Through characterisation, these composites' chemical, compositional, thermal, and mechanical properties are compared to determine the degree to which the addition of MWCNTs has improved the properties of the underlying polymer matrix of ABPBI. The thickness of the ABPBI/MWCNT nanocomposite membranes was then optimised to determine the minimum thickness required to shield against the most commonly occurring proton energies in the LEO environment. With the completion of the thickness optimisation, pristine ABPBI and ABPBI/MWCNT membranes were fabricated for the proton radiation shielding tests.

1.2.2 Proton Radiation Shielding Tests

Proton radiation shielding tests of the polymer composites were performed at the iThemba LABS (Johannesburg) particle accelerator facility. The polymer membranes are exposed to a 5 MeV proton beam to determine their effectiveness at shielding against proton irradiation. With this, the polymer composites' secondary radiation generation, specifically neutron generation, was determined and discussed. The effects of proton irradiation on the composites were determined through characterisation following the irradiation processes. Details of the achievements of this study have been discussed accordingly.

1.3   Thesis Outline

This thesis contains seven chapters:

- Chapter 1, the introduction, provides an overview of the research background and introduces the motivation and scope.

- Chapter 2 is the literature review, overviewing the space radiation environment. Also, an overview of the ionising radiation shielding principles is provided with an overview of conventional radiation shielding versus nanocomposite materials.

- Chapter 3 provides an in-depth look into synthesis methods for fabricating the poly(2, 5)benzimidazole membranes used in this work. Also given in this chapter is a brief overview of the characterisation techniques used to analyse the polymer membranes.

- Chapter 4 presents a computational study of a plasma-enhanced chemical vapour deposition system for producing carbon-based films. With this, we attempt to ascertain the system's feasibility in producing the multi-walled carbon nanotubes used in this study.

- In Chapter 5, poly(2, 5)benzimidazole and poly(2, 5)benzimidazole/multi-walled carbon nanotube composite membranes are fabricated, evaluated and compared for their chemical, compositional, thermal, and mechanical properties.

- Chapter 6 illustrates the proton shielding capabilities of the nanocomposites as well as their secondary neutron attenuation proficiencies.

- Chapter 7 highlights the significant findings and gives recommendations for future work.

Chapter 2

Literature Review

2.1 Space Radiation

2.1.1 Radiation Sources

The radiation environment in space is mainly comprised of electrons, protons, solar particle events (SPEs), and galactic cosmic radiation (GCR), which are all extremely hazardous during space travel. The three primary sources of radiation in space are shown in Figure 2.1.
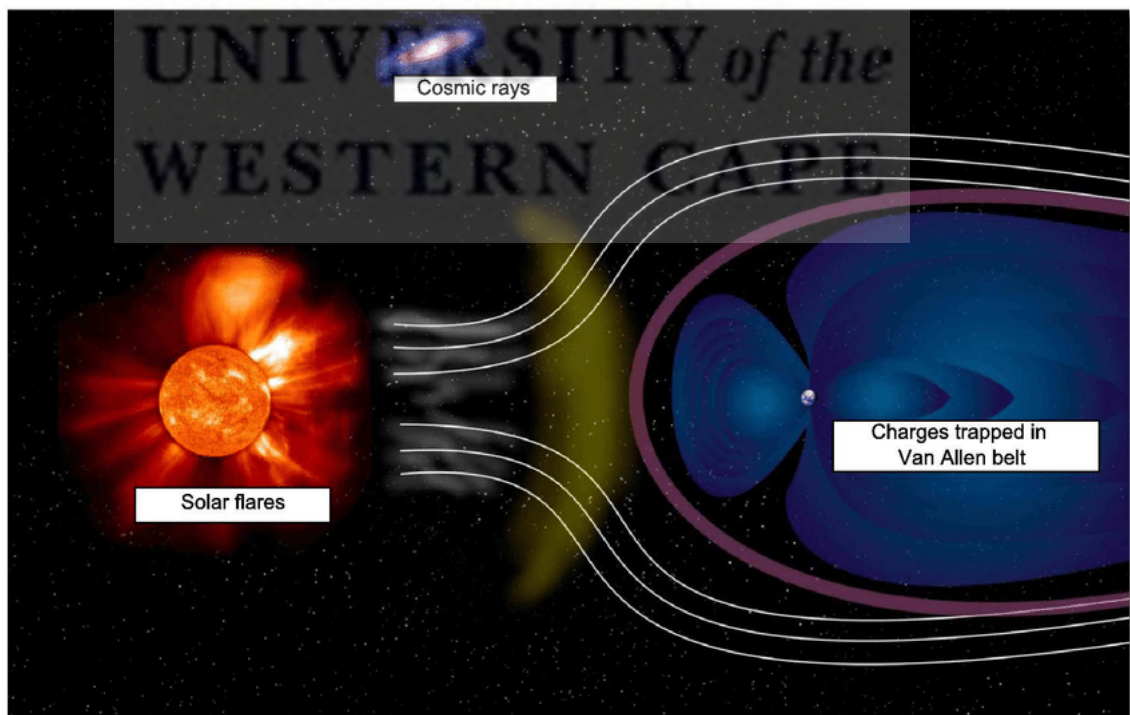
FIGURE 2.1: Radiation sources in space[1].

SPEs are events containing a vast number of high-energy charged particle from the Sun per unit of time[43]. These originate from solar flare sites or through shock waves associated with coronal mass ejections. The GCR comprises high-energy charged particles originating in outer space from supernovae of massive stars and active galactic nuclei. The GCR comprises primarily nuclei, or fully ionised atoms, with a small contribution ($\approx 2\%$) from electrons and positrons[44]. The remaining 98% of the particles in GCR are baryons, 85% are protons, 14% are α particles, and around 1% are high-energy and atomic number particle (HZEs). HZEs consist of ions with atomic numbers between 3 and 28[23, 45]. GCR particles are primarily positively charged and interact with materials mainly through Coulomb interactions with the negative electrons and positive nuclei in the materials and, to a lesser extent, through collisions with atomic nuclei in the materials. The energies of GCR particles range between 10's of MeV to 10's of GeV while their flux is affected by solar activities and Earth's magnetic field in low earth orbit (LEO). In LEO, the flux of GCR particles received by spacecraft reaches a maximum near Earth's poles due to the magnetic field lines drawing particles toward the Earth. Conversely, the flux is minimal near the equator, where particles travel parallel to the Earth. Figure 2.2 shows the energy spectrum of GCR particles in solar minimum and maximum.
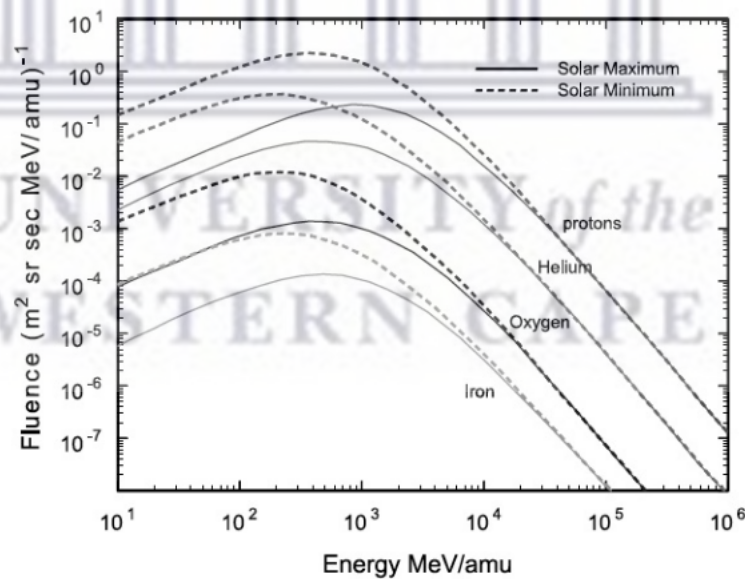
FIGURE 2.2: Energy spectrum of GCR in a solar maximum and minimum[2].

As mentioned, three main types of SPEs exist; coronal mass ejections (CME), solar flares and solar winds. CMEs are a result of matter eruptions from the sun. This matter is composed of high-energy plasma containing mainly protons and electrons. However, small amounts of HZE particles, like Iron (Fe) with atomic number 26, are also ejected during CME along with electromagnetic radiation. These ejections reach

speeds ranging between 20 km/s to 3200 km/s, with an average speed of around 489 km/s[6]. The duration of CME is in the order of days and is defined by the release of large fluxes of protons (10^9/cm^2) with a broad angle in solar longitude[46]. Solar activities are observed in 11-year cycles with maximum and minimum solar phases[5]. During a solar maximum, SPEs and solar flares are always detected. Solar flares occur suddenly, release energy up to 6.4x$10^3$8 MeV, and occur in active regions of the sun around sunspots [46]. They typically last a few hours and are defined by relatively large fluxes of electrons (10^7/cm^2 to 10^8/ cm^2) [47]. Compared to CME and solar flares, solar winds are always present in the solar system and consist of protons and electrons with energies ranging from 1.5 to 10 keV[48].

When protons and electrons from GCR and SPEs interact with the Earth's magnetic field and atmosphere, the most energetic particles are trapped, forming the Van Allen Radiation belt, see Figure 2.3.
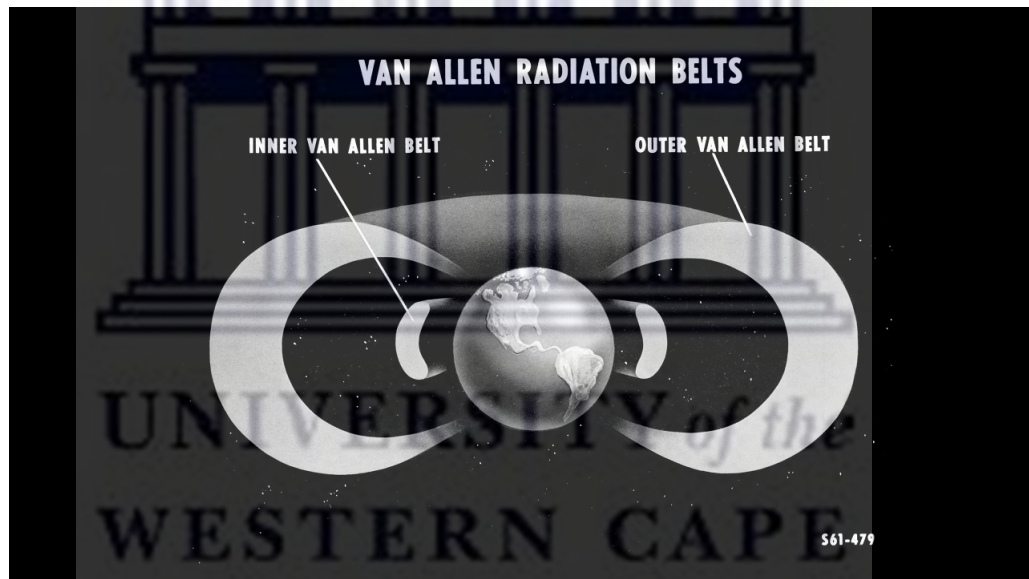
FIGURE 2.3: Van Allen Radiation Belt[3].

The outer Van Allen Radiation belt ranges from 13 000 km to 60 000 km above the earth's surface. The particles found here are mainly electrons. The inner belt ranges from 100 km to 10 000 km above the ground, with the particles found here primarily being protons and electrons. Electron energy ranges from 5 MeV in the inner belt to 7 MeV in the outer belt. The intensity of trapped protons decreases as a function of altitude above the earth's surface. The energies of these protons can go up to several hundreds of MeV; however, the most intense fluxes occur at energies lower than 10 MeV, which have been shown to contribute most to the absorbed radiation dose[49]. Figure 2.4 shows the integral fluxes for protons and electrons as a function of particle energy for the Van Allen Radiation belts.
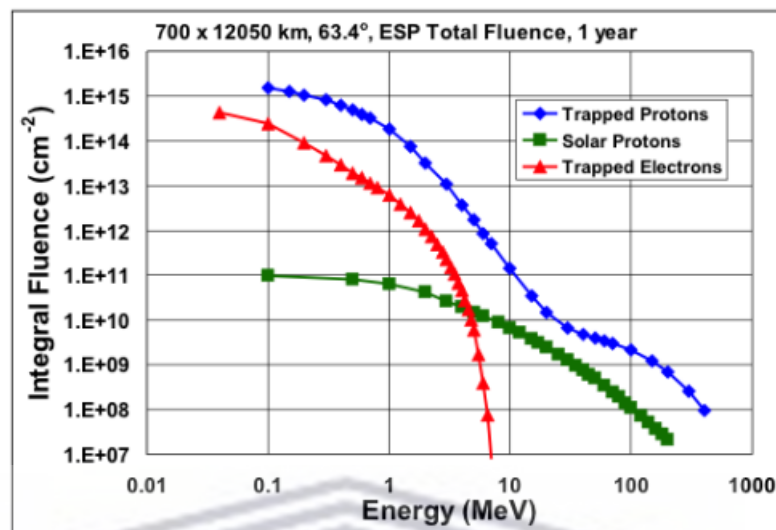
FIGURE 2.4: Proton and electron flux as a function of energy[4].

A good understanding of the radiation sources in the space environment plays an essential role in selecting effective shielding materials. Along with understanding the types of particles in the application region, it is also vital to know the factors that give rise to this radiation and the energy ranges you can expect to plan for any anomalies. In the following sections, we will look at the radiation environment to further understand the nature of the anticipated types of radiation.

2.1.2 Radiation Environment

Although several planetary landing missions have been conducted in recent history, the most visited regions of space remain the area immediately surrounding Earth. The orbital regions around Earth can be subdivided into smaller areas based on their proximity to the Earth's surface. These are low earth orbit (LEO), medium earth orbit (MEO), and geosynchronous earth orbit (GEO).

2.1.2.1 LEO

LEO ranges between the earth's surface to approximately 2000 km above the ground. A majority of the current spacecraft will be found orbiting in this region. Predominantly found in LEO are protons trapped in the inner Van Allen Radiation Belt with a radiation dose rate of around 1 mSV/year[50]. The proton flux in LEO varies according to the change of inclination and altitude of the spacecraft orbit. Rapid increases in proton flux are observed for inclinations between 0° and 30°, while for inclinations between 30° and

60°, a more gradual increase in proton flux is observed [51]. For orbit altitudes between 200 and 600 km above ground, the proton flux increases drastically with amplitude, while after the 600 km mark, the proton flux stabilises [47, 52]. For context, the International Space Station (ISS) mostly orbits at an altitude well within the inner radiation belt (320 to 400 km). However, when the ISS travels over the South Atlantic region, more than half the radiation absorbed by the ISS is due to trapped protons in the inner radiation belt stemming from an abnormal drop in the geomagnetic field [53]. These trapped protons typically have energies comparable to those commonly found in the outer radiation belt. To avoid prolonged exposure to the effects of trapped protons, the orbital altitudes of the ISS are pre-emptively adjusted. In LEO, electrons typically have energies up to 7 MeV, while most protons found in LEO have energies less than 10 MeV [53]. Protons with energies between 10 and 500 MeV only constitute a relatively small percentage of the proton energy spectrum in LEO. With the ISS being arguably the most famous spacecraft to orbit in this region, extensive documentation is kept on the radiation mixture and dose received by the ISS during its orbit. Figure 2.5 shows the 11-year integral fluence versus particle energy experienced by the ISS through its orbit.
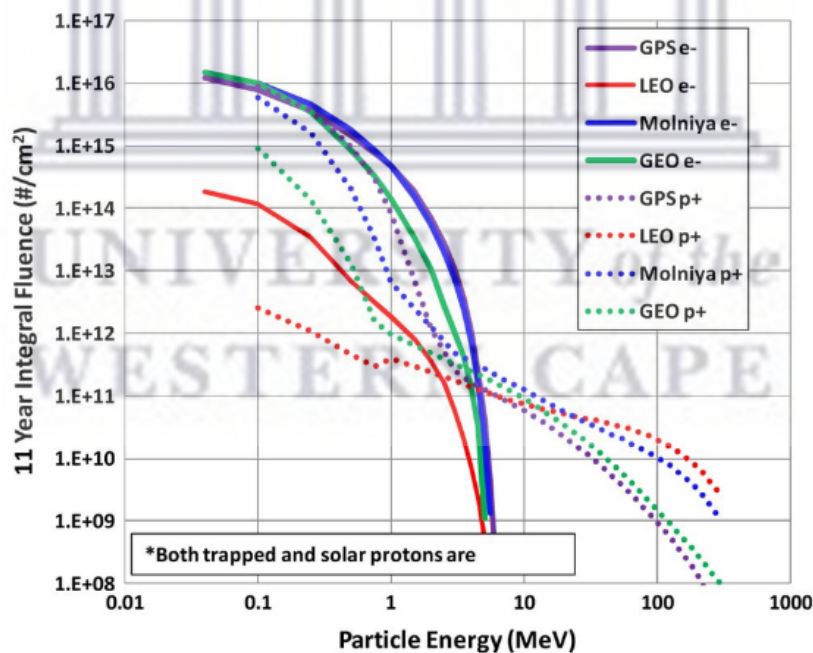
FIGURE 2.5: Proton and Electron energy spectrum for the orbit of the International Space Station [5]

For protons, from Figure 2.5, it is evident that proton flux decreases as proton energy increases, subsequently showing the abundance of protons with energy less than 10 MeV. This observation plays a key role when designing ground based experiments for the LEO region of space.

2.1.2.2 MEO and GEO

The MEO and GEO constitute the other regions that makeup what is classified as Earth's orbits. MEO ranges from 2000 km (the maximum boundary of LEO) to around 35 786 km above the earth's surface. This region is commonly home to geographical positioning satellites which lie between the upper and lower Van Allen belts. In a study by Gerald *et al.* [52], they reported that the radiation environment in MEO depends greatly on the altitude and inclination of the spacecraft, with the dose rate from protons and electrons of around 1 Sv/year.

The geostationary (or geosynchronous) orbit (GEO) is the outer orbit, above 35 786 km. In GEO, orbiting satellites remain stationary over a single line of longitude. These satellites get exposed to the outer Van Allen Radiation Belt, where the trapped protons from cosmic rays and solar flares can supply radiation dose rates of around 0.1 Sv/year[47]. Data from early NASA missions showed that the radiation dose encountered by spacecraft could range between 110 to 1270 μGu/day in LEO compared to 10.3 to 1154 mGu/day in GEO [54]. Although various advanced materials have been used in radiation shielding applications in these regions, Center *et al.*[55] have reported that satellites and crews in spacecraft can still receive different types of radiation ranging from 80 to 160 mSv/six-months, much higher than the 2 mSv/year they would receive on earth.

2.1.3 Effects of Space Radiation

The effects of space radiation exposure on astronauts and spacecraft payloads are determined by the type of radiation exposure, the radiation energy level, the absorbed radiation dose, and the exposure time[20]. These factors, among others, are directly related to the amount of damage radiation can induce during space activities. The radiation-induced damage experienced by spacecraft can be broadly classified into two general categories; ionising damage and non-ionising, or displacement, damage[30].

Non-ionising radiation damages tissue and materials through the production of atomic displacement. This radiation is especially damaging to electronics on spacecraft as they produce stable, long-term changes in device and circuit characteristics that result in degradation and functional failure of these devices. Non-ionising radiation is also known for producing health risks such as carcinogenesis, cardiac problems, and other acute radiation syndromes[19]. Although non-ionising radiation carries major risks related to its exposure, shielding against non-ionising radiation is a relatively simple endeavour. Since this kind of radiation does not have sufficient energy to ionise atoms, the energy of the

non-ionising radiation is converted to heat[6]. Materials with good thermal properties can therefore be used to mitigate these effects by absorbing the radiation and dissipating the heat generated without heating the underlying structure [56].

While carrying similar health and safety risks as non-ionising radiation, ionising radiation is much more difficult to shield against. In general, ionising radiation consists of heavy ions and high energy particles that may produce immediate or delayed health concerns. The risk factors for spacecraft electronics associated with ionising radiation often pose mission-critical problems. As most orbital spacecraft rely heavily on solar energy, the damage caused by ionising radiation by creating electron-hole pairs in semiconductors can lead to catastrophic power failures on spacecraft. However, solar panel arrays are not the only component of the spacecraft that uses semiconductor materials. The ionising radiation effects on semiconductors can be classified into two major categories: total ionising dose (TID) and single event effects (SEE). TID causes device degradation due to accumulated effects of ionising radiation over the exposure time, whereas SEEs are transient or permanent effects due to a single particle. Table 2.1 summarises the space environment's primary effects on these devices[30].

TABLE 2.1: Effects of the Space Radiation Environment on Semiconductor Devices.

Radiation Source	Particle Type	Primary Effect on Devices
Trapped Radiation Belts	Protons	Ionising damage.
	Electrons	SEEs in sensitive devices.
Galactic Cosmic Radiation	High-energy Charged Particles (ions)	Single Event Effects (SEE).
Solar Flares and CME	Protons	Ionising damage.
	Electrons	SEEs in sensitive devices.
	Lower-energy heavy-charged particles	Single Event Effects.

The single event effects can arise either directly from the ionising particles or secondary particles generated from the interaction of the primary ionising particle with the material[57]. An example would be protons interacting with metallic materials and producing secondary neutrons. SEEs are generally classified into two categories: soft errors and hard errors. Soft errors usually appear as a bit flip in memory and do not permanently affect the device's functionality. Hard errors are destructive and can be temporary; however, these tend to cause permanent damage to the device. Among the various SEEs, Single Event Upsets (SEU) are important to note. SEUs are radiation-induced errors in microelectronic circuits caused when charged particles, usually from the radiation belts or GCR, lose energy by ionising the medium through which they pass, producing electron-hole pairs that damage digital, analogue, and optical devices [30]. Other SEEs include: Single Hard Error (SHE), Single Event Functional Interrupt (SEFI), Single Event Latchup (SEL), Single Event Burnout (SEB), Single Event Gate Rupture (SEGR), and Multiple Bit Upset (MBU).

Non-ionising radiation produces relatively stable, long-term device changes and circuit characteristics that may cause parametric degradation and functional failure. Non-ionising energy loss results in displacement damage and defects in semiconductor and insulator regions. Non-ionising radiation can also damage materials and tissue by producing of atomic displacements. As this work focuses more on the effects of ionising radiation, displacement damage caused by non-ionising radiation won't be discussed in detail. However, a more detailed description of displacement damage can be found in the work done by Beck *et al.* [56].

Understanding the space radiation environment's effects on both biological and electrical materials is a good risk assessment standard. Combining this with the knowledge of space radiation sources assists with selecting appropriate shielding materials to help mitigate these mission-critical risk factors. The following section examines the principles regarding shielding against ionising radiation.

2.1.4 Shielding Principles for Ionising Radiation

In conventional radiation protection, three principles apply: (1) minimising the duration of exposure; (2) maximising the distance to the radiation source; (3) placing shielding between personnel and the radiation source whenever possible[58]. However, these three principles are difficult or impractical to apply on human-crewed space flights. The first principle is inoperable due to the general duration of non-commercial (private) space activities. The second principle can only be applied to ground based radiation sources as, in space, the radiation source is omnipresent. The third and final principle is utilising a shielding material against ionising radiation to mitigate exposure. Radiation particles such as protons and high-atomic number element radiation (HZE) contribute the most to the absorbed radiation dose in space activities[24].

Moreover, due to the use of high-atomic number (high-Z) materials on components of the spacecraft, secondary radiation generation, which include electrons and neutrons, becomes a shielding concern. An effective radiation shielding material can be designed by knowing the particle mixture and understanding the physical principles required to shield against these particles. In this section, we explore the main particles of concern and give an overview of the principles related to shielding against these radiation types.

2.1.4.1 Protons

Protons are positively charged particles with masses 1000x greater than an electron. The nucleus of an atom only occupies 10^{-5} of its volume; therefore, when protons pass

through matter, direct collisions between the protons and the nucleus are rare. As such, most of the incident proton's energy is lost by ionisation and excitation of atoms through interactions with electrons. Consequently, the material's electron density is essential when shielding against proton radiation[27]. To effectively shield against protons, the shielding material should have a sufficient electron density, maximise the probability of projectile fragmentation, and minimise the shielding atom's fragmentation [59].

The electron density is defined as[60]:

$$N_e = \rho N \frac{Z}{A}.$$ (2.1)

Where ρ is the material density, N is Avogadro's number, Z is the atomic number, and A is the atomic weight. In Equation 2.1, we see that the electron density is determined by a material's density and the ratio $\frac{Z}{A}$. For space applications, materials should be as light as possible. For cost consideration, the mass density should be low. Hence, the factor $\frac{Z}{A}$ is an important ratio to consider when shielding against protons. The higher this ratio, the more efficient the element's shielding capabilities. A comparison of the $\frac{Z}{A}$ ratio as a function of atomic number is presented in the figure below. From Figure 2.6, we find that hydrogen has the highest $\frac{Z}{A}$ ratio, which is more than 50% higher than other atoms presented in the figure, this implies that hydrogen is the most effective at shielding proton radiation.
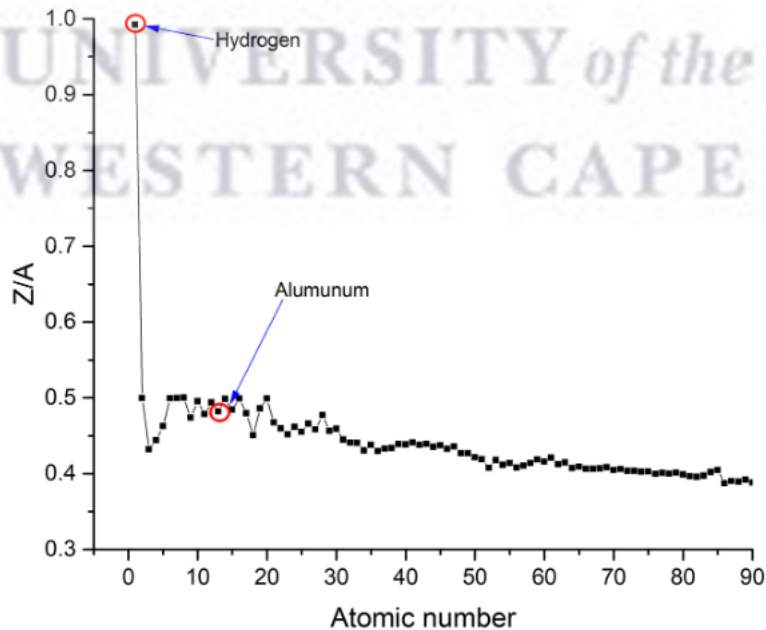
FIGURE 2.6: Calculation of Z/A for atoms with atomic number Z from 1 to 90[6].

The second consideration regarding shielding protons is maximising the probability of projectile fragmentation and minimising the shielding atom's fragmentation. Protons lose most of their energy through interactions with electrons; however, nuclear reactions can occur between the incident protons and the nuclei of the shielding material when the incident proton has a sufficiently large kinetic energy. The Bradt-Peters equation can be used to approximate the nuclear interactions as[38]:

$$\sigma = \pi r_0^2 c_1(E)(A_P^{\frac{1}{3}} + A_T^{\frac{1}{3}} - c_2(E))^2 \tag{2.2}$$

where σ, the total fragmentation cross-section, is proportional to $A_T^{\frac{1}{3}}$, the atomic mass of the shielding material. From Equation 2.2, we see that the lighter the material is, the smaller nucleus, the more nuclear reactions will occur, increasing the effectiveness of shielding against proton radiation. However, this results in generating a cascade of secondary emissions, such as electrons, light ions, gamma rays, and neutrons, from nuclear collisions of the incident protons with shielding material[38]. Since the generation of secondary emissions is unavoidable when shielding protons, the material should have some capabilities of attenuating these secondary emissions.

2.1.4.2 Electron Shielding

Similarly to other heavy charged particles, Coulomb interactions play a crucial role when electrons pass through matter. Compared to positively charged ions, when electrons collide, they do so in an elastic manner that can produce a cascade of scattering events. An electron with energy > 10 keV has a more significant energy loss per collision event. Subsequently, these electrons have a longer range and lower ionisation density in the shielding material than their positively charged counterparts[61].

For low-energy electrons, Coulomb interactions between the positively charged nucleus of the shield and the electrons result in the production of secondary photons. The energy of the photons greatly depends on the atomic number (Z), scattering angle, and incident energy of the electrons. The probability of energy loss due to the production of photons strongly depends on Z as well. This is illustrated in Equation 2.3[62].

$$\frac{Z_{radiative}}{Z_{electronic}} \approx \frac{ZE}{800MeV} \tag{2.3}$$

$Z_{radiative}$ is the radiactive energy loss, $Z_{electronic}$ is the collision energy loss, and E is the electron energy in MeV. Equation 2.3 indicates that high-Z materials (Z = 80-90) produce a larger quantity of photons low low-Z materials. These low-Z materials mainly

stop high-energy electrons (10-100 MeV) through ionisation[62]. Consequently, high-Z materials achieve better attenuation of electron energy as more energy is deposited into the material (through collisions) and carried away through secondary radiation production. As such, less electron attenuation is expected for low-Z materials but with significantly less secondary radiation generated[54]. As proposed in works by Najafi *et al.*[42], Saxen *et al.*[63], and Sharif *et al.*[64], to effectively shield against electron radiation, the material used should adopt the characteristics of both high-Z (high stopping power) and low-Z (fewer secondary emissions) materials into one composite material.

2.1.4.3 Secondary Radiation Shielding

As previously mentioned, secondary radiation produced when protons interact with matter can be more harmful than the protons themselves. In particular, produced neutrons are difficult to shield against due to their electro-neutrality, which means they are unaffected by an electric field and can, uninhibitedly, deliver high radiation doses to the spacecraft's occupants and components. A two-step process is implemented for neutron shielding applications[59]. The first step requires the fast neutron to be slowed down to thermal energies (around 0.025 eV[26]). Light elements, such as hydrogen, is used to achieve this in the shielding material. Hydrogen is effective due to a maximum energy transfer from the neutrons to the nucleon of hydrogen during the collision process. Furthermore, the risk of producing more secondary neutrons is mitigated with the nucleus of a hydrogen atom not containing any neutrons. However, hydrogen has limitations in its implementation, which are discussed later in this chapter.

Heavier elements were investigated that can provide effective neutron radiation shielding due to the limitations that arose from the use of hydrogen. Turner *et al.*[7] provides the principles on which these materials are evaluated: Suppose the energy, Q, is transferred to a nucleus of mass, m, in a single elastic collision with a neutron of mass, M, and neutron energy ,E_n, Equation 2.4 is used to describe the relation between Q and E_n.

$$Q = \frac{mME_n}{(M + m)^2} \tag{2.4}$$

From the relation in Equation 2.4, with a neutron having an atomic mass of 1 (M=1), we see that only when $m = 1$ (as is the case for hydrogen) can maximum energy be transferred during the collision process. Also, by increasing the mass m, the energy transferred decreases exponentially, effectively advocating using hydrogen or hydrogen rich materials.
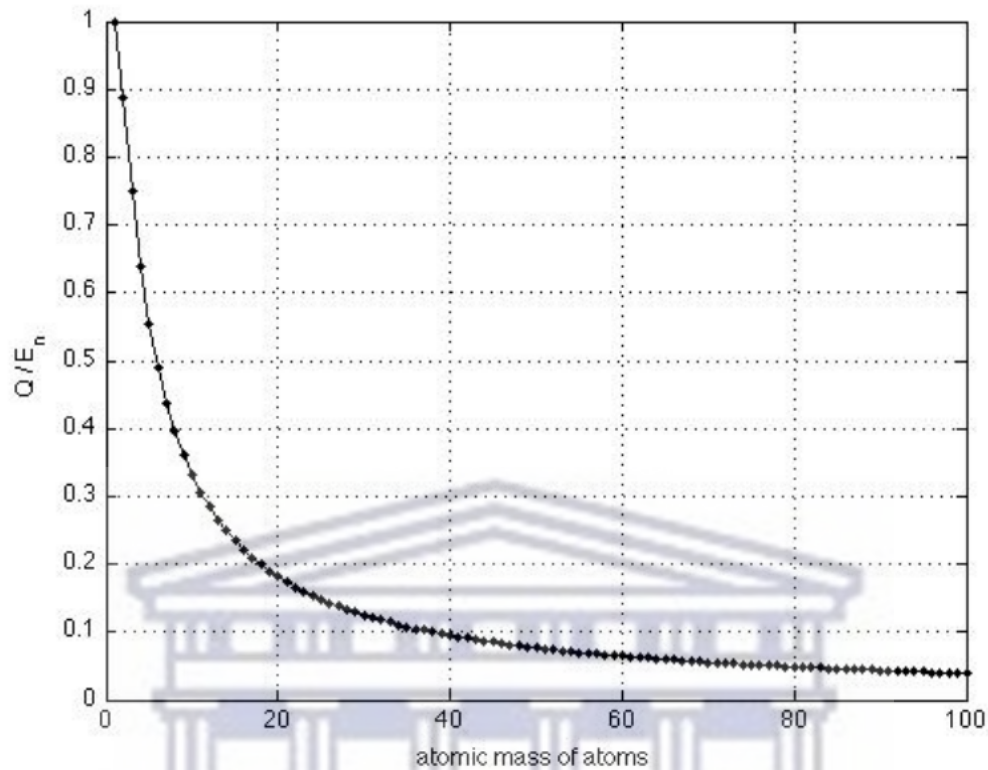
FIGURE 2.7: Q/E_n vs atomic mass[7].

In the second step, once the neutrons have reached thermal energies, they must absorbed. This is achieved using materials with high thermal neutron capture cross-sections. In work done by Carron *et al.*[65], they could show all the stable isotopes with relatively high thermal neutron capture cross-sections. From this, they discovered that all isotopes with the required thermal capture cross-section produced gamma rays during the collisions with neutrons. Effectively, an extra layer or material would be required to mitigate photon radiation production. In comparison, isotopes like B_{10}, He_3, and Li_6 have been shown to capture thermal neutrons while producing no gamma-ray emissions effectively [65, 66].

2.2   Conventional Shielding Materials

To maintain the normal operation of onboard spacecraft electronics and ensure the health of astronauts' on manned missions to space, materials have been developed that can effectively shield against space radiation[67, 68]. In this section, we discuss the conventional materials, Aluminium (Al) and its alloys that currently enjoy widespread use as a radiation shielding material.

2.2.1 Aluminium and Aluminium Alloys

Al and its alloys are the primary structural material for space applications. These include satellites, spacecraft, and launch vehicles. Al is lighter and can endure equal amounts of stress during launch and operation than its heavier metallic counterparts. Consequently, using Al in this regard significantly decreases the payload's weight, reducing the space mission's overall costs. Al has enjoyed use on many famous missions to space, including The Apollo missions, Skylab and the International Space Station (ISS). Following the Apollo missions, Al alloys such as Al 2219-T87 and Al 6061-T6 still form a significant part of shields, radiation or structural, on modern spacecraft and satellites for their high mechanical strengths[69].

New alloys and modified materials have recently emerged to replace the conventional Al 2000, 6000, and 7000 series of alloys[70]. These include; low-density aluminium-lithium alloys, powder processed 7000 series alloys, aluminium-based MMCs, and metal-polymer hybrid composites[6]. The incremental increase in yield strength of the Al alloys is shown in Figure 2.8.
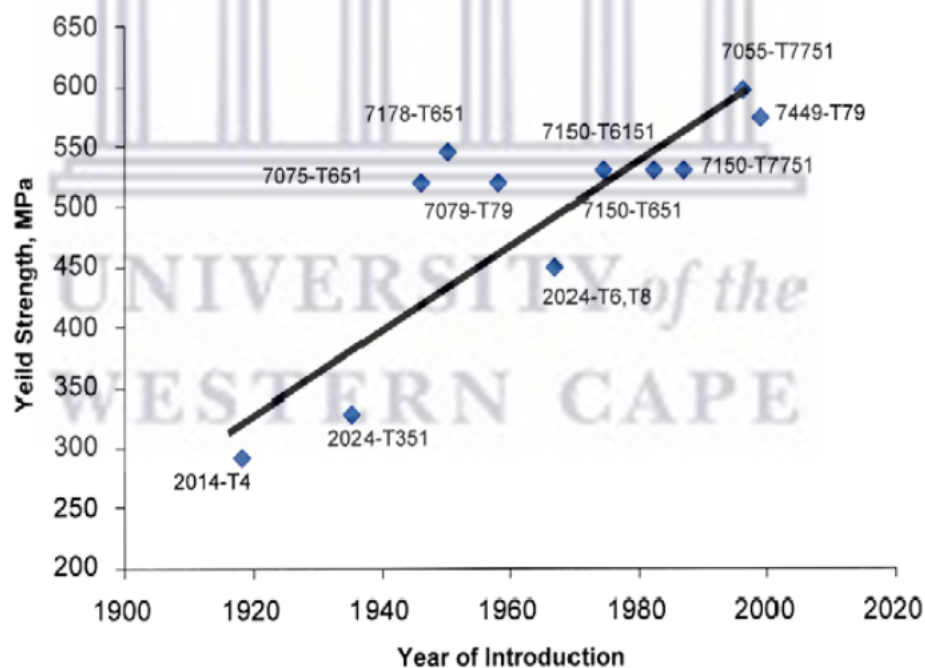
FIGURE 2.8: Plot of yield strength for new Al alloys as a function of the year of introduction[8].

Regarding radiation shielding, Al and its alloys have been the industry standard for several years[29] with their shielding effectiveness having been vastly studied specifically for space applications[37]. Generally, 2 - 5 g cm^{-2} of Al is explicitly used as radiation shielding walls on spacecraft[28]. However, 20 g cm^{-2} of Al is used on several parts of the ISS as an effective shield to protect certain mission-critical payloads. These denser

sections can stop proton radiation between 100 to 200 MeV entirely. Therefore, this shielding can effectively shield the ISS against trapped radiation and SPE.

However, Al suffers from high weight due to its high atomic number. This produces more secondary radiation particles than low-Z materials. The disadvantage of having this high weight is the increased costs of the space mission and the shorter duration stemming from the extra fuel consumption. Some of the secondary radiation produced by the interaction between protons and the metallic atoms of Al include photons, electrons and neutrons. These secondary particles cause further damage to onboard electronics and incur extra radiation doses for astronauts on manned missions.

2.3   Alternative Shielding Materials

The last decade has seen a rise in interest from private (commercial) companies to conduct space activities separate from their national space agencies. With this rise in commercial interest came the need to find materials that can effectively replace Al as a radiation shielding material, primarily for reducing costs associated with space activities. These alternative radiation shielding materials should at least provide an equal or improved radiation shielding function compared to the Al it will be replacing. This section will discuss the five main criteria these alternative materials must satisfy to garner consideration for this application.

2.3.1   Thermal Properties

Some of the main heat sources on a spacecraft are batteries, photovoltaic cells, thermal control systems, scientific equipment, etc. Along with these, depending on the orbital position, the spacecraft and its electronic components can be exposed to direct sunlight 25% stronger than on the ground[71]. In the LEO environment, the spacecraft also experiences extreme temperature fluctuations ranging between 60 and -150°C over a 90 minute period.

A solution to temperature control problems is having excellent thermal design to protect equipment from damaging temperature fluctuations. Presently, spacecraft are designed with thermal control systems that regulate temperatures to ensure optimal conditions are maintained for both the astronauts and the onboard electronics. Every non-inert system must dissipate heat to the environment, as continual thermal buffering is impractical over the long term. Consequently, the thermal control system ensures that the spacecraft operates optimally. However, since these systems technically form part of a spacecraft's

electrical components, they are also susceptible to failure due to exposure to ionising radiation. As such, it is essential to have a material that can effectively transfer heat away from mission-critical components. Moreover, having a single material that can both serve as this heat shield and radiation shield can significantly reduce the overall weight of the spacecraft.

Heat transfer, the energy transmission process via energy carriers, can occur several ways. Generally, there are three main modes: convection, conduction, and radiation[72]. In solids, convection and conduction are the main modes of heat transfer in which phonons and electrons are the energy carriers.

In polymeric materials, phonons, photons, and electrons can transport energy. However, due to the insulating properties of polymer plastics, their electrons cannot move freely within their structure. Hence, phonons play a vital role in heat dissipation[73]. Pure polymers are well known for having low thermal conductivity[74]; it is, therefore, important to enhance this characteristic of the polymer matrix before implementation as a shielding material. This will help maintain the material temperature to within its designed working temperature.

2.3.2   Light-weight

Light-weight materials are essential in reducing fuel costs as fuel can be significantly conserved for each payload. For the functional structures on the spacecraft, such as the radiation shielding component, being lightweight would allow more mission-critical devices to be added to the payload. A function-to-weight ratio is considered when evaluating a material regarding weight requirements. Consequently, the higher the ratio, the lighter the material will be while achieving the same level of radiation-shielding function. An excellent example of this is hydrogen. Hydrogen is the most effective radiation shielding element; however, its applications in space are limited. This is due to difficulties with its processing, the difficulty of compressing it into either a solid or liquid form, and the heavy equipment required to contain it. These limitations lead to the use of Al as a shielding material. Consequently, the material used to replace the conventional Al shielding should have a relatively high function-to-weight ratio. Polymeric materials have an advantageous weight property; however, the radiation shielding function should be established before consideration for its implementation.

2.3.3 Long Lifetime

Under harsher orbital conditions, many materials, including polymers, may be able to maintain the properties that make them attractive candidates for replacing the conventional Al shielding material. Besides being light-weight, alternative shielding materials should also have a relatively long service life. Consequently, an effective radiation shielding material should not only be able to attenuate radiative particles but also possess a strong resistance to radiation-induced damage. A material with high radiative degradation would not be a reliable shield for long-term space missions.

Different forms of radiation have different damage effects on the polymers. These include breaking and cross-linking of polymer chains, micro-cracking within the molecular network, and mass loss[75]. All these can alter the polymer's properties and degrade the material's performance. Therefore, inspecting the prospective materials' structural and compositional properties post-irradiation is crucial to identify any changes that could affect their service life.

2.3.4 Low Cost

As mentioned previously, materials that are heavy and possess short service lifetimes can add considerably to the overall expenditure of these space missions. This is due to having to periodically run maintenance missions to either to replace these materials or replenish fuel aboard the spacecraft. Implementing the first three parameters mentioned above minimises or removes the need for these maintenance missions, reducing expenditure.

Another key facet of cost reduction is the cost of material fabrication. In general, polymers and polymer composites are inexpensive and relatively easy to fabricate at any scale without needing specialised equipment[76, 77], making them attractive for applications on space missions.

2.3.5 Material Compatibility

Some shielding materials are required to protect substrates or devices against ionising radiation. For an alternative material to be considered in this regard, it should have a good adaptability and compatibility with the structure or device it protects. In this way, the structure or device can still perform its functions uninhibited by the material. As such, the compatibility of the material with the structure it would be shielding against ionising radiation needs to be evaluated and understood before its application.

2.4 Nanocomposites for Space Radiation Shielding

Per radiation shielding principles, there are four main criteria a material should satisfy to be considered an effective radiation shield. These are: It must have a high electron density to increase the electromagnetic interaction between target electrons and the incident particles, it produces fewer secondary radiation particles, it is lightweight, and it has the required thermal properties. In this regard, low atomic number (low-Z) materials are widely considered in the design of radiation shielding materials[6]. An element with Z≤6 is regarded as a low-Z element; as such, materials composed of low-Z elements are considered low-Z materials. These low-Z materials are widely considered to provide an optimal balance between the four criteria required for radiation shielding materials. This section explores the use of polymeric nanocomposites for space radiation shielding, including their advantages and limitations.

2.4.1 Low-Atomic Number Materials

2.4.1.1 Hydrogen Compounds

Hydrogen is considered the most effective shielding element due to its low interaction with electromagnetic radiation [59]. The hydrogen atom has the highest atomic number (Z) to atomic weight (A) ratio value (Z/A = 1) with no neutrons in its nucleus. Consequently, hydrogen-rich materials have a high electron density and elicit no secondary neutron production when exposed to ionising radiation. However, various issues, including storage and maintenance, limit using pure hydrogen as a direct radiation shield. Instead, compounds with a high hydrogen content are studied in designing radiation shielding materials. Some examples include the metallic hydrides LiH, BeH_2, MgH_2, $LiBH_4$, and $NaBH_4$. LiH and $LiBH_4$, colourless inorganic compounds, have garnered favour as a potential replacement for conventional Al alloys[32, 33].

Researchers have investigated hydrogen storage materials to overcome the limitation of using pure hydrogen as a direct shielding material. However, the experimental results of these studies are too inconsistent and difficult to reproduce repeatedly[32]. Safety issues related to spontaneous combustion have damaged the feasibility of consideration for LiH in space applications[33]. Safety issues should also be considered when selecting the shielding material.

2.4.1.2 Hydrogen Rich Polymers

Typically, pure polymers are composed of low-Z elements, which make them suitable for space applications. These materials offer a significant weight reduction when compared to their metallic counterparts. Some commonly used polymers in space include epoxy resin, polyethylene (PE), polyetherimide (PEI), polysulfone (PSU), and polyimide[19, 35–37]. These uses vary from simple adhesives to accompanying layers on the radiation shielding materials.

PEI is a structural polymer with high strength, good flame, heat resistance, and hydrolysis resistance. PEI has a density of 1.128 g cm^{-3}, tensile strength of 113.8 MPa and degradation temperature of 200°C[78]. PSU, another structural polymer, has a relatively high glass transition temperature (T_g) above 190°C, facilitating a more comprehensive working temperature range of between -100 and 190°C[79]. However, compared to PE, PEI and PSU have shown a reduction in radiation shielding effectiveness over Al when shielding against GCR of around 11%[80]. Furthermore, the low hydrogen content in polyimide has resulted in it having very inferior radiation shielding effectiveness, even with its high degradation temperature (> 500°C) and tensile strength (231 MPa)[81]. These works show that hydrogen content plays a vital role in the radiation shielding effectiveness of polymer composites where it is favourable to have good mechanical and thermal properties.

Polyethylene (PE) has been extensively studied for its radiation shielding effectiveness[82, 83]. NASA has chosen PE as the reference material against which all other polymeric materials are compared, mainly due to its high hydrogen content[28]. Ultra-high molecular weight high-density polyethylene (UHMW-HDPE) and high-density polyethylene (HDPE) are currently the primary polymeric materials used in radiation shielding applications. They are commonly used as the industrial standard by which NASA, and other researchers, measure the effectiveness of developing materials[84–86]. In work by Cucinotta *et al.*[86], they show that the risk of exposure induced-fatalities for PE (1.7 - 3.5%) was lower than that of Al allows (2.0 - 4.4%), further advocating for replacing Al-based shields with polymeric materials with high hydrogen contents.

Poly(2, 5)benzimidazole (ABPBI) has yet to be tested for its radiation shielding effectiveness. However, due to its properties comparable to HDPE, it has been listed as a polymer of interest for further investigation [43]. Comparing ABPBI to HDPE, a complete comparison of the basic properties of the two polymer materials is given in Table 2.2. HDPE has stronger mechanical properties; however, the thermal properties

of ABPBI are significantly larger, providing the benefit of having a greater working temperature range. HDPE has a melting point of 80°C whereas ABPBI is thermally stable up to around 430°C[87].

TABLE 2.2: Comparison of the basic properties of HDPE and ABPBI[16, 17]

Property	HDPE	ABPBI
Z/A	0.57	0.52
Tensile Strength (MPa)	32	41
Thermal Conductivity (W.m^{-1}.K^{-1})	0.3	0.4

2.4.2 Nanocomposites

Nanocomposites are produced when a nanoscale filler, or simply nano-filler, material is introduced into the polymer matrix to improve the overall properties of the underlying polymer matrix. This section explores these nano-filler materials and their benefits concerning radiation shielding effectiveness.

2.4.2.1 Radiation Resistance

In radiation shielding, the radiation-induced free-radical formation is primarily responsible for degrading a material's properties. The ionising energy the polymer absorbs during irradiation initiates the free-radical production process[88]. Subsequently, the polymer undergoes chain breakage and cross-linking, which alter the polymer's intrinsic material characteristics. Hence, enhancing these inherent characteristics with a nano-filler can significantly reduce the probability of chain breakage and cross-linking occurring. The selection of the type of nano-filler used also plays a vital role in the properties of the fabricated nanocomposite, as many of its properties are inherited from the filler material[89]. A few aspects to consider when fabricating a nanocomposite include how uniformly the filler is dispersed in the polymer matrix, the type of interactions that will occur between the polymer matrix and the filler material, and the effective size of the filler[90]. To date, it has been shown that the reinforcement of the polymer with nano-fillers presents good radiation resistance for the composite materials [26, 39, 40, 63, 64].

Some studies have shown that nano-crystalline materials possess better radiation resistance than their polycrystalline counterpart[91]. This is attributed to the large volume-fraction of grain boundaries in the material that serves as an effective sink for defects produced during irradiation [92, 93].

Carbon based nano-filler materials quickly became the leading filler material to be investigated for radiation shielding applications[94]. UHMW-HDPE reinforced using graphite

nanofibres was studied by Zhong *et al.*[95]. Here, the addition of graphite nanofibres enhanced the thermal and mechanical properties of the UHMW-HDPE composite; however, it showed no improvement or reduction in its radiation shielding effectiveness. This was an unfavourable result; however, it led to exploring other carbon-based materials for the same application. In the years following this research, carbon nanotubes (CNTs) began to show signs of being the leading candidate. CNTs are unique nanostructures with remarkable physical and chemical properties, which researchers hope will be inherited by the polymer nanocomposite.

Several research groups have reported improvements in the polymer composite's thermal and mechanical properties with the addition of CNTs, examples of which can be found in [35, 96–98]. However, fewer groups have investigated the ionising radiation resistivity of CNT-based polymer composites [42, 99–101]. The material properties of poly(4-methyl-1-pentene) (PMP) reinforced with 0.5 wt. % loading of single-walled CNTs (SWCNT) was investigated by Clayton *et al.*[35]. This showed that the PMP/SWCNT nanocomposite had high radiation resistance and greatly improved mechanical performance that could warrant its replacement of PE as a shielding material. Computational simulation work of the LEO environment was conducted by Boul *et al.*[99] in which a proton beam with energies 10 to 30 MeV was used to detect the deformation in SWCNTs thin films. Their work showed that proton irradiation induced disorder within these films. Moreover, high-energy (63 and 105 MeV) proton beam experiments were conducted by Li *et al.*[26] on SWCNT-based polymer composites. Here, they reported that both the pure polymer, polydimethylsiloxane (PMDS), and the polymer composite, PMDS/SWCNT, showed a considerable weight reduction as compared to Al, up to 20.84%, for stopping protons of equivalent energy. Moreover, they reported that the polymer composite produced significantly fewer secondary radiation particles, which was attributed to the secondary radiation absorption ability of the SWCNTs in the polymer matrix. Their results also showed that relatively low loading (around 1.12 wt. %) of SWCNTs was enough to improve the proton shielding ability of the PMDS polymer matrix. Furthermore, the stopping range of ionising radiation in nanocomposites is affected by the composites' structure and distribution of the filler material. A non-uniform distribution of SWCNTs in a polymer matrix might affect the material reinforcement properties of the resultant nanocomposite. Li *et al.* thus suggested that the effects of uniformly distributed SWCNTs on stopping range and material properties be investigated in future applications of this nano-filler.

In work by Mathew *et al.*[102], they investigated the difference between SWCNTs and multi-walled CNTs (MWCNTs) after a 2 MeV proton irradiation. Their work indicated that MWCNTs showed significantly less disorder post-irradiation than their single-walled counterparts. Moreover, other studies have suggested that SWCNTs could suffer more

from interactions with charged particle irradiation[103, 104]. MWCNTs comprise several inter-layer covalent bonding, which can cause, post-ionising radiation, bridging between inter-layer graphene layers[105]. This bridging increases thermal conductivity as graphene bridges increase[106–108]. As such, MWCNTs are a promising nano-filler candidate for ionising radiation applications.

Secondary radiation (electrons, ions, and neutrons) produced by the interaction between ionising radiation and the shielding material can be just as, if not more, harmful as the primary radiation to payloads. During irradiation, the hydrogen-rich polymers will absorb secondary generated neutrons which could produce hazardous gamma rays[109]. The nano-filler should possess high stopping power for neutrons and a large bandgap to stop electrons and absorb these gamma rays. However, carbon-based materials have shown limited capabilities to shield high-energy electrons compared to other shielding materials such as lead (Pb)[63]. Pb's use in shielding materials has not been considered due to its toxicity. However, adding nano-fillers with similar shielding properties as Pb in the polymer matrix efficiently increases stopping power while maintaining the desired weight[110].

An example is Gadolinium oxide (Gd_2O_3), which has been shown to efficiently absorb electrons and gamma rays within a polymer matrix[110, 111]. These, unfortunately, are extremely expensive to produce, limiting more comprehensive applications [112, 113]. Ultimately, carbon-based materials, more specifically SWCNTs and MWCNTs, have shown the most promise in radiation shield applications as they provide a good balance between shielding functions and radiation resistance, and the cost of fabrication is low. These warrant their consideration as the nano-filler material of choice.

2.4.2.2 Mechanical Properties

With regards to mechanical properties, the intrinsic mechanical properties of CNTs make them a desired nano-filler. Their properties suggest they may be used as reinforcing fibres in high-toughness nanocomposites, where rigidity, strength and weight are essential considerations[114]. The strength of the nanocomposites depends on two variables: load transfer between the polymer matrix and the filler material and the nano-filler dispersion uniformity[6]. Regarding the first variable, if the interfacial adhesion between the phases of the polymer and the nano-filler is weak, CNTs behave like hole-inducing local stress concentrations and the mechanical benefits of CNTs are lost. For dispersion, if the CNTs are poorly dispersed, the CNTs will form localised bundles, creating areas with variable strengths in the nanocomposite.

Carbon-based filler materials enjoy wide use as mechanical reinforcement of polymers, which exhibit high strength-to-weight ratios[114–116]. The high-performance polymer polybenzimidazole (PBI) was studied for durable space applications using CNTs or other nano-filler materials[117]. These works reported that CNTs could improve the mechanical properties of polymers at relatively low CNT loading due to their high elastic-modulus and tensile strength[35]. CNTs also have excellent thermal and electrical conductivities and high oxidation resistance[90, 118]. Thus, CNTs can be used to fabricate mechanically strong, ultra-lightweight composites[119]. Additionally, studies have shown that polymeric materials reinforced with CNT exhibit improved mechanical and thermal stability and improved radiation resistance over their pure counterparts[117, 120, 121].

Apart from radiation shielding, these mechanically enhanced nanocomposites have numerous other possible applications in the space industry. Some include aerospace structural panels, ultra-lightweight space structures, and high stiffness-to-weight mirror substrates[6]. Many other applications in other industries would benefit from using these polymer nanocomposites.

2.4.2.3 Thermal Properties

As previously mentioned, the properties of a reinforced polymer composite depend greatly on the type of nano-filler material used. Since most polymers are known to have weak thermal properties, the focus was placed on using nano-filler materials with high thermal conductivity. The reported thermal conductivity of a single MWCNT (length of 2.5 μm and outer diameter of 14 nm) is >3000 W/mK [122], and SWCNTs can theoretically achieve values around 6000 W/mK[123]. In comparison, the thermal conductivity of Al is only 240 W/mK[124], which is less than a tenth of the value of MWCNT. As such, using CNTs, with high thermal properties, will improve radiation resistance and shielding capabilities but also the thermal stability of the nanocomposites.

Polymers, being plastics, generally have a thermal conductivity of less than 1 W/mK. Hence, by adding CNTs to the polymer matrix, the thermal conductivity of polymers can be increased by up to 33%[125]. In work by Haggenmueller *et al.*[126], they added 2 wt. % SWCNTs to the polymer matrix of low density polyethylene (LDPE) and HDPE, respectively. They reported an improvement in thermal conductivity of 592% in LDPE and 600% in HDPE. However, they found that the thermal conductivity improvement was non-linear with increasing SWCNT load. The thermal property reinforcement effects of CNTs are strongly affected by the aspect ratio, distribution in the matrix, and the interaction between the CNTs and the polymer matrix[6].

Even at low CNT loading in the polymer matrix, a loading threshold can be achieved in the nanocomposite. CNTs in the matrix come into contact to form a network-like structure in the nanocomposite. Zhong *et al.*[127] reported a reduction in the contact resistance between longer CNTs and significant overlap of CNTs in a polymer matrix. The reduction in the contact resistance subsequently improves the dispersion of CNTs, consequently enhancing the nanocomposite's bulk thermal properties. Achieving higher CNT loading concentrations in the nanocomposite without affecting the mechanical properties of the composite can result in better thermal properties. However, over-saturation of the polymer matrix with the filler material causes compositional instability and malformation of the underlying polymer matrix. Hence, finding the optimal CNT loading that balances improved thermal and mechanical properties is essential.

Chapter 3

Polymer Fabrication and Characterisation

3.1 ABPBI Fabrication Methods

This section outlines the three main membrane casting methods for poly(2, 5)benzimidazole (ABPBI). ABPBI, the most basic and inexpensive member of the PBI family of polymers, can be rapidly obtained at the laboratory level by the condensation of the simple AB-monomer, 3.4-diaminobenzoic acid (DABA) in poly phosphoric acid (PPA) with or without the use of P_2O_5[76, 77]. Furthermore, the synthetic path that follows the self-condensation of DABA in methanesulfonic acid (MSA) and P_2O_5 (Figure 3.1) is a popular path to follow [128].
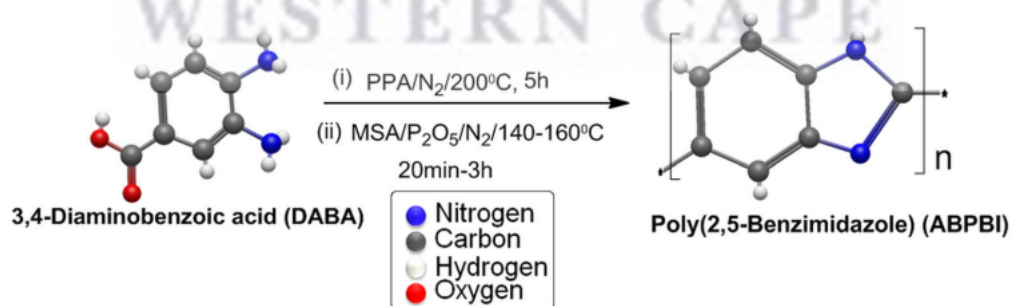
FIGURE 3.1: Synthesis of ABPBI from DABA [9]

Since polymerisation only requires the use of the AB-monomer, the purification of the monomer is not mandatory. As outlined in work by Asensio *et al.*[129], numerous groups have reported different viscosities for synthesised ABPBI polymers. However, they deemed that a viscosity between 2.3 and 2.4 dlg^{-1} is sufficient for formulating appropriate membranes. When using the dehydration agent P_2O_5 in the reaction mixture,

29

an optimum amount should be used to improve the dehydrating features of PPA. Saturation of the reaction media with P_2O_5 makes the polymerisation dope more solid-like, hindering stirring and consequently affecting the polymerisation kinetics as the reaction rate increases significantly. Due to its high molecular weight, ABPBI is dissolved in strong acids: MSA, PPA, H_2SO_4, formic acid (HCOOH) and trifluoroacetic acid (TFA). The casting of ABPBI membranes by different methods, solvents, and process parameters is discussed below.

3.1.1 ABPBI casting by Direct Acid Casting (DAC)

Asensio *et al.* first reported the direct acid casting method for ABPBI fabrication using a simultaneous doping and casting process[130]. Casting the membranes directly from a MSA-H_3PO_4 solution bypasses the polymer purification and separation methods. Additionally, the requirement for a nitrogen atmosphere is not compulsory during this process. Different compositions of ABPBI were dissolved in MSA and PPA, and the resultant solution was cast on a hot plate inside a fume hood to evaporate the solvent (MSA). Care was taken to optimise the PPA content of the reaction media to not eliminate all the PPA from the polymer matrix during the evaporation of the MSA. Membranes obtained from this method were homogeneous and transparent compared to conventional bath doping membranes. The XRD patterns for these DAC membranes observed an increase in crystallinity. However, they found that the conductivity of these membranes had decreased compared to the conventional acid bath-doped membranes.

3.1.2 ABPBI casting by Solution Casting (without phosphoric acid)

3.1.2.1 ABPBI casting from MSA

ABPBI membranes can effectively be cast from MSA [76, 77, 128, 131] in high temperature (HT) casting techniques. Care should be taken in the HT-casting technique to remove obnoxious fumes (MSA is a strong, non-volatile and hygroscopic acid). All heating of the ABPBI reaction media containing MSA should be performed in a well-ventilated fume hood. In the HT-casting technique, ABPBI polymer solution is poured onto a flat surface, generally a glass plate or petri dish, and heated to a temperature between 150-200°C to completely evaporate MSA from the polymer matrix [132–134]. When dissolving ABPBI in MSA, the solution becomes very viscous and sticky, making casting difficult by a suitable sol-gel transformation. The physical appearance of the membranes cast in MSA varies between the bottom (side closer to the hot-plate) and

the top of the membrane. The top face was dull, rough and non-uniform, while the bottom was glossy and uniform. Furthermore, casting membranes at high temperatures for prolonged periods increase the probability of pinholes and bubbles forming on the surface of the membranes. These pinholes could develop due to the hot plate not providing uniform heat distribution to the base of the glass plate or petri dish leading to uneven removal of MSA from the membranes. Consequently, to ensure uniform and homogeneous membranes are obtained from the HT-casting method, the temperature needs to be increased slowly, steadily and at regular intervals between 150 to 200°C[135]. In contrast to this, Linares *et al.*[136, 137] considered 100°C as the optimum temperature for completely evaporating MSA from the ABPBI polymer matrix.

Opting to cast ABPBI membrane from MSA at room temperature in atmospheric conditions results in significant moisture uptake by the solvent MSA, as opposed to its evaporation, and the membranes fail to form. From our experiments with membrane casting using this method, we found phase separation occurs with a gel-like structure forming at the mixing container's bottom while leaving the solvent to float at the top, consistent with reports from Linares *et al.*[136]. Furthermore, separating the membranes from the glass plate proved difficult, while immersion in a water bath to assist with this separation caused the membranes to break into unusable pieces.

3.1.2.2 ABPBI casting from other solvents

The casting of ABPBI membranes at room temperature is possible in solvents like formic acid (HCOOH) and strong basic alkalinised ethanol (ethanol-NaOH)[138, 139]. Membrane casting from an ethanol-NaOH solution at low temperatures is very sensitive to atmospheric conditions. Hence, special conditions are required for this casting procedure. These conditions include: casting on a glass plate inside a glove box in a nitrogen atmosphere, casting on a Teflon sheet at 0° in a nitrogen stream and keeping overnight and, again, placing the membranes in a vacuum at 40° for 24 hours on a glass substrate[140]. All these are very labour-intensive and time-consuming. Moreover, casting at moderate temperature conditions from NMP-LiCl or TFA-PA has also been demonstrated for ABPBI[141]. Viva *et al.*[140] dissolved the polymer in ethanol-KOH, an eco-friendly solvent, and used a spray casting technique to form homogeneous membranes, with a thickness of 80 μm, without defects. However, it took five days for the ABPBI to dissolve entirely in this solvent. In 2016, Nayak *et al.*[142] demonstrated the casting of ABPBI membranes from various solvents, namely; TFA, MSA, HCOOH and H_2SO_4, and meticulously correlated several characteristics of the matrix. However, some solvents produce membranes with inferior chemical stability, restricting their use on a broader scale.

3.1.3 ABPBI casting by Immersion Precipitation

To bypass the removal of solvents from the membranes and to simplify the membrane casting technique, Chaudhari *et al.*[143] proposed the idea of the immersion precipitation method for obtaining homogeneous ABPBI membranes. The ABPBI polymer solution, in MSA, was cast using a table-top casting apparatus on a heated glass plate. To detach the membrane from the glass plate it is submerged in a non-solvent bath containing PPA and deionised water at room temperature. The membranes obtained from this method showed a higher acid doping level and, subsequently, a higher proton conductivity than the aforementioned casting methods.

Several factors must be considered when attempting to derive an absolute ABPBI membrane matrix. Some of these include; selecting an appropriate solvent, knowing the definite composition of the polymer and solvent, optimising a proper dissolution time, and having better casting methods in which complete evaporation of the solvents is obtained over a suitable period. Nevertheless, most reports have selected MSA as a good solvent for casting the ABPBI membranes due to the membrane quality and ease with which it can be removed from the final membrane. As such, in this work, ABPBI membranes are cast using a combination of the casting from MSA and the immersion precipitation methods first reported by Kim *et al.*[128]. With this being a single-step polymerisation technique, we deemed this to be the most cost-effective way of producing high-quality ABPBI membranes for use in our studies.

3.2 Characterisation

Following selecting an appropriate ABPBI membrane fabrication method for our work, we now need to select appropriate characterisation techniques to evaluate the quality of the derived membranes. This work first focuses on the effects that the addition of MWCNTs has on the underlying polymer matrix of ABPBI. Once these have been established, the samples are exposed to proton irradiation. The pristine ABPBI and ABPBI/MWCNT nanocomposites will then need to be evaluated and compared for any structural and compositional changes due to the radiation exposure. The polymer's thermal stability must also be determined for both pre- and post-irradiation composites. As such, this section gives a brief overview of the selected characterisation that can effectively provide all the polymer property information required for this study.

3.2.1 Fourier Transform Infrared Spectroscopy

Fourier Transform Infrared Spectroscopy (FTIR) is an analytical technique for identifying organic, inorganic and polymeric materials[144]. FTIR uses infrared (IR) radiation to scan samples and observe chemical properties. When IR radiation passes through a sample, some are absorbed, and some are transmitted. The resulting signal is a spectrum representing the sample's molecular "fingerprint". This fingerprint is useful as different chemical molecules produce different spectral fingerprints for identification.
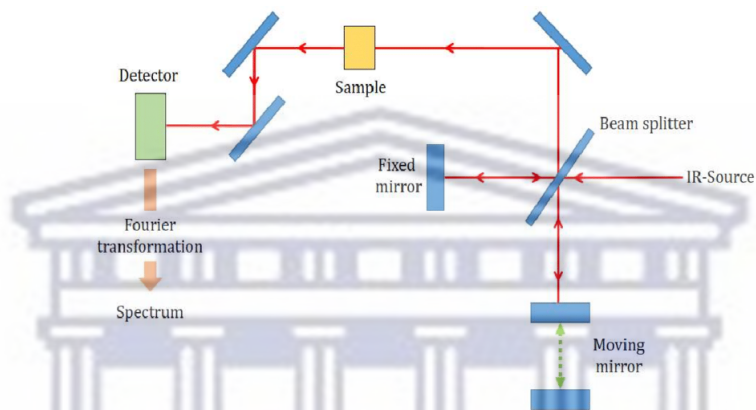
FIGURE 3.2: Schematic of FTIR spectrometer [10]

3.2.2 Differential Scanning Calorimetry

Differential Scanning Calorimetry (DSC) is a thermoanalytical technique used to measure the amount of heat transfer through a material. This heat transfer is benchmarked against a reference sample. A standard DSC technique result is a heat flux curve versus temperature. With DSC, you obtain information pertaining to fusion and crystallisation events, glass transition temperatures (T_g) as well as decomposition temperatures (T_d) of the polymers[145].
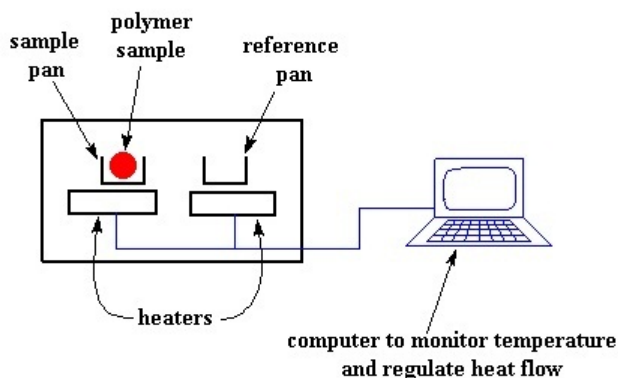
FIGURE 3.3: Scheme of DSC[11]

3.2.3 Thermogravimetric Analysis

Thermogravimetric Analysis (TGA) is an analytical technique used to determine a material's thermal stability by monitoring the weight change that occurs as a sample is heated at a constant rate. Performed in an oxidising or inert gas environment, TGA provides a weight sensitivity of up to 0.01 mg.
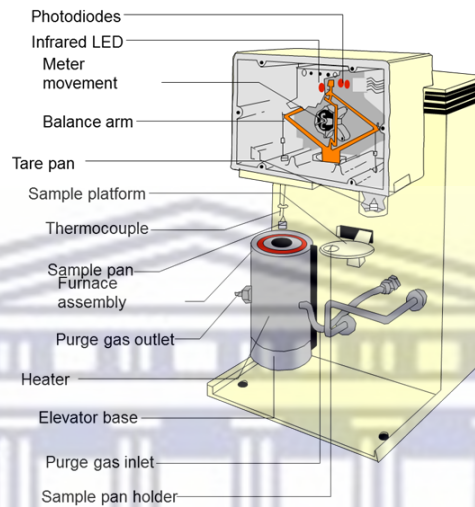
FIGURE 3.4: Scheme of Q50 TGA Instrument[12]

3.2.4 X-Ray Diffraction

X-Ray Diffraction (XRD) determines a material's crystallographic structure. It works by irradiating the material with incident X-rays and then measuring the intensities and scattering angles of the X-rays that leave the material[146]. The primary uses of the XRD technique include identifying materials based on their diffraction pattern, phase identification, and obtaining information on how the actual structure of a material deviates from its ideal counterpart owning to its internal stresses and defects[147].
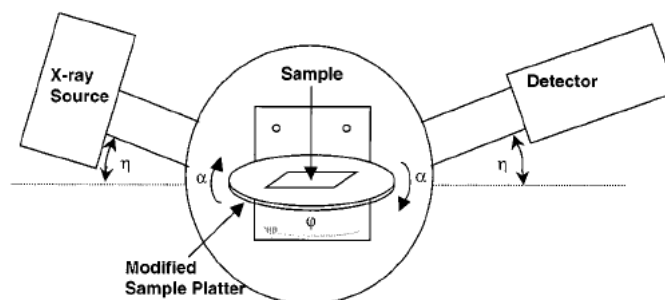
FIGURE 3.5: Scheme of Scintag XRD Diffractometer[13]

3.2.5 Scanning Electron Microscopy

A scanning electron microscope (SEM) projects and scans a focused stream of electrons over the surface of a sample to create an image[14]. The electrons interact with the sample, producing various signals to obtain information about the sample's surface topography and composition. With this, identical samples can be compared and inspected for any changes in surface morphology and elemental composition with Energy-dispersive X-ray spectroscopy (EDS).
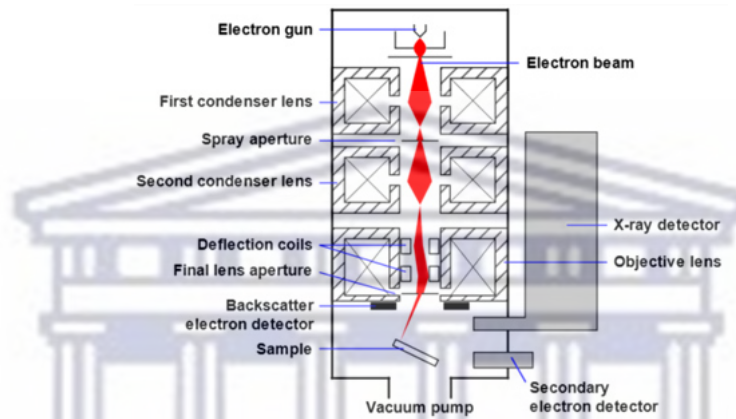
FIGURE 3.6: Schematic of a scanning electron microscope[14]

3.2.6 Tensile Strength Test

Tensile strength tests are performed with an Instron 5548 Micro Tester following ASTM D638-10 standards. Polymer samples are cut into dog bone shapes and loaded into the instrument for testing. The tensile strengths for each specimen are recorded until the sample's failure is reached, i.e. the centre of the dog bone brakes.

(A)
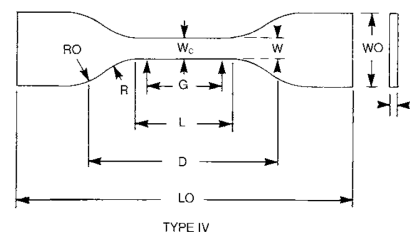
(B)

FIGURE 3.7: Instron 5548 Micro Tester (A) and Dog done shaped sample (B) [15].

This chapter looked at the various membrane casting techniques for fabricating ABPBI membranes. Among these, we selected the membrane fabrication method that best suited our membrane quality requirements. We then gave a brief overview of the selected characterisation techniques used to analyse our fabricated membranes and can now test the efficacy of ABPBI and ABPBI/MWCNT nanocomposites as a proton radiation shield.

Chapter 4

Modelling of a PECVD system for the growth of MWCNTs

In this chapter, we computationally explore the feasibility of growing the required nano-filler material, MWCNTs, using one of the deposition methods available at the author's home institution (University of the Western Cape, South Africa). The deposition method selected for this exploration is the plasma-enhanced chemical vapour deposition (PECVD) technique. For this, the COMSOL multiphysics software is employed to model the condition within a PECVD reactor to determine the optimum parameters required for the growth of MWCNTs. The following sections provide information on the modelling procedures and outcomes.

37

4.1 Abstract

A 2-D axisymmetric fluid model simulation of inductively coupled discharges of a methane plasma is presented. The continuity equations for charged species and electron energy are solved with COMSOL multiphysics. A constant frequency and gas pressure, 13.56 MHz and 0.02 Torr, respectively, are used. Initially, a coil power of 100 W is used, but this is later adjusted to include various coil powers up to 600 W. A Boltzmann equation solver is used to calculate the electron energy distribution function and reduced electron mobility. The effects of increased coil power are investigated, and the results indicate that power increases increase the electron temperature and charge densities moderately. The growth rate of carbon across the substrate holder is mapped to determine a growth profile for the system.

4.2 Introduction

Efficient wafer processes require high-density plasmas. Inductively coupled plasma (ICP) reactors are widely used for microelectronic device fabrication for their high plasma densities and good deposition uniformity[148]. In ICP reactors, it is possible to provide high ionic and radical fluxes onto the wafer surface while the ion energy is controlled independently of the plasma density. In addition, high ion selectivities are a requirement for competitive semiconductor manufacturing[149]. A way to achieve this is by controlling the bombardment of the surface by the ions. However, independent control of the plasma density and ion energy cannot be achieved with capacitively coupled plasma (CCP) reactors, while ICP reactors offer such control of those properties. This is done by capacitively coupling the radio frequency (RF) bias power to the ICP chamber[150]. Using numerical simulations for ICP reactors provides an improved understanding of the ICP process while also providing measurable quantities that otherwise would be challenging to attain experimentally. Numerical simulations provide a quick way to understand the plasma behaviour in the reactor and subsequently allow for the optimisation of the plasma deposition process.

Various methods can be used to explore the nature of plasma physics. Due to the complex problems encountered in plasma physics, computer simulations of numerical schemes have become the more desired approach. Numerical methods in computer simulations offer an efficient design tool to provide accurate performance predictions in plasma physics applications[151]. Computer plasma simulations can be subdivided into two general categories: the fluid and the kinetic models. An overview of the fluid, kinetic and hybrid plasma models can be found in the work by van Dijk *et al.*[152].

Kinetic models generally offer higher accuracy than fluid models in these simulations but suffer high computational costs. Fluid models are usually faster and provide valid approaches to the plasma processes within certain limits [153, 154]. Some examples of these codes would be the hybrid plasma equipment model of Kushner *et al.*[155] or the Plasimo model[152]. An increase in demand has seen commercial multiphysics codes become more prominent. In the last decade, commercial multiphysics codes have become more widely used in the simulations of various types of non-equilibrium plasmas. Simulations based on fluid models have been shown to provide valid approaches to the plasma process for low Knudsen numbers (Kn < 0.2), which is the case for typical ICP chambers of pressure 10 mTorr or higher[153–155]. In this work, the ICP chamber of the Cluster Apparatus for Device Applications Research (CADAR) system at the University of the Western Cape (UWC) is investigated using the COMSOL multiphysics software. An image of the reactor is provided in Figure 4.1, which has a unique design among systems of this kind. COMSOL is a software package that provides a plasma module with an ICP interface. As there is limited literature available concerning applications of plasma module of COMSOL for methane[148], this work aims to provide simulation results that can be used to qualitatively benchmark against published work, which allows for further optimisation of the system. The approach used in this work is a fluid model. Jia *et al.*[156] provide an example of ICP reactor simulation using COMSOL. The work presented incorporated many simplifications to keep computational costs low, with one such simplification being the use of a Maxwellian electron energy distribution function.
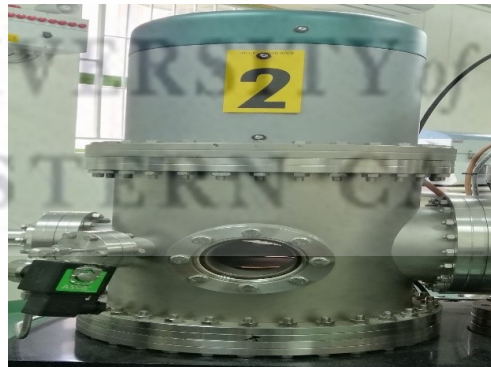
FIGURE 4.1: PECVD reactor chamber of the CADAR system fitted with a COPRA DN 250-CF round plasma beam source.

This work aims to develop a model that will provide an improved understanding of the dynamics of a high-purity methane discharge in the CADAR system. To this end, we employ a two-dimensional (2-D) axisymmetric self-consistent fluid model of the system depicted in Figure 4.1. In our work, improvements are implemented in this existing model, including the Boltzmann equation solver and a two-term approximation function that calculates the electron and ion mobility corresponding to a reduced electric field.

4.3 Description of the Computational Model

Three classes of modelling techniques can be used to simulate plasma discharges. These are: statistical, or particle, models[157, 158], fluid models[159, 160] and hybrid models[160, 161]. All three models have specific advantages and drawbacks, depending on certain conditions. In this work, a fluid model is employed to describe the particle transport in radio frequency discharges, as fluid models are usually faster and give valid approaches to plasma processes within certain limits[153, 154]. The ICP interface of the plasma module of COMSOL was used to run simulations in this work. A 2-D axisymmetric model of the CADAR deposition system was considered adequate to provide all the data required for this study. A schematic diagram of the system is given in Figure 4.2. The system consists of a single multi-turn, homogeneous coil placed behind a dielectric material made of quartz with a thickness of 5 mm, as outlined by the system's user manual[162]. This quartz liner was considered to have a relative permittivity of 4.2. The area surrounding the coil, between the quartz liner and the system wall, is considered to possess vacuum properties as it forms part of the internal structure of the reactor. The system's walls are electronically grounded, i.e. potential on the walls is 0 V. The outer boundaries of the geometry were magnetically insulated, i.e. $\mathbf{n} \ \mathbf{A} = 0$, where $\mathbf{n}$ is the surface normal and $\mathbf{A}$ the magnetic vector potential.
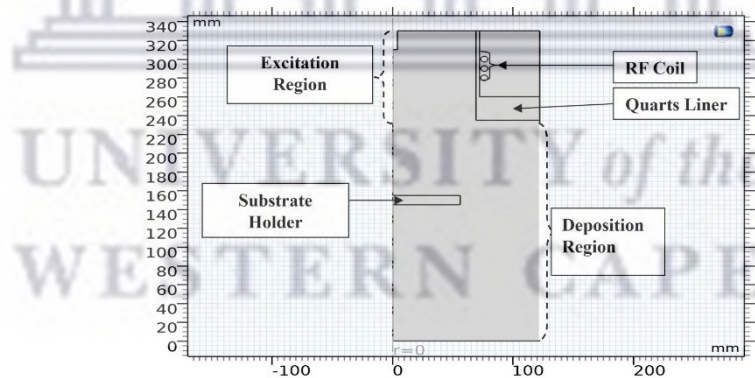
FIGURE 4.2: Schematic Diagram of the CADAR system used in the simulations.

The simplified methane chemistry considered in this model is shown in Table 4.1. The dominant reaction pathways are the ionisation reactions. Electron impact reactions with CH_4 cultivate the formation of radicals and ions. When a sinusoidal voltage is applied and the discharge is ignited, electron impact and dissociation of CH_4 occur, resulting in the consumption of CH_4 and the creation of new species (electrons, ions and radicals). The formation of electrons and ions in the plasma is crucial in sustaining the discharge. Hence, the ionisation reactions become the most critical channels for electron impact ionisation of CH_4. The cross-sectional data in this simulation for electron methane collisions are generated with the Boltzmann code BOLSIG[163].

TABLE 4.1: Important collision processes in a methane discharge[18].

Process	Reaction	$\Delta\varepsilon$ [eV]
Dissociation Attachment	$e + CH_4 \rightarrow CH_3 + H^-$	0
Dissociation Attachment	$e + CH_4 \rightarrow H_2 + CH_2^-$	0
Elastic	$e + CH_4 \rightarrow e + CH_4$	0
Vibrational Excitation	$e + CH_4 \rightarrow e + CH_4$ (V23)	0.162
Vibrational Excitation	$e + CH_4 \rightarrow e + CH_4$ (V13)	0.361
Dissociation Excitation	$e + CH_4 \rightarrow e + CH_2 + H_2$	9.0
Dissociation Excitation	$e + CH_4 \rightarrow e + CH_3 + H$	10.0
Ionisation	$e + CH_4 \rightarrow 2e + CH_4^+$	12.6
Ionisation	$e + CH_4 \rightarrow 2e + CH_3^+ + H$	14.6

This model did not consider convective flux to study the methane plasma discharge without the effects of flow vortices, and therefore, no gas inflow or outflow was used. A similar approach was used by Brezemes *et al.*[164] and this was found to be a valid approach. The model has 15922 domain mesh elements and 882 boundary mesh elements, most of which are triangular. Boundary layers were created next to the walls. This is needed to capture the space charge separation between the electrons and ions close to the walls. A fine mesh was also created in the coil domain since the plasma skin depth also needs to be resolved. The final mesh is shown in Figure 4.3.

For the simulations to run, COMSOL requires defining surface reactions that describe how charged particles interact with the system's walls. In this work, we consider two charged species, CH_4^+ and CH_3^+, and their wall interactions are shown in Table 4.2, along with their rate coefficients obtained from the literature[165].

TABLE 4.2: List of Surface Reactions with Rate Coefficients.

Reaction	Rate Coefficient $[cm^3 s^{-1}]$[165]	Sticking Coefficient
$CH_4^+ \rightarrow C_s + 2H_s + H_2$	1.2384×10^{17}	1
$CH_3^+ \rightarrow C_s + H_s + H$	1.1991×10^{17}	1

In Table 4.2, C_s and H_s represent surface species created from ion interactions with walls. Ions are essential in forming the deposited material layers in the PECVD process. Ions have a hand in creating the interrelated structure, which alters the morphology and properties of the deposited material and the kinetics of the heterogeneous chemical reactions[165]. The growth rate for the deposited films can now be extracted by including the surface reactions in the model.

The simulation ran for a fixed pressure of 0.02 Torr, the standard deposition pressure, a frequency of 13.56 MHz and a power of 100 W. As a secondary aim for this study, we attempted to determine the conservation of CH4 and the yields of the reaction products within the system. As such, calculations are carried out for up to 10 seconds. We also

attempt to determine a deposition rate for carbon materials within the PECVD reactor system.
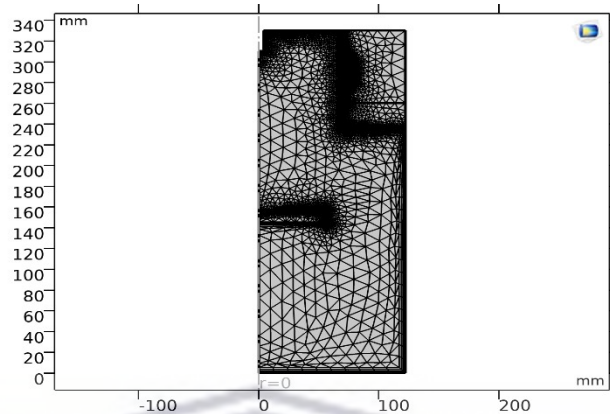
FIGURE 4.3: Final Mesh of the CADAR system used in the simulations.

The fluid model is used to track all species as a function of time with a maximum time-step to the order of 1 nanosecond until a steady state (convergence) is reached for the charged species. Convergence is achieved when the difference between consecutive time steps in the main variables is less than 0.05%. Figure 4.4 shows the evolution of the error with time steps, referred to as the residuals. The total computation time for the main simulation was around 11 minutes.
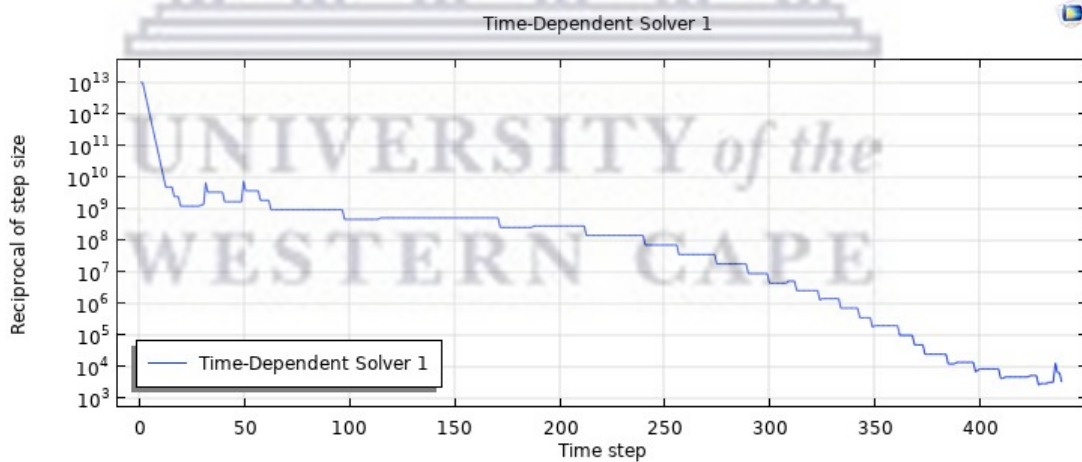
FIGURE 4.4: Evolution of the linear error with time step for calculating discharge power of 100 W, 13.56 MHz and pressure of 0.02 Torr for a total runtime of 11 minutes.

A few assumptions made in our model are summarised in the following points [166, 167] and incorporate these assumptions, and it has shown to work well for their purposes:

1. The methane neutral atoms are assumed to be the dominant species in the discharge. These are uniformly distributed in the system, and the system pressure and gas temperature determine their density.

2. Due to the significant difference in mass between ions and electrons, ions can only gain small amounts of energy from the applied fields and lose a considerable amount of energy through electron collisions. As such, ion temperature is assumed to be the same as the neutral gas temperature.

3. In our model, electrons at the walls are reflected with a probability of 20% ($r_e = 0.2$) as a baseline parameter.

Along with these assumptions, the following initial plasma conditions were implemented in our model:

1. Initial electron density, $n_{e,0}$, represents the initial seed electrons in the plasma: $n_{e,0} = 1 \times 10^{14} \text{m}^{-3}$.

2. Initial mean electron energy $\bar{\varepsilon}_0 = 4$ V. This value corresponds to an electron temperature (T_e) value of 2.66 eV.

3. Electric potential, $V = 0$ V.

4.4 Theory

The Fluid plasma model describes the time-averaged statistical properties of the plasma particles. Each specie is considered a separate fluid to satisfy mass conservation in all computational regions. A brief description of the groups of equations used in the simulations is given in this section. The first such set is the Drift-diffusion equations. The Drift-diffusion equations describe the transport of electrons and electron energy[148]:

$$\frac{\partial n_e}{\partial t} + \boldsymbol{\nabla} \cdot \Gamma_e = R_e - u \cdot \nabla n_e \tag{4.1}$$

where n_e is the electron density, Γ_e is the flux of the electrons due to the electric field and diffusion, R_e is the electron generation rate due to collisions and reactions and $-u \cdot \nabla n_e$ is the convective term which is not considered in this work as there is no gas flow present. Equation 4.1 can be rewritten as:

$$\frac{\partial n_\varepsilon}{\partial t} + \boldsymbol{\nabla} \cdot \Gamma_\varepsilon + E \cdot \Gamma_e = R_\varepsilon + \frac{Q}{q} \tag{4.2}$$

where n_ε is the electron energy, Γ_ε is the flux of electron energy, $E \cdot \Gamma_e$ represents the Joule heating or heating due to resistance, R_ε is the gain or loss of energy, and

Q/q is the term that accounts for other possible power inputs to the system. The term q is the charge of an electron, while Q is the external power input. This model was calculated in conjunction with the Magnetic Field Interface of COMSOL. The flux terms Γ_ε and Γ_e, which arise from the electric field and diffusion, depend on transport coefficients: electron energy, electron diffusivity, electron energy mobility and electron energy diffusivity. COMSOL allows the use of the reduced forms of these variables, which are the variables mentioned above divided by the density of the neutral particles.

For this work, the reduced electron mobility was calculated as a function of the mean electron energy. This was done using the Boltzmann solver interface. The interface solves the Boltzmann equation with a two-term approximation, as outlined by Hagelaar *et al.*[168]. The solver calculated the electron energy distribution function (EEDF) and the reduced electron mobility corresponding to the mean electron energy. The calculated values for the reduced electron mobility were included in the initial values for the main simulation. Drift diffusion equations are also used in COMSOL to calculate the movement of heavy species in the plasma. Heavy species are regarded as all species in the plasma except for electrons. More information on how these equations are implemented in COMSOL can be found in the COMSOL user manual[169].

Maxwell's equations describe and calculate the magnetic field inside the system and surroundings. Expressing Ampere's law as a function of magnetic potential, the following equation is obtained:

$$(j\omega\sigma - \omega^2\varepsilon_0\varepsilon_r)A + \nabla \times (\mu_0^{-1}\mu_r^{-1}\nabla \times A) = J_e \qquad (4.3)$$

where j is the imaginary unit, ω is the angular frequency of the electric source, σ is the electrical conductivity, ε_0 and ε_r are the vacuum and relative permittivity, respectively, A is the magnetic vector potential, μ_0 and μ_r are the vacuum and relative permeability respectively, and J_e is the applied external current. An external current (J_e) is applied to the coil. This current is sinusoidal and creates a time-varying magnetic field in the chamber. In Equation 4.3, the magnetic vector potential is calculated rather than the magnetic field. From Faraday's law, this time-varying magnetic field creates an electric field in the system, accelerating the electrons and creating an induced current. This work calculates the induced electric field by the Magnetic Field interface of COMSOL. Also, the induced electric field is calculated in the azimuthal direction only. This acceleration is a consequence of the positioning of the coils, which restricts the motion of the electrons in the azimuthal direction. It is set to zero in the other directions, radial and vertical. This results in the induced current being azimuthal as well. This is a 2-d axisymmetric analysis of the system, so the inductive power will be considered a scalar,

as the power that accelerates the electrons in the vertical direction creates a stream of charged particles. The input power is calculated in the following way:

$$Power = \frac{1}{2}real(E \cdot J) \tag{4.4}$$

where E is the induced electric field, J is the total electric current, and *real* refers to the real part of the scalar operation. The induced current is calculated along with the induced electric field as:

$$J_i = \sigma E \tag{4.5}$$

where J_i is the induced electric current. The total current, J, is calculated using the model's displacement and induced current. In this case, the displacement current is very small compared to the induced current, therefore:

$$J \approx J_i. \tag{4.6}$$

Thus, the power can be calculated as a function of the induced electric field with the magnetic potential. The interface also uses Poisson's equations to calculate the electric potential, V. This is only solved in the r and z-direction:

$$\nabla^2 V = -\frac{\rho_f}{\epsilon} \tag{4.7}$$

where ϵ is the total electric permittivity, and ρ_f is the space charge density. ρ_f is calculated in every mesh cell's negative and positive charge concentration.

4.4.1 Boundary Conditions

Electrons in the system are lost due to random collisions within a few mean free paths of the wall and gained due to secondary emission effects. This results in the following boundary condition for the electron flux[170]:

$$-\mathbf{n} \cdot \Gamma_e = \frac{1 - r_e}{1 + r_e}\left(\frac{1}{2}v_{th}n_e\right) - \Sigma_p\gamma_p(\Gamma_p \cdot \mathbf{n}) \tag{4.8}$$

$$v_{th} = \sqrt{\frac{8k_BT_e}{\pi m_e}} \tag{4.9}$$

where $\mathbf{n}$ is the unit vector normal to the wall, v_{th} is the electron thermal velocity, k_B is the Boltzmann constant and m_e is the electron mass. The second term in Equation 4.8 is the gain of electrons due to secondary emissions. The electron energy flux towards the walls is given by:

$$-\mathbf{n} \cdot \Gamma_e = \frac{1 - r_e}{1 + r_e} \left(\frac{5}{6} v_{th} n_e \right) - \Sigma_p \gamma_p \epsilon_p (\Gamma_p \cdot \mathbf{n}) \tag{4.10}$$

where ϵ_p is the mean energy of the secondary electrons and the second term in Equation 4.10 is the secondary emission energy flux. For the last boundary condition, the electric potential must satisfy the following:

$$V = 0 \ and \ V = V_{rf} \tag{4.11}$$

where $V = 0$ accounts for the grounded walls, and $V = V_{rf}$ is applied to the driven electrodes.

4.5   Results and Discussion

Typical results of the fluid model for glow discharge plasmas are the densities of the various species, the electric field, the electron temperature, the magnetic field, and the power and resistance of the coil itself. The convergence criteria of the simulation are attained after a few minutes (9 - 11) on an Intel Core (TM) i7-7820X CPU, 16x3.60 GHz with 24 GB RAM. The simulations are carried out for a fixed pressure of 0.02 Torr with a gas temperature of 300 K. In this work, before the main simulation was calculated, the Boltzmann equation with a two-term approximation was used to calculate the EEDF, which is required to determine the reduced electron transport properties used in the main model. The results hereof can be seen in Figure 4.5 and 4.6.

Figure 4.5 presents the EEDF for a pressure of 0.02 Torr and plasma discharge power of 100 W. It can be seen from Figure 4.5 that the electron collision profile with methane closely resembles that of a Maxwellian distribution, which further validates the selection of Boltzmann equations for the EEDF calculations in our model. Furthermore, the use of Boltzmann equations to calculate the EEDF is generally more accurate as an anisotropic perturbation is introduced, and the EEDF is computed based on a coherent set of electron impact reaction cross sections that describe how electrons lose or gain energy in collisions with the background gas[171]. Consequently, if a Maxwellian distribution were used in the EEDF calculation, this would lead to model results that are very similar

to those obtained using the Boltzmann equations but at reduced accuracy. Essentially, the EEDF calculation method does affect the modelling results but not by orders of magnitude; in Figure 4.6, the reduced transport properties are calculated due to the EEDF calculations.
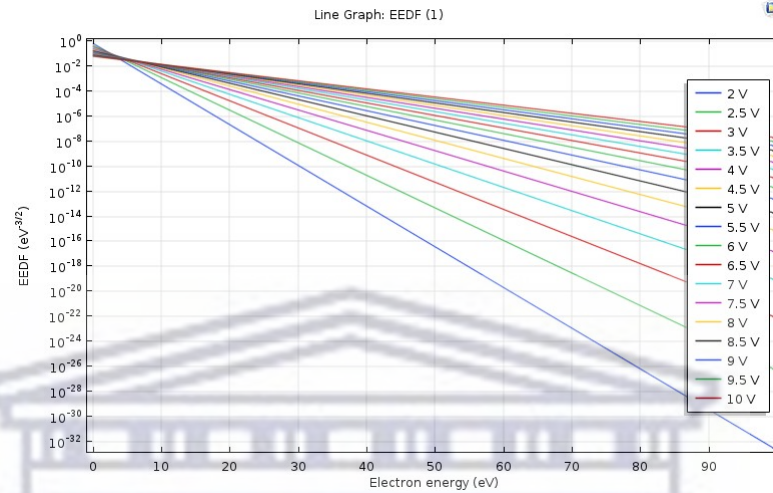
FIGURE 4.5: EEDF vs Electron energy plots of Methane for mean electron energies from 2-10 V.
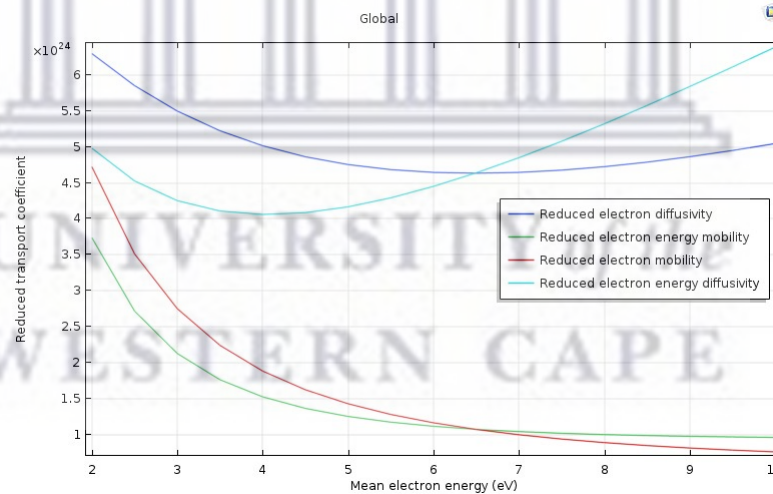
FIGURE 4.6: EEDF vs Electron energy plots of Methane for mean electron energies from 2-10 V.

Ideally, in the plots for the reduced transport properties, one would like to identify the minimum mean electron energy and the corresponding reduced transport coefficient that would lead to a stable and convergent solution. Our model requires the input of the reduced electron mobility as an initial value. Using the data in Figure 6, we were able to determine that the initial value for the reduced electron mobility, n, would have to be in the range between 4 and $4.5 \times 10^{24} \mathrm{V}^{-1} \mathrm{m}^{-1} \mathrm{s}^{-1}$ with a corresponding initial mean electron energy, $\bar{\varepsilon}_0 = 4$ V. With all the required initial values calculated, the main model was now ready to be calculated, and the results are presented in the sections below.

4.5.1 Electron Density

As previously mentioned, ICPs generally operate at high charge densities. Consequently, a relatively high electron density is required to sustain the plasma glow discharge in a reactor of this kind. Figure 4.7 shows the electron density distribution within the CADAR system at a convergence time of 0.01 s.
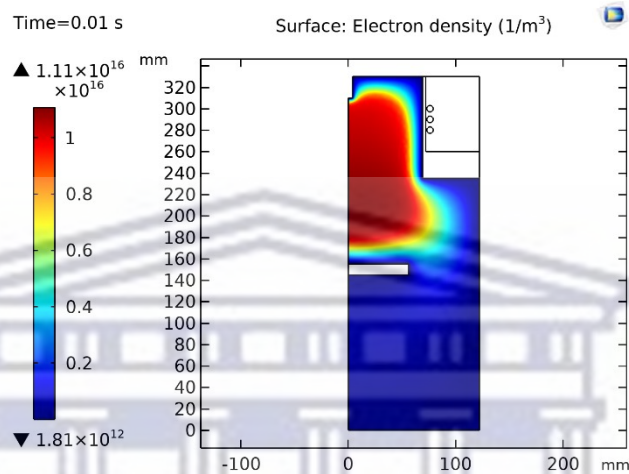
FIGURE 4.7: Electron density in the system for the pressure of 0.02 Torr, discharge power of 100 W and frequency of 13.56 MHz.

From Figure 4.7, we see that the electron density is highest in the excitation region, the area adjacent to the coils, and the extraction region, the area above the substrate holder. The electron density in these regions reaches a maximum value of 1.11×10^{16} electrons/m^3. This is generally referred to as the plasma bulk, i.e. the most intense region. As a result of electron flux from the plasma bulk and the walls, the electron density decreases drastically in the axial direction.

Due to the placement of the coils, which confines the electrons in the azimuthal direction, electrons migrate in the axial direction down towards the substrate holder, creating various plasma intensities above and below the holder itself. To account for this, the system is fitted with an adjustable substrate holder, which can move the substrates closer to or further away from the plasma bulk, depending on the deposition requirements. At its furthest point from the excitation region, indicated by the vertical axis at 0 mm in Fig 4.7, the electron density has a value of 1.81×10^{12} electrons/m^3.

4.5.2 Electron Temperature
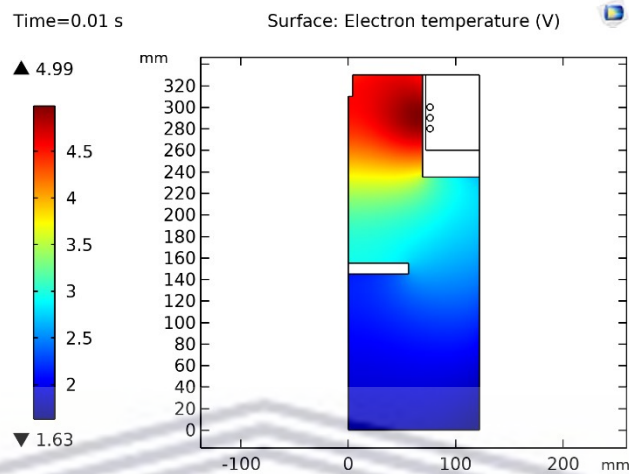
FIGURE 4.8: Electron density in the system for the pressure of 0.02 Torr, discharge power of 100 W and frequency of 13.56 MHz.

The electron temperature (T_e), which is a measure of the change in internal energy concerning entropy[172], is highest in the excitation region with a maximum value of 4.99 V. This is expected due to the region's proximity to the coil, given that this is where the bulk of the power deposition occurs. T_e remains relatively uniform in this region and decreases as you move down in the axial direction. From this, it can be seen that the electric field in the plasma bulk is slightly stronger than in any other region of the system.

4.5.3 Electrical Properties

From an electrical standpoint, the quantities of interest are; the total power dissipation, coil resistance and inductance. These parameters give a good indication of a system's efficiency and provide measurable quantities that can easily be compared to literature if needed. The first parameter we consider is coil resistance; the results are shown in Figure 4.9. Figure 4.9 shows that the coil's resistance increases slightly by a factor of 10 when the plasma discharge is ignited. When ignited, the plasma induces a substantial opposing current back into the coil, causing the observed increase in the coil resistance. Once stabilisation is achieved, the coil resistance starts to decrease as the induction mentioned above decreases. As a corrector, the electric potential across the coil needs to be increased to maintain a constant total current, as outlined by work done in[170]. The next parameter of interest is the coil power; the results are presented in Figure 4.10.
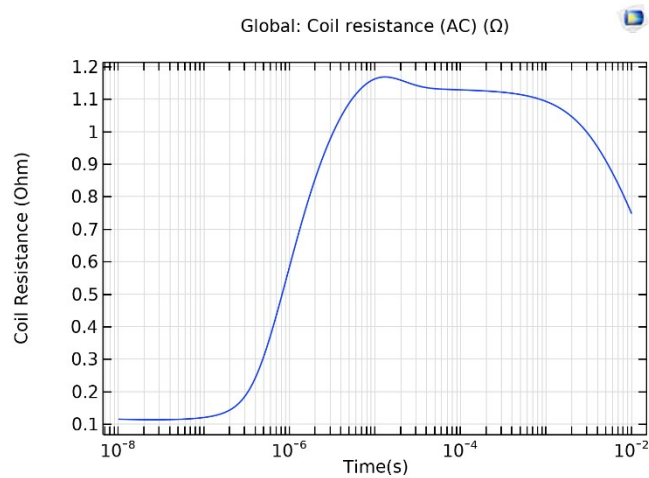
FIGURE 4.9: Coil resistance vs time in the CADAR system.
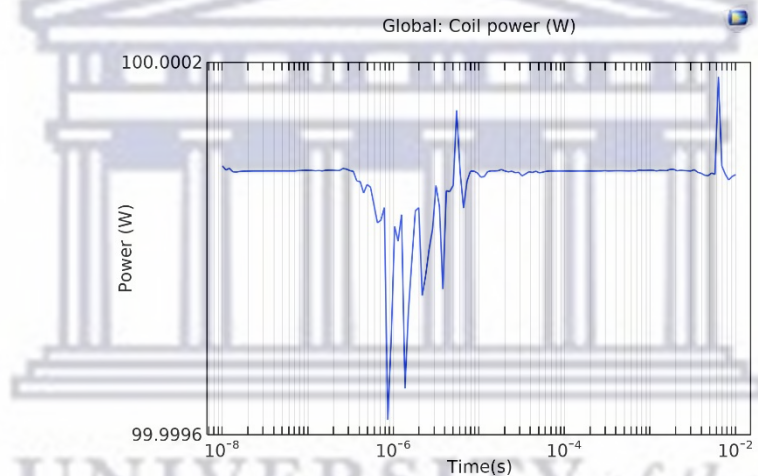
FIGURE 4.10: Coil power vs time in the CADAR system for coil power of 100 W.

Initially, all power dissipated in the system is dissipated by the coil. Once the plasma glow discharge is ignited, electrons absorb more power as electron collisions dissociate neutral gas atoms into electrons and ions[170]. This is evident in the distinct drops in the total coil power seen in the plots in Figure 4.10. This power absorbance lasts approximately 2 microseconds before the coil power stabilises and returns to a constant of 100 W. In this work, the dominant ions formed from electron collisions with Methane are CH_4^+ and CH_3^+. The ion number density for the ions mentioned above is calculated separately to track their abundance in the system, as both play an important role in the PECVD process of Carbon materials. The results of this analysis are presented in Figure 4.11 and 4.12.
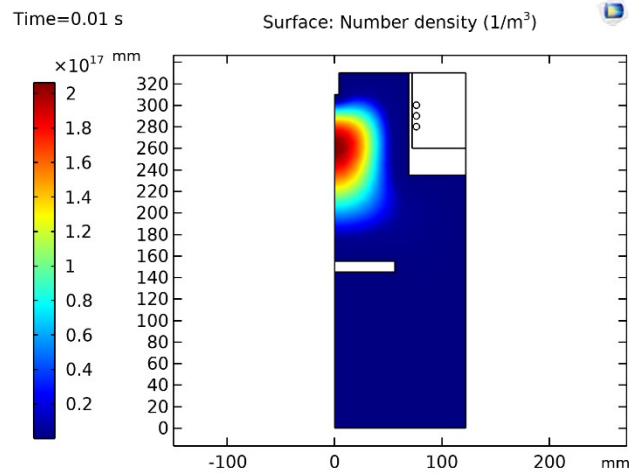
FIGURE 4.11: CH_3^+ ion number density for the system with a pressure of 0.02 Torr, discharge power of 100 W and frequency of 13.56 MHz.
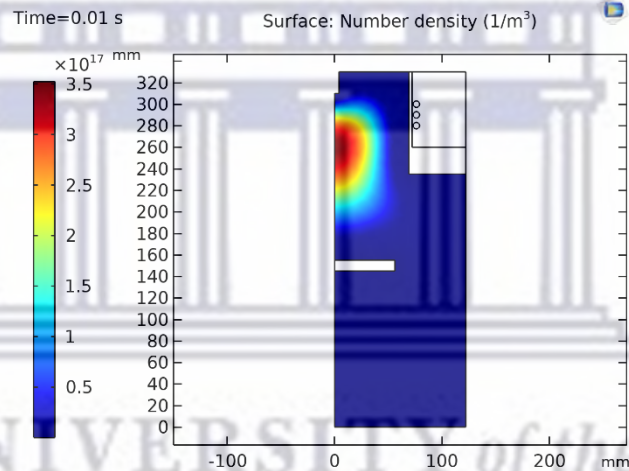
FIGURE 4.12: CH_4^+ ion number density for a system with a pressure of 0.02 Torr, discharge power of 100 W and frequency of 13.56 MHz.

Both CH_4^+ and CH_3^+ have their highest number density in similar regions. This peak again occurs in the excitation and extraction regions of the system. This correlates to the electron density peak seen earlier in Figure 4.7. It stands to reason that if the electron density is high, the likelihood of electron collisions with neutral methane molecules would also be high, consequently increasing the ion production rate in this region.

It can also be seen that both ions reach a maximum density in the order of 10^{17} m^{-3}, 2.2×10^{17} m^{-3} for CH_3^+ and 3.5×10^{17} m^{-3} for CH_4^+, respectively. This is consistent with the expected total charge density, $> 10^{17}$ m^{-3}, for an Inductively Coupled Plasma system[152]. The last parameter of interest pertaining to the electrical properties is the power dissipation into the plasma. The plasma skin depth determines the region over which power is deposited to the plasma. This region is shown in Figure 4.13. The plasma skin depth is defined as[170, 173]:

$$\delta = \sqrt{\frac{2}{\omega\sigma}} \tag{4.12}$$

where ω is the angular frequency and σ is the plasma conductivity. From Equation 4.12, increasing the driving frequency does not necessarily couple more power into the plasma. As the frequency increases, the plasma shields the region over which the power is deposited into a thin layer close to the wall adjacent to the coil. The plasma skin depth in our model is of the order of 40 mm, which, according to Stenson *et al.*[173], prevents the electric field from penetrating the core of the plasma.
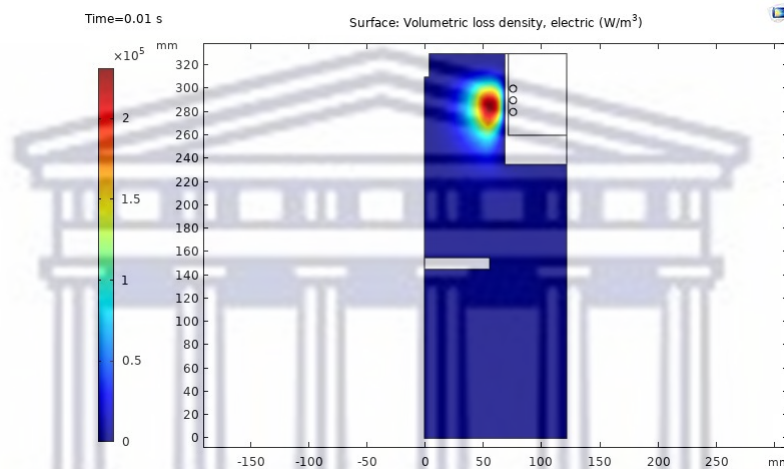
FIGURE 4.13: Plot of the power deposition into the plasma for a system with a pressure of 0.02 Torr, discharge power of 100 W and frequency of 13.56 MHz.

For the current set of parameters, our model shows that the ICP system creates a consistent methane plasma within the confines of its geometry. To further explore the plasma dynamics within the system, a second study was conducted in which the coil power was sequentially increased to a maximum value of 600 W. The comparative results of this study are presented in the sections that follow.

4.5.4 The Effects of Varying Coil Power on the Plasma Conditions

This section presents electron density, electron temperature and ion density as a function of coil power. In this study, all the initial values are kept the same as in the previous study, but the coil power is increased. For each new run, the coil power varied by 100 W, from 100 to 600 W. This culminates in having six sets of results for each parameter of interest. We start by comparing the electron density, as shown in Figure 4.14. From the results presented in this figure, we immediately notice that an increase in the coil power increases the migratory effects of the electrons. This is most likely due to the increase in the induced electric field strength due to the increased coil power. Again, due to the

placement of the coil, electrons are accelerated axially away from the excitation region towards the lower part of the chamber.
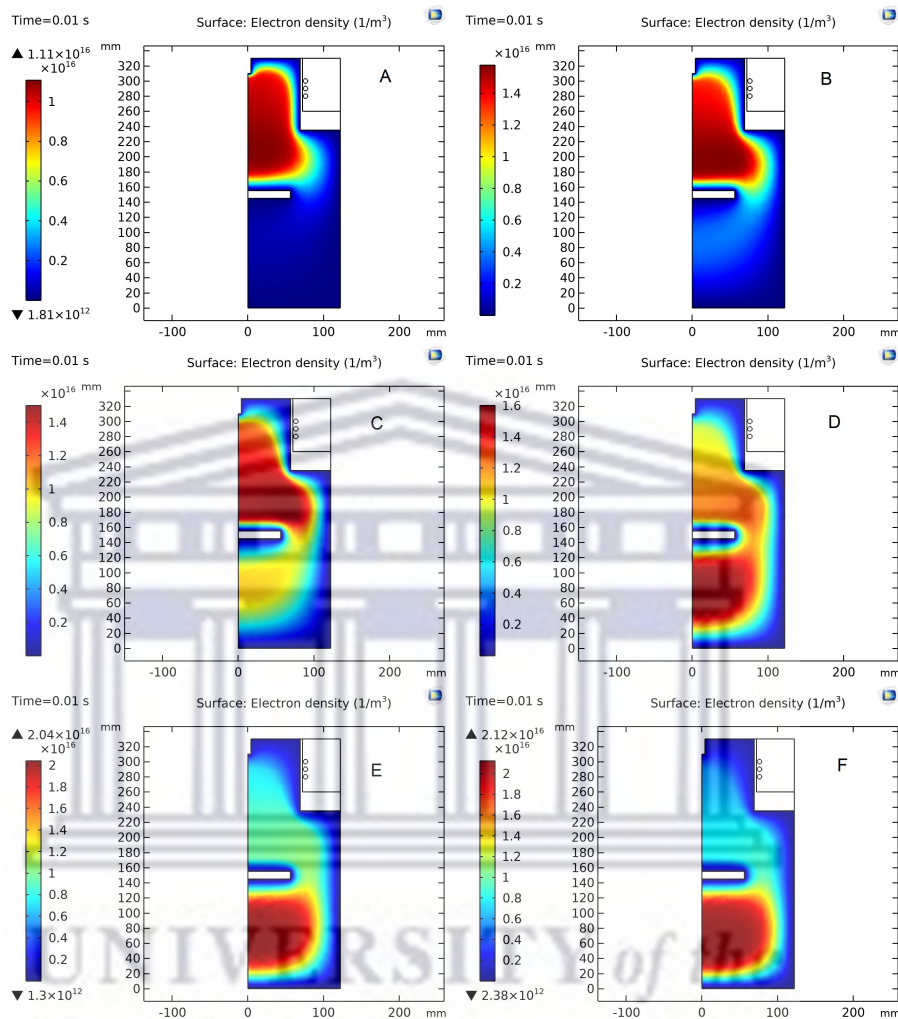
FIGURE 4.14: Electron Density for the pressure of 0.02 Torr, Frequency of 13.56 MHz and Coil Power in (A)-(F) of 100 to 600 W, respectively.

We also observe that in Figure 4.14, D F, for coil powers 400, 500 and 600 W, respectively, the electron density is higher below the substrate holder than in the excitation and extraction regions. However, in the excitation region, the value for the electron density is very similar for all coil powers. This value ranges roughly between 0.9 and 1.1×10^{16} electrons/m^3 for all coil powers. This suggests that in this region, to maintain the methane glow discharge plasma, the system requires a specific electron number density to maintain ignition through collisions with the neutral methane atoms. This inference can be further investigated by looking at the ion density profile for the varying coil power; this is done later in this section. Firstly, we compare the electron temperature for the various coil powers, shown in Figure 4.15.

The overall profile for the electron temperature is nearly identical inside the system, regardless of the coil power. The maximum value for T_e is always observed at the wall

nearest to the coil. A noticeable difference, however, is the sharp increase in the maximum value, which increases almost by a factor of 4 between the lowest (100 W) and highest (600 W) coil power.
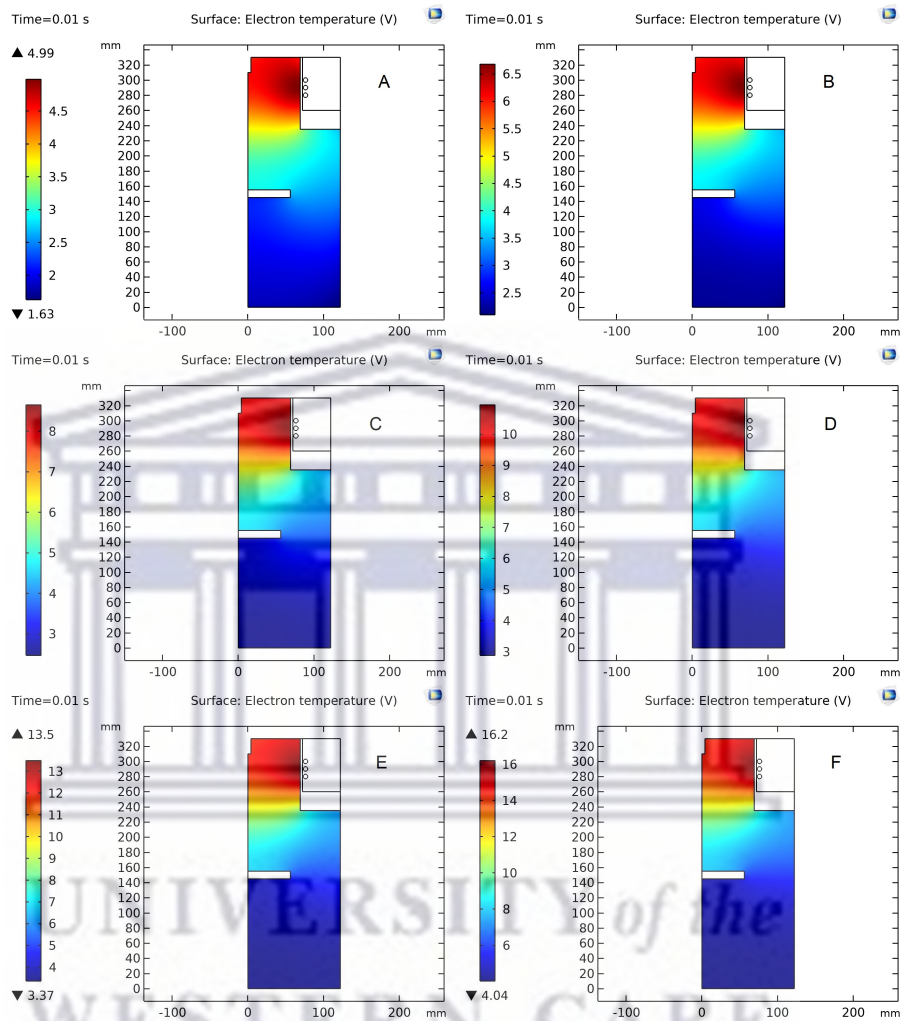
FIGURE 4.15: Plot of the power deposition into the plasma for the system with a pressure of 0.02 Torr, frequency of 13.56 MHz and Coil Power in (A)-(F) of 100 to 600 W, respectively.

It is encouraging to note that T_e remains relatively uniform in the system concerning the coil power, suggesting that the electric field remains slightly higher in the plasma bulk. Lastly, we look at the ion distribution density for CH_3^+ and CH_4^+, shown in Figure 4.16 and 4.17.

For both sets of ions, there is a slight increase in the ion number density as the coil power increases. There is a noticeable increase in the ion density for both CH_3^+ and CH_4^+ in the lower half of the system for coil powers of 400, 500 and 600 W, in D-F, for both Figure 4.16 and 4.17, respectively. At first glance, one might assume the ions are migrating; however, when ion density is compared to electron density plots in Figure 4.15, this is not the case. In Figure 4.15, D-E, we see that the electron density in the region below the substrate holder is relatively high.
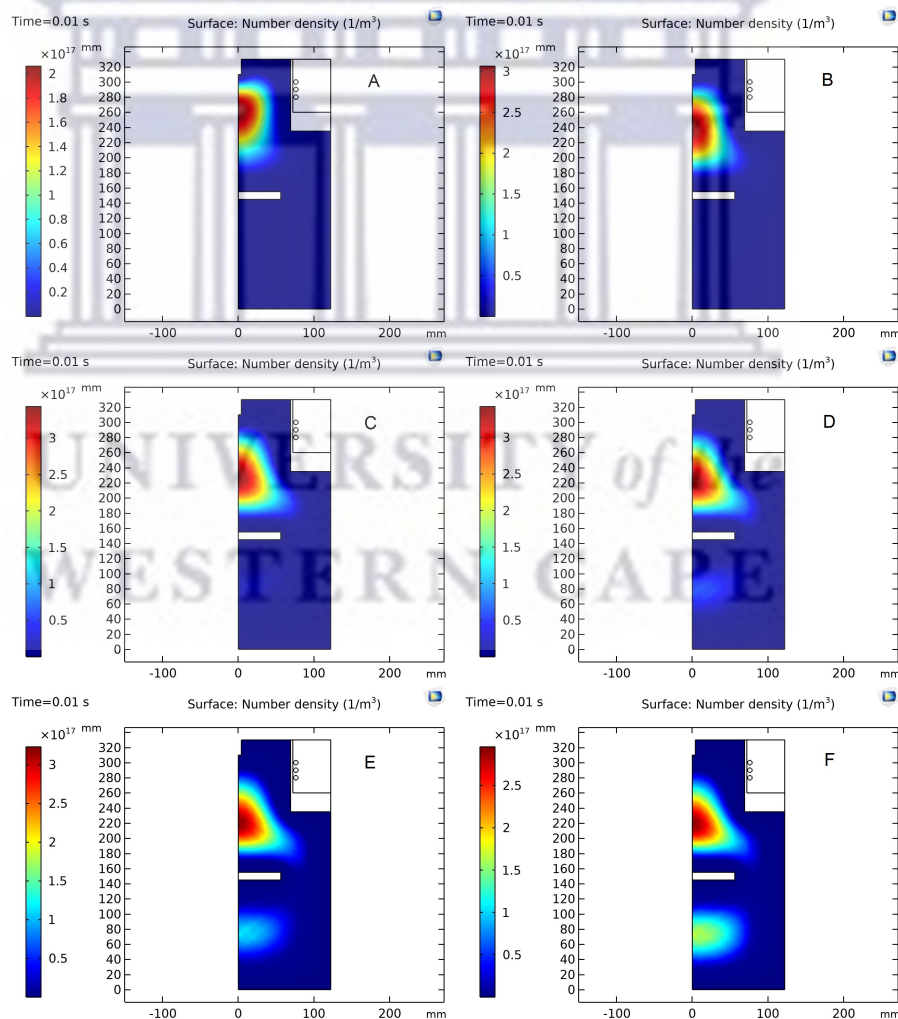
FIGURE 4.16: CH_3^+ Ion Density for a pressure of 0.02 Torr, Frequency of 13.56 MHz and Coil Power in (A)-(F) of 100 to 600 W, respectively.
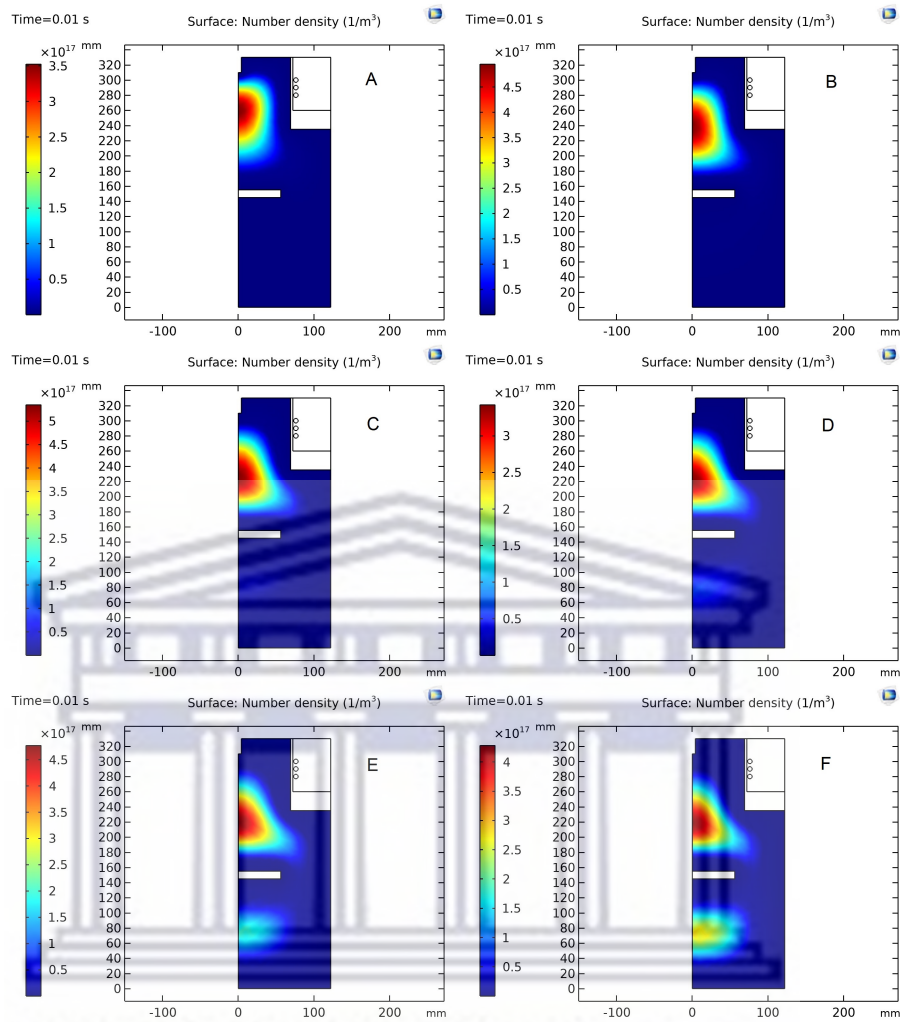
FIGURE 4.17: CH_4^+ Ion Density for a pressure of 0.02 Torr, Frequency of 13.56 MHz and Coil Power in (A)-(F) of 100 to 600 W, respectively.

This suggests, instead of the ions migrating from the excitation region, that secondary electron collisions with methane atoms occur here, leading to the production of the CH_3^+ and CH_4^+ ions. This would be something to be mindful of when deciding where to place your substrates relative to the excitation region in the system.

4.5.5 Surface Carbon Growth Rate as a Function of Varying Coil Power

The growth rate for surface carbon is determined using the dissociative reactions from Table 4.2. In these reactions, CH_3^+ and CH_4^+ are dissociated to surface carbon, C_s, and hydrogen radicals. The C_s are deposited on substrates forming the desired carbon layer. The growth rate is determined from the average height of the accumulated C_s on the substrate as a function of time. This study used the average height across the entire substrate holder to map the growth profile across its surface. The centre of the substrate holder is set as 0 mm, and its edge is 55 mm. The result of this mapping is presented in Figure 4.18. In Figure 4.18, the x-axis gives the length of the substrate holder (in mm), while the y-axis shows the accumulated growth height (in nm) across the surface of the substrate holder obtained for a fixed time of 8×10^{-3} s for different coil powers.
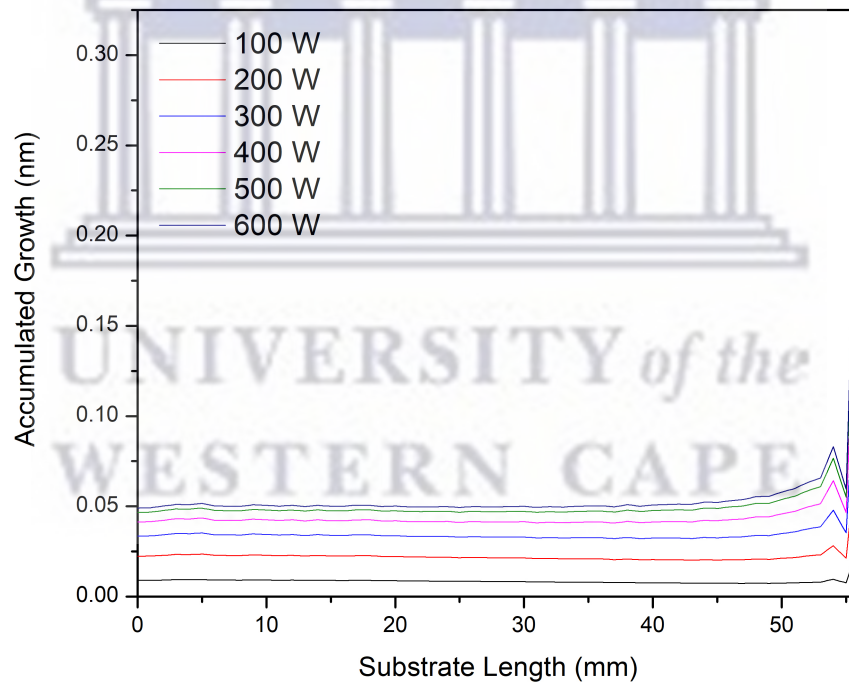
FIGURE 4.18: Accumulated surface Carbon growth over a fixed period at a pressure of 0.02 Torr, frequency of 13.56 MHz and coil powers ranging between 100 and 600 W.

In the accumulated growth plots for varying coil powers presented in Figure 4.18, it is evident that the growth profile is consistent and uniform across the surface of the substrate holder up to approximately 53 mm. After the 53 mm mark near the edge of the substrate holder, we identify a spike in the accumulated growth height, suggesting that more carbon is deposited in this region. This spike is a consequence of the model's

inability to resolve data near edges fully. A way to correct this would be to refine the mesh even further in this region to increase the resolution of the data. However, this will come at a computational cost. Given that the growth profile on the majority of the substrate holder, 95%, shows good homogeneity, this gives a good estimate of the substrate sizes that can be used in the reactor. To further explore the varying coil power on the growth profile of the system, the deposition rate as a function of coil power is calculated.

The result of these calculations is presented in Table 4.3. As expected from Figures 4.16 and 4.17, increasing the coil power increases the carbon deposition rate. This is a consequence of more CH_3^+, and CH_4^+ radicals present, which dissociate into the C_s deposited on the surface of the substrates.

TABLE 4.3: Deposition Rate for varying Coil Power.

Coil Power [W]	Average Height [nm]	Time [s]	Deposition Rate [nm/s]
100	7×10^{-3}	8×10^{-3}	0.87
200	22×10^{-3}	8×10^{-3}	2.75
300	33×10^{-3}	8×10^{-3}	4.13
400	41×10^{-3}	8×10^{-3}	5.13
500	46×10^{-3}	8×10^{-3}	5.75
600	49×10^{-3}	8×10^{-3}	6.12

4.6 Conclusion

A two-dimensional axisymmetric self-consistent fluid model for an inductively coupled plasma discharge has been used to understand better the dynamics of a high-purity methane discharge in the CADAR system. The simulation model has been solved with the finite element method (FEM) using COMSOL Multiphysics. The 2-D distributions of particle density, the electric properties and electron temperature are presented for a gas pressure of 0.02 Torr, frequency of 13.56 MHz and, initially, a power of 100 W. The values for the same parameters are then presented later for a varying power between 100 and 600 W. In this work, notable results obtained include:

- A slight increase in electron density, electron temperature and ion density is observed when coil power is increased.

- In the excitation region, the system maintains an overall electron density of around 1×10^{16} electrons/m^3 regardless of the coil power.

- The carbon deposited on the substrate is homogeneous, and a proportionality exists between coil power and the deposition rate and, consequently, the average height or thickness of the deposited layer.

- The plasma skin depth is around 40 mm.

The simulation results confirmed that coil power principally doesn't control the bulk plasma characteristics, but rather these are controlled by higher frequencies, as suggested in work by Rebiai *et al.*[166].

Future simulations will deal with improvements to the current model and can cover a broader range of input variables to create a results database. In addition, future simulations will account for the influence of convective fluxes on the plasma, including a gas flow in and out of the reactor.

Overall Conclusion

The work presented in this chapter has shown that the CADAR system at UWC can deposit the MWCNTs required for the nano-filler material to be used later in this work. As such, MWCNTs can now be produced as needed for polymer reinforcement applications.

Chapter 5

ABPBI Nanocomposite for Radiation Shielding

5.1 Abstract

Introducing nano-fillers to the polymer matrix can enhance the polymers inherent properties. Understanding the effects the introduction of the nano-filler has on the underlying polymer matrix is of great importance. Having the nano-filler well dispersed in the polymer matrix of the nanocomposite should, theoretically, provide better radiation shielding effectiveness over nanocomposites it is poorly dispersed. In this regard, the structural, compositional, thermal, and mechanical properties of the ABPBI polymer are investigated, both before and after the introduction of the MWCNTs, to ascertain the effects MWCNTs have on the polymer matrix of ABPBI. The ABPBI and ABP-BI/MWCNT nanocomposite membrane fabrication are provided in this chapter, with a complete comparison and analysis of the characteristics for both sets of composites.

5.2   Introduction

Polymer matrix composites have been studied extensively as part of a special group of high-performance, lightweight materials that play an important role in the current and emerging technologies for applications ranging from structural, electronic, and electro-magnetic shielding to smart materials[174]. These are typically prepared by dispersing a filler material, such as fibreglass or carbon fibres, in a polymer matrix. The resulting properties of these polymer matrix composites greatly depend on the amount of par-ticular filler material introduced into the matrix. However, nanoscale additives such as nano-clays[175], nanoparticles[176], and carbon nanotubes (CNTs)[177] can overcome the limitation related to the quantity of filler material used when they are dispersed in a polymer matrix. It has been shown that nanoscale additives can drastically change the properties of a polymer even at lower loading concentrations[177]. Of these, CNTs, namely single-walled carbon nanotubes (SWCNTs) and multi-walled carbon nanotubes (MWCNTs), have attracted the most attention as they inherently possess excellent mechanical, thermal, and electrical properties[178]. It is these properties that, by intro-ducing CNTs into a polymer matrix, are hoped to be inherited by the polymer. The resulting nanocomposite could thus be used in areas where affordable, lightweight, and multifunctional materials are required. To this end, we explore using poly(2, 5)benz-imidazole (ABPBI) filled with a nanoscale filler material for the system of applications mentioned above.

ABPBI, the simplest member of the polybenzimidazole (PBI) family, is the cheapest and most straightforward to produce in laboratory conditions[76]. ABPBI is predom-inantly used in high temperature proton exchange membrane (HT-PEM) applications for its excellent thermal stability and high ionic conductivity[9]. ABPBI membranes are synthesised through a relatively simple condensation reaction of the 3,4-Diaminobenzoic acid (DABA) monomer in Methansulfonic acid (MSA), which offers a cost-effective alter-native to other complex polymers while maintaining comparable or improved application efficiencies. ABPBI intrinsically has relatively high mechanical and thermal properties compared to other simple polymeric materials such as polyethylene[179]. With the addi-tion of CNTs to the ABPBI polymer matrix during the polymerisation process, in-situ polymerisation, the goal is to enhance these intrinsic properties resulting in a more robust polymer nanocomposite to serve a more comprehensive ray of applications. Al-though ABPBI is synthesised from the DABA monomer dissolved in MSA, various other chemicals can be introduced to the polymer reaction mixture during the condensation process resulting in ABPBI membranes with varying properties. One such example can be found in the work done by Kang *et al.*[178]. This work introduces aqueous hy-drochloric acid (HCl) into the reaction mixture to stabilise the condensation process.

While still producing ABPBI membranes with similar properties to that obtained by using the standard synthesis method containing only DABA, MSA and polyphosphoric acid (PPA), adding HCl drastically increased the time taken to recrystallise DABA into ABPBI. This method also decreased the total product yield by 30%, compared to the standard procedure, without significantly improving the intrinsic properties of the resultant ABPBI membrane. As such, in this work, a single-step condensation synthesis procedure was used to fabricate the ABPBI membranes with the in-situ addition of MWCNT to produce the ABPBI/MWCNT nanocomposites.

Carbon nanotubes (CNTs) are an efficient filler material for polymers as they enhance the properties of the polymer[180, 181]. Some unique properties of CNTs that are hoped to be inherited by the polymer during the *in-situ* polymerisation process include; high thermal and electrical conductivities, high tensile strength and a low thermal expansion coefficient[182]. The resulting polymer composite achieves improved thermal stability and mechanical strength over its pristine counterpart by inheriting these properties from the CNT filler material.

Herein, we report an *in-situ* polymerisation of ABPBI reinforced with MWCNTs, at different load weighting percentages (wt. %) to form ABPBI/MWCNT nanocomposites. The resultant nanocomposites are then evaluated for their thermal and mechanical properties compared to the pristine ABPBI polymer. Also reported are the compositional and structural changes from adding MWCNTs to the polymer matrix.

5.3 Methods

5.3.1 Materials

The reagents and solvents used in this work are the AB monomer 3,4-Diaminobenzoic acid (DABA), Phosphorus pentoxide (99%-P_2O_5), Methanesulfonic acid (99%-MSA), multi-walled carbon nanotubes (MWCNT), Sodium Hydroxide (0.1 M - NaOH) and Methanol (99%-CH_3OH). All reagents and solvents were purchased from Sigma-Aldrich and used as received unless otherwise specified.

5.3.2 Synthesis of Poly(2,5)benzimidazole

Poly(2,5)benzimidazole (ABPBI) was synthesised in a polymerisation medium containing MSA and P_2O_5, as illustrated in Figure 5.1. Into a 150 ml resin flask equipped with a magnetic stirrer and nitrogen inlet and outlet, P_2O_5 (1.5 g) and MSA (10 ml) were

added and stirred under a dry nitrogen purge at 150°C for 1 hour until a homogeneous solution was obtained. To avoid drastic foaming of the solution DABA (1 g) was added to the reaction mixture and allowed to mix for 30 minutes. The temperature was then increased to 200°C, and the reaction mixture was left to stir for an additional 1 hour, after which an increase in the polymer solution viscosity was observed. The hot polymer solution was then poured into glass vials, cooled, and stored under a vacuum for later use.
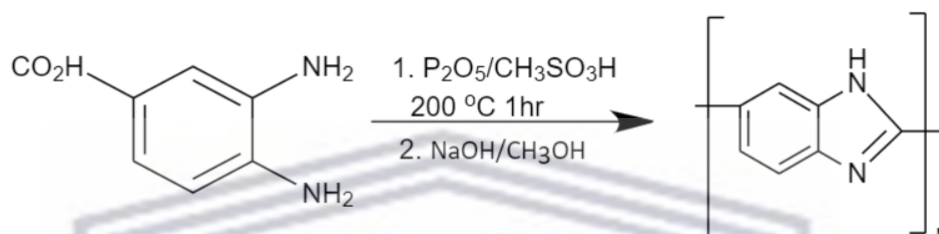
FIGURE 5.1: Synthesis of ABPBI from DABA in a reaction mixture of MSA and P_2O_5

5.3.3 In Situ Polymerization of 3, 4-Diaminobenzoic Acid with 1 and 3 wt. % MWCNT Load

In the same setup as for ABPBI synthesis, P_2O_5 (1.5 g), MSA (10 ml) and DABA (1 g) were mixed to form the polymer solution. Before the temperature was increased from 150°C to 200°C, as in the ABPBI synthesis, MWCNT (10 mg or 30 mg) was added to the reaction mixture to form the polymer solutions for the different 1 and 3 wt. % MWCNT load concentrations. The solution was again left to stir for 1 hour before being placed in glass vials for storage.

5.3.4 Membrane Casting

Membranes were cast for each composite sample. The resultant homogeneous polymer solutions, obtained from the previously described synthesis methods, were cast on a levelled hot-plate into custom-made glass moulds having dimensions 50×10×1 mm. The mould solution was then heated, inside a well-ventilated fume hood, to 180°C for 1 hour and then at 200°C for 2 hours to slowly evaporate MSA out of the polymer membranes slowly. The heating process continued until no visible elevation of MSA was observed from the films. The glass moulds, while hot, were immersed in deionised water to detach the resulting membranes from the moulds. The membranes were then removed from the water and placed into a purification solution containing 0.1 M-NaOH, CH_3OH and deionised water to remove the residual phosphoric acid in the membranes. The solution

with the membranes was stirred using a magnetic stirrer for three days, changing the solution every 24 hours. The membranes were then rinsed for 4 hours in deionised water to remove any residual purification mixture from the membrane. The purified membranes were then sandwiched between filter paper to keep them flat and dried under vacuum for four to five days.

5.3.5 Characterisation

The fabricated ABPBI and ABPBI/MWCNT composites were characterised by Fourier-Transform Infra-Red (FTIR) spectroscopy, X-ray Diffraction (XRD) spectroscopy, Thermogravimetric Analysis (TGA), Differential Scanning Calorimetry (DSC) and Tensile strength testing for mechanical properties.

FT-IR was performed on a Nicolet iS10 FTIR spectrometer (Thermo Fisher) on the pre- and post-irradiation composites in the range 400 - 4000 cm^{-1} with a resolution of 2 cm^{-1}. The resulting spectra for all composites were evaluated and compared, including the assignments of the observed peaks.

XRD was performed on a Scintag DMS2000 diffractometer on all composites. The instrument parameters used were Cu$K\alpha$1 radiation ($\lambda = 1.54184$ Å) operating at a voltage of 30 kV and a current of 10 mA, in the 2θ-range of 5-65°. The spectra obtained were evaluated and compared to identify the characteristic peaks for ABPBI and any changes in these peaks due to the addition of MWCNT.

TGA was performed on a Q500 from TA Instruments to determine the composite's weight loss as a function of increasing temperature. The analysis was performed in an inert N$_2$ atmosphere for a temperature range between 25-600°C at a ramp rate of 10°C min^{-1}. The results for all composites were evaluated and compared.

DSC was performed on a Q20 from TA Instruments to measure the change in the composite's heat flow as a function of temperature. The analysis was performed in an inert N$_2$ atmosphere for a temperature range between 25-400°C at a ramp rate of 10°C min^{-1}. All composites used for the study had a mass of approximately 10 mg.

Tensile strength tests were performed with an Instron 5548 Micro Tester following ASTM D638-10 standards on only the pristine ABPBI and ABPBI/MWCNT 1 wt. % composites. The results of these tests are compared to deduce whether adding MWCNTs increases the mechanical strength of the ABPBI polymer matrix.

5.4 Results and Discussion

5.4.1 Fourier Transform Infrared Spectroscopy

Fourier Transform Infrared (FTIR) Spectroscopy was used to investigate the molecular composition of the ABPBI and ABPBI/MWCNT nanocomposites at different MWCNT wt. % loads. The FTIR spectra for the pristine ABPBI and ABPBI/MWCNT of 1 and 3 wt. % composites are presented in Figure 5.2, with the associated bands for the polybenzimidazole backbones provided in Table 5.1, by FTIR studies conducted by Musto *et al.*[183] and Kang *et al.*[178].
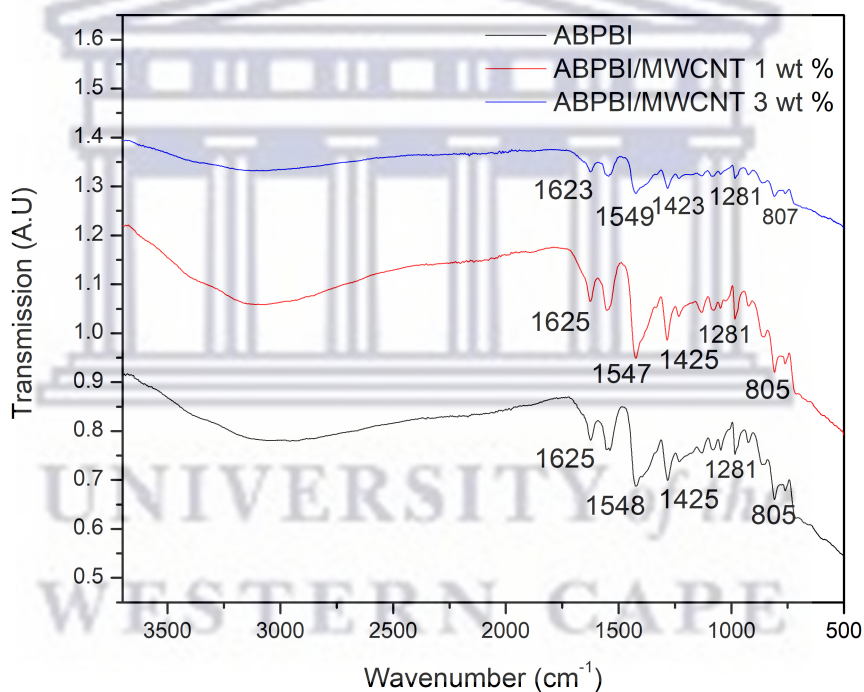
FIGURE 5.2: FTIR spectra of pristine ABPBI and ABPBI/MWCNT composites.

For the pristine ABPBI, in the region between 3750 and 2500 cm^{-1}, we observe a band around 3666 cm^{-1} assigned to O-H stretching from absorbed water, a band around 3135 cm^{-1} assigned to hydrogen bonded N—H stretching and lastly, a band at 3091 cm^{-1} assigned to C—H stretching. ABPBI polymers are very hygroscopic, giving rise to the absorbed water peak around 3500 cm^{-1} even after drying at 100°C. The characteristic polybenzimidazole C=C and C=N stretching bands appear at 1625 cm^{-1}, and the breathing mode of the imidazole ring appears at 1281 cm^{-1}. Some other bands identified include; the band at 1548 cm^{-1} assigned to ring vibrations due to conjugation between benzene and imidazole rings, the band at 1425 cm^{-1} assigned to in-plane deformation

of the benzimidazole rings. The band at 1227 cm^{-1} is assigned to the in-plane deformation of C—H, and the band at 805 cm^{-1} is assigned to the out-of-plane bending of the benzene rings.

The FTIR spectra for the MWCNT loaded composites show similar spectra to that of the pristine ABPBI membrane, confirming that the ABPBI structure is intact after blending. A notable difference in the spectra stems from a decrease in the relative intensities of the peaks observed for the ABPBI/MWCNT 3 wt. % composite. This is most evident in the region between 3750 and 2500 cm^{-1}, where we observe a gradual decrease in intensity as the MWCNT loading percentage increases. A negligible shift of < 3 cm^{-1} in the band peak positions for the nanocomposites was also observed, but these shifts generally fall within 1-3 wave numbers to that of the pristine ABPBI. No new discernible peaks were identified in the spectra for the ABPBI/MWCNT nanocomposites. Of notable importance across all three polymer composites is the absence of the strong MSA band, which would present at 2940 cm^{-1}, indicating the complete evaporation of the solvent during the membrane casting.

TABLE 5.1: Infrared Spectra Analyses of poly(2,5)benzimidazole and associated composites.

Wave Number (cm^{-1})			
ABPBI	**MWCNT 1 wt. %**	**MWCNT 3 wt. %**	**Peak Assignment**
805	805	805	Out-of-plane C—H bending of the benzene rings.
1281	1281	1281	Breathing mode of the imidazole rings.
1227	1231	1232	In-plane C—H deformation
1425	1425	1423	In-plane deformation of benzimidazole rings.
1548	1547	1549	Ring vibration due to conjugation between benzene and imidazole rings.
1625	1625	1623	C=C/C=N stretching.

5.4.2 X-ray Diffraction

X-ray diffraction (XRD) was used to perform structural analysis on the ABPBI and ABPBI/MWCNT nanocomposites, presented in Figure 5.3. XRD was performed on 1×1 cm membrane samples of the pristine ABPBI, and the MWCNT loaded nanocomposites dried at 100°C for two days.

All three polymer composites are semi-crystalline, evident by the broad diffraction peak around $2\theta = 26°$, considered the characteristic peak for this material[178]. In the case of the pristine ABPBI, the characteristic peak is centred at $2\theta = 26.68°$ with respective d-spacing = 3.34 Å. This is assigned to the stacking of ABPBI chains in the polymer matrix[184]. A second characteristic peak at $2\theta = 10.56°$, corresponding to a d-spacing = 8.42 Å, also appears in the spectra for the pristine ABPBI membrane. This is attributed to the crystallisation tendency of the polymer when solid membranes are formed[185, 186]. No additional peaks were identified in the spectra.
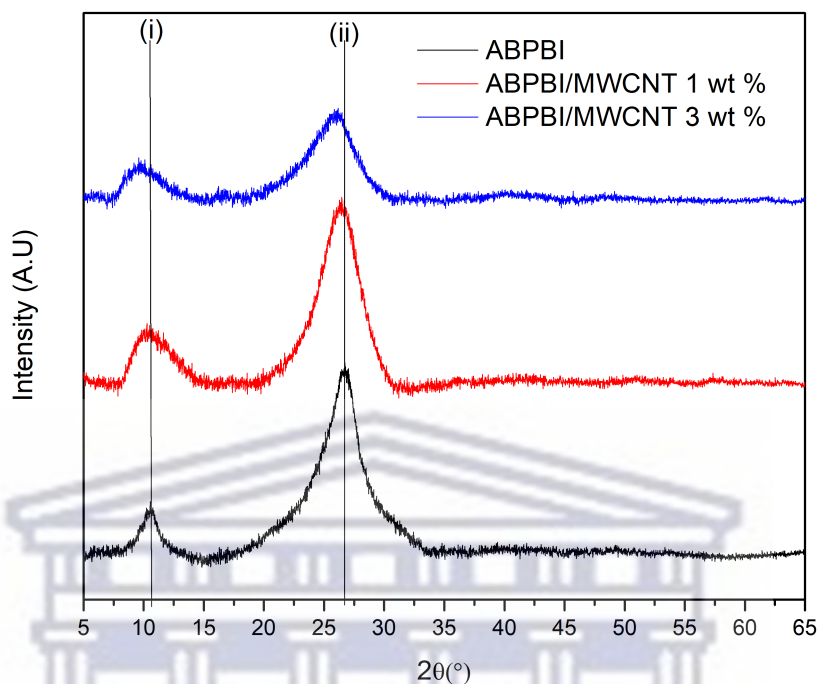
FIGURE 5.3: XRD patterns of pristine ABPBI and ABPBI/MWCNT composites.

The addition of MWCNTs, of different wt. %, to the ABPBI polymer matrix, displayed similar XRD patterns as that of the pristine ABPBI membrane. Both nanocomposites displayed the two characteristic peaks around $2\theta = 10°$ and $2\theta = 26°$, respectively. When looking at the first set of peaks, marked by line (i) in Figure 5.3, we observe a slight shift in the interplane distance across all nanocomposites. The $2\theta = 10.37°$ and $9.68°$ peaks of the ABPBI/MWCNT 1 and 3 wt. % composites are observed, which correspond to d-spacing = 8.53 and 9.14 Å, respectively. The peaks around $2\theta = 10°$ also show broadening across all nanocomposites, suggesting a decrease in the crystal size with adding more MWCNT into the polymer matrix. A similar shifting and peak broadening phenomenon is observed for the second characteristic peak centred at around $2\theta = 26°$, marked by line (ii) in Figure 5.3. These peaks for the nanocomposites are located at $2\theta = 26.34°$ (d-spacing = 3.38 Å) and $25.97°$ (d-spacing = 3.43 Å) for the ABPBI/MWCNT 1 and 3 wt. % composites, respectively. Moreover, no peaks for MSA were observed across the three membranes, which would present sharp, narrow peaks in the spectra due to its disruption of the molecular orientation[187].

To further explore the peak broadening observed in the MWCNT loaded composites, the Williamson-Hall method was used to calculate the crystallite sizes and the intrinsic strain, which were then compared to the pristine ABPBI polymer. Using the Uniform

TABLE 5.2: XRD analysis of poly(2,5)benzimidazole and associated composites.

Samples	i		ii	
	2 (°)	d-Spacing (Å)	2 (°)	d-Spacing (Å)
ABPBI	10.56	8.42	26.68	3.34
ABPBI/MWCNT 1 wt. %	10.37	8.53	26.34	3.38
ABPBI/MWCNT 3 wt. %	9.68	9.14	25.97	3.43

deformation model (UDM), which considers strain that is isotropic in nature[188], we obtain the relation:

$$\beta Cos(\theta) = \varepsilon 4 Sin(\theta) + \frac{K\lambda}{L} \tag{5.1}$$

where β is the full-width at half of the maximum intensity of the diffraction peaks, ε is the intrinsic strain, K is the dimensionless shape factor, λ is the x-ray wavelength, and L is the crystallite size. Equation 5.1 is in the form of a straight-line equation. As such, by plotting $4Sin(\theta)$ along the horizontal axis against $\beta Cos(\theta)$ along the vertical axis, the slope of the plot gives the intrinsic strain of the composites while the y-intercept is used to calculate the crystallite sizes. The results of the Williamson-Hall analysis, using the UDM for the composites, are presented in Table 5.3, which contains the associated crystallite size and value of the intrinsic strain for each composites.

The Williamson-Hall analysis shows that the composites' intrinsic strain increases with the increase of the MWCNT wt. % load in each composite. This is because the MWC-NTs induce strain on the underlying ABPBI chains, increasing as additional MWCNTs are added to the ABPBI polymer matrix. Concerning the crystallite sizes, a decrease in crystallite size is observed in the ABPBI/MWCNT 1 wt. % composite. This decrease accounts for the broadening observed in the XRD spectrum for the peaks around $2\theta = 10°$ and $26°$ for this composite. Conversely, the crystallite size of the ABPBI/MWCNT 3 wt. % composite showed an increase of 0.26 nm at this MWCNT load percentage compared to the pristine ABPBI polymer. This suggests an expansion of the underlying ABPBI polymer matrix at this MWCNT wt. % load, which gives rise to the shifting of the two characteristic peaks to lower 2θ values.

TABLE 5.3: Williamson-Hall analyses estimating strain and crystallite size for ABPBI and its associated MWCNT loaded composites.

Sample	Crystallite Size, L (nm)	Strain, ε
ABPBI	3.05	0.01586
ABPBI/MWCNT 1 wt. %	2.62	0.01928
ABPBI/MWCNT 3 wt. %	3.31	0.04369

5.4.3 Thermal Properties

The thermal properties of the polymer composites were investigated upon completion of the spectroscopic analysis. The two techniques employed in this regard were TGA and DSC. Details of the analysis for these techniques are presented in the following sections.

5.4.3.1 Thermogravimetric Analysis

TGA was performed to determine the thermal stability of the ABPBI and ABPBI/MWCNT nanocomposites. TGAs were performed under a dynamic N_2 atmosphere for pristine ABPBI membrane, ABPBI/MWCNT 1 wt. % and ABPBI/MWCNT 3 wt. % nanocomposites. The TGA analysis for the polymer composites was conducted from room temperature to 600°C at a temperature ramp rate of 10°C min^{-1} is presented in Figure 5.4.
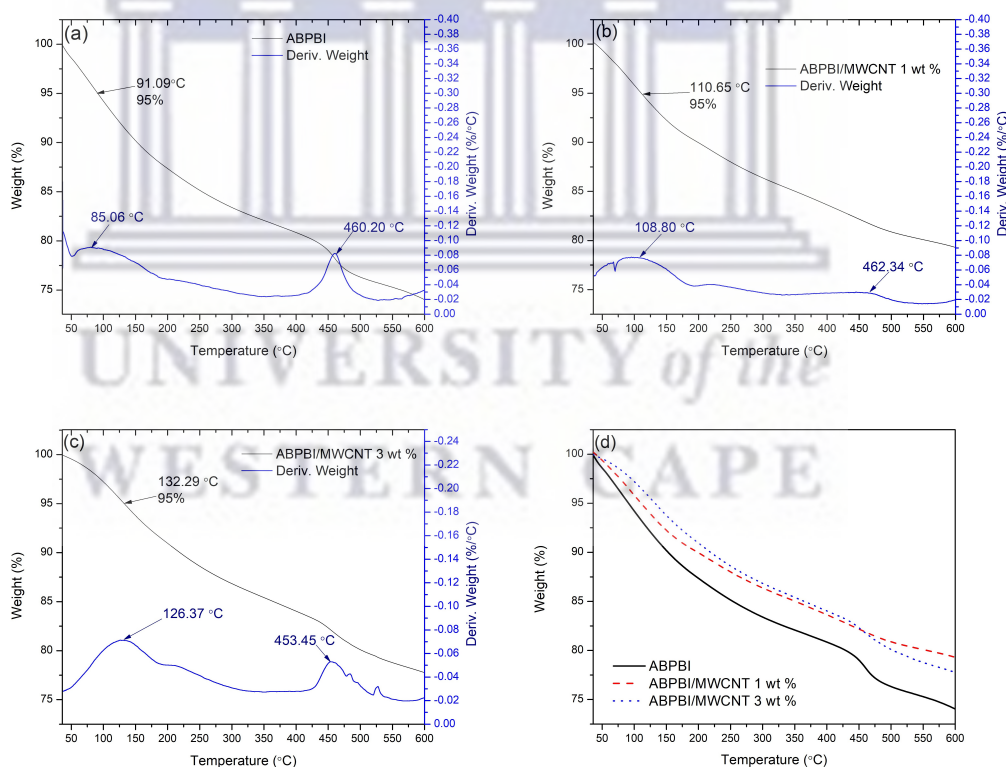
FIGURE 5.4: TGA plots of Pristine ABPBI (a), ABPBI/MWCNT 1 wt. % (b) and ABPBI/MWCNT 3 wt. % (c) composites with their corresponding Deriv. Weight plots. An overlay of the TGA curves for all nanocomposites is presented in (d).

All three composites displayed very similar weight loss profiles as a function of temperature. A trend observed from the TGA plots was that an increase in the MWCNT loading increased the thermal stability of the composites. The Deriv. Weight plots for

all composites show two distinct event peaks for all TGA curves, one around 100°C and the other around 460°C.

The first set of peaks corresponds to a weight loss of approximately 5% ($T_{d5\%}$), which occur at 91.09, 110.56 and 132.29°C for the pristine ABPBI, ABPBI/MWCNT 1 wt. % and ABPBI/MWCNT 3 wt. % composites, respectively. These peaks are also believed to arise from loosely bound water evaporating from the composites, resulting in the initial weight loss observed between 25°C and 150°C. The second set of peaks, at around 460°C, is believed to show a transition temperature for the composites, given that corresponding temperatures are close to the proposed glass-transition temperature ($T_g \approx$ 430°C) for ABPBI[87]. In the pristine ABPBI composite, this peak appeared around 460.20°C, which presented a sharp degradation in the TGA curve for the composite. Similarly, the MWCNT loaded composites displayed sharp degradation at temperatures of 462.36°C and 458.34°C for the ABPBI/MWCNT 1 wt. % and ABPBI/MWCNT 3 wt. %, composites, respectively. Since this set of peaks is attributable to the T_g for the composites, it suggests that adding MWCNTs to the ABPBI polymer matrix does not increase the glass-transition temperature of the polymer composites. However, it does increase the overall temperature stability of the composite, evident from the slower degradation observed from the composites containing the MWCNT compared to the pristine ABPBI polymer. This phenomenon was also observed in a proton irradiation study of PMMA loaded with MWCNTs conducted by Li *et al.*[109].

5.4.3.2 Differential Scanning Calorimetry

The second technique used concerning thermal properties was Differential Scanning Calorimetry (DSC), which measured enthalpy changes due to changes in the polymer composites' physical or chemical properties. The DSC analysis was performed under a dynamic N_2 atmosphere for all the nanocomposites. Figure 5.5 shows the DSC curves from room temperature to 400°C at a temperature ramp rate of 10°C min^{-1}.

From the DSC curves in Figure 5.5 for the pristine ABPBI membrane, we observe a strong endothermic peak at 123°C and a second smaller peak at 229°C. These peaks are attributed to the loss of absorbed water from the structure of the membrane[187]. Due to the hygroscopic nature of ABPBI, water is absorbed and loosely bound between the fibres of the polymer chains and is easily removed by heating the ABPBI membranes, thereby resulting in the endothermic peaks observed in the DSC curves. The value of the endothermic peaks for all three composites is given in Table 5.4. After the second endothermic peak, the curve remains relatively featureless, an expected result for the temperature range used in the analysis. Generally, DSC is used to identify a material

compound's glass-transition temperature (T_g) and decomposition temperature ($T_{d100\%}$). T_g and $T_{d100\%}$ are not identifiable in our DSC curves as polybenzimidazole-based membranes, which have an all-aromatic structure, have a relatively high glass-transition temperature ($T_g \approx 430°C$) and a high decomposition temperature ($T_{d100\%} > 600°C$[87]). DSC could not be performed at higher temperatures due to instrument limitations; however, the current temperature range gives adequate and insightful information about the composites' heat-flow characteristics. Furthermore, the temperature range used for the DSC analysis falls outside the maximum temperature the composites would be subjected to in the LEO environment, which at its maximum would be 60°C.

TABLE 5.4: Endothermic peak values (T) of pristine ABPBI and ABPBI/MWCNT composites.

Sample	Temperature (°C)
ABPBI	123 and 229
ABPBI/MWCNT 1 wt. %	208
ABPBI/MWCNT 3 wt. %	98 and 210

The DSC curves for ABPBI/MWCNT composites with 3 wt. % MWCNT load showed similar features to that of the pristine ABPBI membrane, with two endothermic peaks
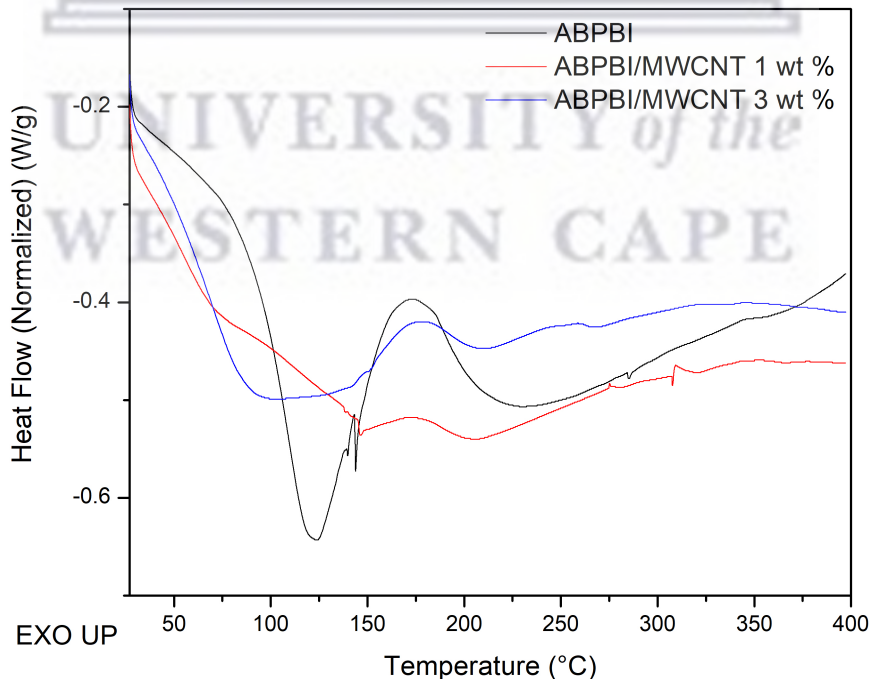
FIGURE 5.5: DSC curves for the pristine ABPBI and MWCNT loaded composites, performed in N_2 atmosphere. Exothermic heat-flow in the positive y-direction (EXO UP).

in its curve. Both peaks appear at lower temperatures and relatively lower intensities than the pristine ABPBI membrane. This would suggest that the polymer becomes less hygroscopic at this particular MWCNT loading percentage. Interestingly, the ABP-BI/MWCNT 1 wt. % shows the most stable DSC curve concerning the endothermic peaks. This suggests a decrease in the uptake of loosely bonded water in the membrane structure, which consequently indicates a reduction in the hygroscopic nature of the membrane at this MWCNT load percentage. The DSC curve for the ABPBI/MWCNT 1 wt. % membrane only shows a small endothermic peak at 208°C, after which the rest of the curve remains relatively featureless.

5.4.4 Tensile Strength Tests

This section reports tensile strength tests conducted on the pristine ABPBI and ABP-BI/MWCNT 1 wt. % composite membranes to ascertain their mechanical properties. We elected to perform these tests on the ABPBI/MWCNT 1 wt. % composites only, to establish a baseline enhancement of the composite's tensile strength after the addition of the MWCNT's into it's matrix. From this baseline, an appropriate loading percentage can be determined based on the tensile strength requirements of the final composite. These tests were conducted at One Eighty Metallurgy on an Instron 5548 Micro Tester following ASTM D638-10 (TYPE IV) standards. Before loading the samples for testing, samples are cut into dog bone shapes (See Figure 3.8) to precise specifications as outlined by the above standards. Multiple samples of the same kind are loaded into the tester, and the sample's mechanical properties are determined by averaging out the obtained values over the number of samples tested. As such, for this study, four samples were used for the pristine ABPBI, while five were used for the ABPBI/MWCNT 1 wt.% composite. Images of the samples before and after testing can be found in Figures 5.6 and 5.7, respectively.
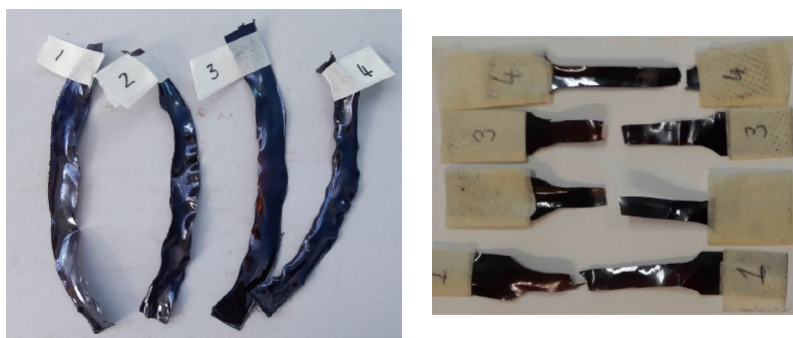
FIGURE 5.6: ABPBI pre-tensile strength testing (left) and ABPBI post-tensile strength testing (right).
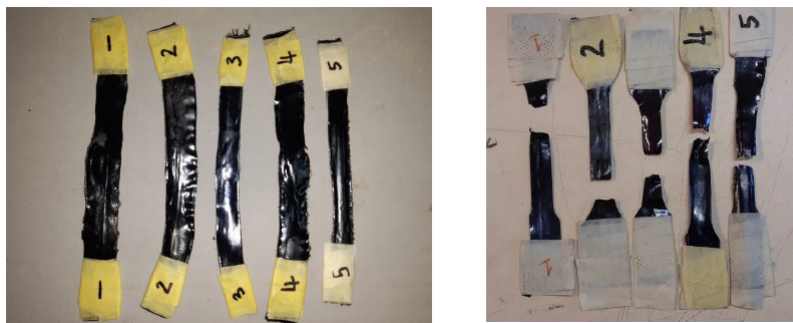
FIGURE 5.7: ABPBI/MWCNT 1 wt. % pre-tensile strength testing (left) and ABP-BI/MWCNT 1 wt. % post-tensile strength testing (right).

The point of failure for each membrane during its respective test can be seen in Figures 5.6 and 5.7. During each test run, the mechanical properties of each sample are collected. These include the sample's; yield strength, tensile strength, percentage elongation, and Young's Modulus. The results of the testing for these parameters are presented in Tables 5.5 and 5.6, respectively.

TABLE 5.5: Tensile Test Results (ABPBI)

Sample No.	Yield Strength (MPa)	Tensile Strength (MPa)	Per Elongation (%)	Young's Modulus (GPa)
1	16	40	26	1.50
2	22	44	19	1.10
3	19	43	22	2.07
4	28	55	22	2.58
Average	**20.50**	**41.75**	**21.50**	**1.67**

TABLE 5.6: Tensile Test Results (ABPBI/MWCNT 1 wt. %.)

Sample No.	Yield Strength (MPa)	Tensile Strength (MPa)	Per Elongation (%)	Young's Modulus (GPa)
1	45	68	7.5	3.44
2	44	65	8.4	3.46
3	26	62	36	2.85
4	28	55	22	2.58
5	41	76	42	3.77
Average	**36.8**	**65.2**	**23.18**	**3.22**

When comparing the results in each table, we see the obtained values for the ABP-BI/MWCNT 1 wt. % composite has increased significantly over values obtained from the ABPBI membrane tests. This suggests that the addition of MWCNTs to the ABPBI polymer matrix has indeed improved the mechanical properties of the underlying polymer matrix. Looking specifically at Young's Modulus, which is the stiffness of a material, we see that the value has doubled from 1.67 GPa (for ABPBI) to 3.22 GPA (for ABP-BI/MWCNT 1 wt. %) with just a 1 wt. % MWCNT addition to the ABPBI polymer matrix. Nayak *et al.*[142] reported a Young's Modulus value of 0.9±0.13 GPa for the pristine ABPBI membrane, which is slightly lower than the value obtained from our work. The difference between the two values could result from different acid doping levels in the membranes of Nayak and his team.

5.5   Conclusion

In this work, we explore the fabrication of a polymer matrix composite. The composite in question is poly(2, 5)benzimidazole (ABPBI) reinforced with multi-walled carbon nanotubes (MWCNTs) to form ABPBI/MWCNT nanocomposites with different MWCNT load wt. %.

From the result presented, we determined that adding of MWCNTs made the composites less hygroscopic, with the characteristic molecular fingerprint peaks of the ABPBI matrix still present. Also, adding MWCNTs to the polymer matrix changed the composite's crystallite sizes and intrinsic strain. An increase in the MWCNT load resulted in an increase in the intrinsic strain within the composites. The thermal analysis, TGA and DSC, showed improved thermal stability in the MWCNT loaded composites over the pristine ABPBI membranes. Lastly, we demonstrated that adding MWCNTs to the polymer matrix of ABPBI, even in small quantities, significantly improves the mechanical properties of the polymer.

Having shown that the ABPBI polymer membrane responds favourably to the MWCNT filler material, it is now possible to further explore the intended application for this nanocomposite.

Chapter 6

ABPBI for Proton Radiation Shielding

6.1 Abstract

When planning for any space mission, shielding against ionising radiation is essential. Polymers, combined with a nano-filler material to reinforce and enhance the polymer properties, can provide a sufficient radiation shielding function with lower weight and less secondary radiation generation than traditional shielding materials such as lead. In this study, poly(2, 5)benzimidazole/multi-walled carbon nanotube (ABPBI/MWCNT) nanocomposites were fabricated and evaluated for their proton radiation shielding capabilities in the low-earth orbit (LEO) region of space. The radiation shielding effectiveness of the ABPBI/MWCNT nanocomposites was experimentally evaluated by comparing their proton transmission properties and their secondary neutron generation to that of pristine ABPBI. The results showed that adding MWCNTs to the ABPBI matrix further reduced the secondary neutrons generated by the pristine ABPBI. In addition, the depth profile showed that proton penetration into the bulk of the composite decreased as the MWCNT weight percentage loading increased. The MWCNT-loaded composites showed improved resistance to proton radiation-induced damage compared to the pristine ABPBI membrane. This was evident from the visible damage observed in the SEM micrographs for the pre-and post-irradiated ABPBI membranes. Furthermore, composites containing MWCNTs displayed improved thermal stability over the pristine ABPBI for both pre-and post-irradiation composites. The overall characteristics presented have shown ABPBI/MWCNT nanocomposites as an effective material for application in the space industry.

∗ *The contents of this chapter were published in APL Materials, Volume: 11, Issue: 7: DOI: 10.1063/5.0156686. Modifications were made in this chapter to suit the thesis presentation style.*

6.2 Introduction

The space environment contains many hazards that could be detrimental to space travel, among which is, but is not limited to, space radiation. For outer space activities, space radiation primarily consists of electrons and protons, solar particle events (SPEs) and galactic cosmic radiation (GCR) [43]. The energy of the radiation particles ranges between 1 MeV/nucleon to 10 GeV/nucleon. For missions closer to Earth, namely in the low-earth orbit (LEO) region, the particle radiation mixture changes significantly concerning species and energies. In LEO, the radiation mixture mainly consists of atomic oxygen (80%), with the remaining consisting of protons, electrons and molecular nitrogen[189]. Atomic oxygen is known for its corrosive effects on the outer components of the spacecraft. At the same time, protons and electrons proved most detrimental to the spacecraft's electrical components and astronauts on human-crewed missions to this region of space. Protons, in particular, pose the most significant risk to the electrical components of spacecraft as, through their ionising effects characterised by their generation of secondary neutrons when interacting with materials, they induce a phenomenon known as bit flipping in the CPUs of these components control units[190]. On earth, random bit flips occur, on average, at a rate of 4 flips/gigabyte per month. This rate significantly increases the further away from the Earth's surface you travel.

Consequently, spacecraft would have to be fitted with multiple control units for redundancy to negate the effects of incorrect data obtained from the affected components or complete failure. This solution adds significant weight to the overall payload, increasing the overall expenditure of the space mission. A more practical solution would be the addition of materials to the spacecraft that could shield against this ionising radiation and enhance neutron attenuation to improve protection against the harmful effects of radiation. Currently, materials used for shielding purposes include aluminium (Al), high-density polyethylene (HDPE) and water. The use of these materials has disadvantages such as low thermal resistance (HDPE), high atomic number (Al) and complex maintenance systems (water), which result in heavy loads and increased costs in space missions. For simple kinematic considerations of particle collisions, low atomic number (low-Z) materials are known to be efficient in shielding against particle radiation. However, they suffer inferior material properties compared to metallic counterparts.

However, conventional metallic shielding materials suffer from weight issues and secondary neutron and gamma radiation generation associated with their interactions with proton irradiation. Materials with a high hydrogen content, such as low-Z polymers, have thus become an attractive alternative to conventional shielding materials as these address both the issues of weight and secondary radiation generation.

Limitations in low-Z polymers compared to their metallic counterparts are that they have lower mechanical strength and lower electrical and thermal conductivities. Various studies have investigated different polymer composites to find lightweight alternatives to metallic alloys with sufficient strength and shielding performance [43, 191, 192]. Nano/micro-sized fillers can be introduced into the polymer matrix, improving mechanical strength, electrical and thermal properties, electromagnetic interface shielding, proton radiation shielding and neutron attenuation characteristics[192]. Secondary neutrons are difficult to shield against due to their electroneutrality. One of the most considered elements for neutron shielding is the isotope ^{10}B of boron[59]. However, using this in conjunction with the proposed polymer composite would again add to the total weight of the shields. One way to overcome this is using targeted neutron attenuation methods. Using targeted strategies that could reduce the probability of generating secondary neutrons, one would obtain a more weight-efficient way to minimise radiation-induced damage.

In this work, we report on the neutron attenuation characteristics of the ABPBI/MWCNT composites when exposed to proton irradiation. For this, the ABPBI/MWCNT were fabricated at various loading weight percentages (wt. %) and compared to the performance of the pristine ABPBI polymer membrane under the same radiation conditions. Subsequently, the proton irradiation-induced effects on the composites were studied to ascertain the feasibility of using this composite on space missions. These include the thermal stability, composition and structural changes that may have occurred in the composites during irradiation.

6.3   Methods

6.3.1   Fabrication

The polymer membranes used in this work were synthesised as previously described in Chapter 5.2. Again, pristine ABPBI and ABPBI/MWCNT, of 1 and 3 wt. % respectively were fabricated and compared.

6.3.2 Characterisation

The fabricated ABPBI and ABPBI/MWCNT composites were characterised by Fourier-Transform Infra-Red (FTIR) spectroscopy, X-ray Diffraction (XRD) spectroscopy, Thermogravimetric Analysis (TGA), Differential Scanning Calorimetry (DSC) and Scanning Electron Microscopy (SEM).

FT-IR was performed on a Nicolet iS10 FTIR spectrometer (Thermo Fisher) on the pre-and post-irradiation composites in the range 400 - 4000 cm^{-1} with a resolution of 2 cm^{-1}. The resulting spectra for all composites were evaluated and compared, including the assignments of the observed peaks.

XRD was performed on a Scintag DMS2000 diffractometer on the pre-and post-irradiation composites with Cu$K\alpha$1 radiation ($\lambda = 1.54184$ Å) operating at a voltage of 30 kV and a current of 10 mA, in the 2θ-range of 5 - 65°. The spectra obtained were evaluated and compared to identify the characteristic peaks for ABPBI and any changes in these peaks due to the addition of MWCNT and irradiation-induced changes to the ABPBI matrix.

TGA was performed on a Q500 from TA Instruments to determine the composites' weight loss as a function of increasing temperature. The analysis was performed in an inert N$_2$ atmosphere for a temperature range between 25 - 600°C at a ramp rate of 10°C min^{-1}. The results for both pre-and post-irradiation composites were evaluated and compared.

DSC was performed on a Q20 from TA Instruments to measure the change in the composites' heat flow as a function of temperature. The analysis was performed in an inert N$_2$ atmosphere for a temperature range between 25 - 400°C at a ramp rate of 10°C min^{-1}. The pre-and post-irradiation composites used for the analysis had a mass of approximately 10 mg.

SEM was performed on a Zeiss Auriga field emission gun scanning electron microscope (FEG-SEM) operated at an accelerating voltage of 5 kV using an in-lens high-resolution detector to inspect the surface morphology of both the pre-and post-irradiation composites. The composites were compared to determine if any defects were created on the surface of the composites due to the proton bombardment.

6.3.3 Proton radiation tests and secondary neutron monitoring

The composites were tested for their proton shielding effectiveness and secondary neutron generation properties. Before the proton bombardment experiments were conducted, the simulation software, Stopping and Range of Ions in Matter (SRIM)[193] was used to determine the range of the incident proton in the composites for various energies. Table 6.1 provides the range of incident protons as a function of energy obtained from the SRIM calculations. The densities of the composites used in the SRIM calculations can be found in Table 6.2.

TABLE 6.1: SRIM calculations of the range of incident protons in the ABPBI and associated MWCNT-loaded composites.

Sample	Incident Proton Energy (MeV)	Stopping Range (μm)
ABPBI	3	118.83
	5	286.84
	7	518.09
	10	975.98
ABPBI/MWCNT 1 wt. %	3	100.92
	5	243.56
	7	439.84
	10	828.42
ABPBI/MWCNT 3 wt. %	3	98.04
	5	236.58
	7	427.18
	10	804.45

In the LEO environment, proton energy ranges between 0.1 and approximately 200 MeV with a corresponding 11-year integral fluence between 1×10^{12} and 1×10^9 protons/cm^2, respectively[5]. This information, along with the results obtained from SRIM, was used to select the appropriate energy of the incident proton beam and its associated beam current used in the proton radiation experiments to ensure the protons are stopped in the material. The experimental setup is illustrated in Figure 6.1.
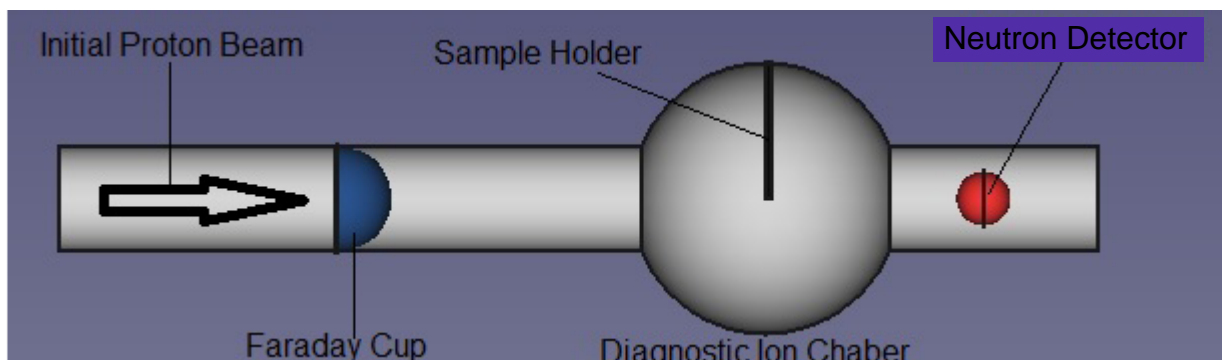
FIGURE 6.1: Simplified schematic of the experimental setup, side view.

The incident proton beam energy was 5 MeV with a proton current of 10 nA and a spot size of 0.82 cm^2. Each composite was exposed to this beam for a total of 1 hour. As such, this correlates to having a fluence of 2.71×10^{14} protons/cm^2. In the LEO environment, the 5 MeV protons have a fluence of approximately 1×10^{11} protons/cm^2, $1000\times$ less than the fluence used in our experiment. The reason for a larger fluence being used in the experiment was to effectively increase the exposure period such that a one-hour exposure would equal approximately forty days (or one month) of total fluence experienced by the composites; this conversion was made in accordance with work done by Liu *et al.*[194].

To monitor the secondary neutrons generated by the composites during the proton irradiation process, a neutron detector (BF$_3$) was placed behind the composites in the beamline. As the beamline components are fabricated from stainless steel, which also produces secondary neutrons when struck by protons, the number of neutrons detected before any samples were placed was also recorded to establish a background reading for the beamline. Once the background reading was recorded, the composites were moved into the beam path to record the secondary neutron generated by each composite.

6.4 Results and Discussion

6.4.1 Proton Permeability of ABPBI.

SRIM simulations were used to determine the stopping range of the protons within the polymer composites as a function of incident proton energy and the thickness of the composites. The results of the simulations are presented in Table 6.1. From this, an incident proton beam energy of 5 MeV was selected to test the proton transmission properties of the composites experimentally. The SRIM companion software, Transport of Ions in Matter (TRIM), was used to simulate the proton range within the ABPBI and the MWCNT-loaded composites. TRIM uses the Kinchin-Pease method to calculate the irradiation damage and depth profiles of the incident radiation on a material[195]. TRIM simulations were successfully used in work by Luz Martines[30] to map the trajectories of protons, of varying energies, in Lead and Aluminium. In the TRIM simulation, an incident proton energy of 5 MeV and an arbitrary composite thickness of 500 μm were used to determine the ion range and damage profile for the ABPBI and MWCNT-loaded composites. The result of the TRIM simulation for all composites is presented in Figure 6.2.
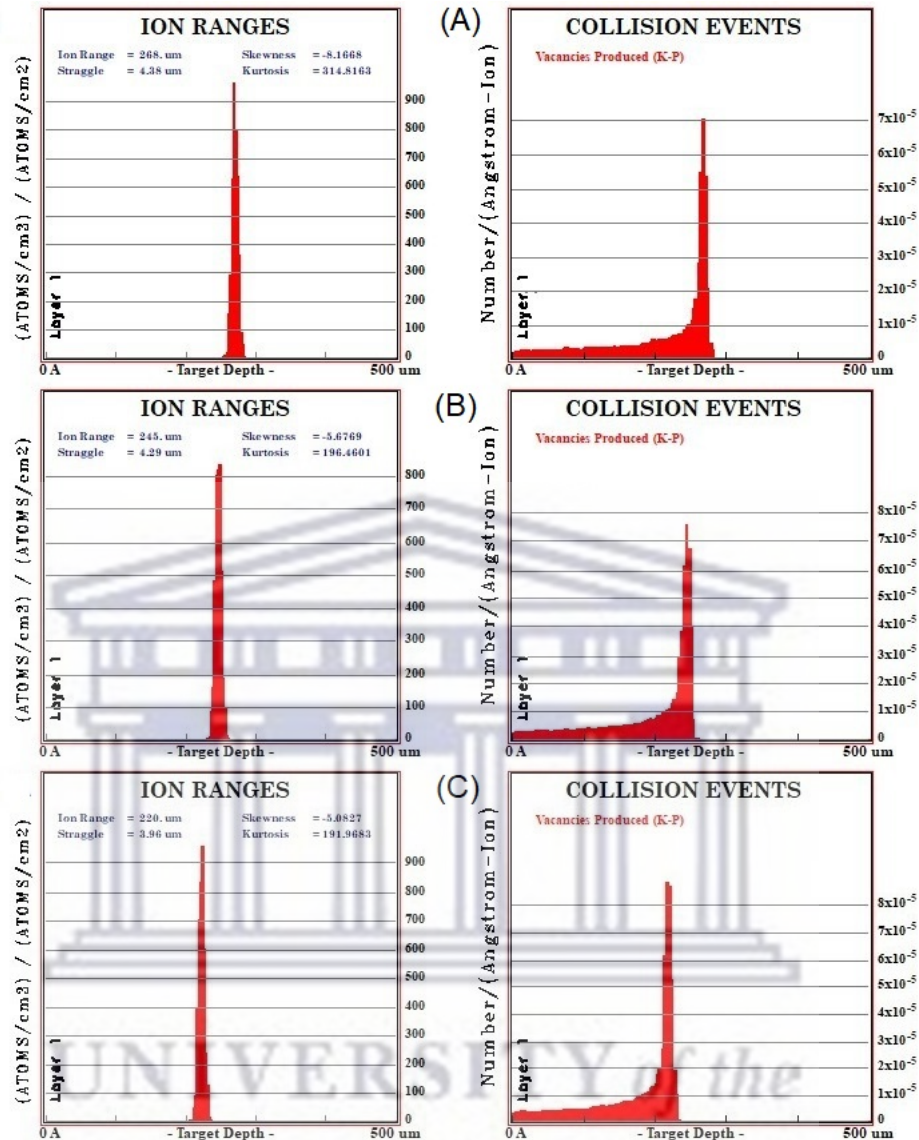
FIGURE 6.2: TRIM simulation results for Ion ranges (left) and Collision events (right) under 5 MeV proton irradiation into pristine ABPBI (A), ABPBI/MWCNT 1 wt. % (B) and ABPBI/MWCNT 3 wt. % (C), respectively.

From the Ion range plot for pristine ABPBI shown in Fig 6.2(A), we see that most of the 5 MeV protons penetrate up to a maximum depth of 268 μm into the ABPBI polymer matrix. The width of the proton distribution peak suggests that the composite is relatively permeable to protons. However, compared to its collision event profile, collisions between the protons and ABPBI matrix occur at lower depths resulting in either a loss of energy by the protons or implantation of the protons at the maximum ion depth in the ABPBI matrix. The collision profile also shows that a relatively large number of collisions occur at the maximum ion depth. TRIM simulations were again run, using the same parameters, for the ABPBI/MWCNT 1 wt. % and ABPBI/MWCNT 3 wt. % composites to compare their depth profiles with that of pristine ABPBI, the results of which are shown in Figs 6.2(B) and 6.2(C), respectively.

When comparing, the ion ranges for the ABPBI/MWCNT 1 wt. % and ABPBI/MWCNT 3 wt. % composites to that of the pristine ABPBI membrane, we observe that an increase in MWCNT loading results in a decrease in proton penetration depth. This lower penetration of protons into the composites is most likely a result increased material density. Consequently, increasing the MWCNT loading would mean that less material (thickness) would be required to shield against these protons, which ultimately reduces the overall weight of the payload. This summation plays an essential role in the cost considerations of the space mission in LEO. The collision events for all three composites showed similar profiles, with very few damage events in the composites recorded before the maximum proton penetration range was reached and nothing after this point. However, the overall number of collision events increases as the MWCNT wt. % load is increased. This increase is attributed to the composites' density increase as the MWCNT load increases. With both the SRIM and TRIM simulations confirming the thickness requirements for the composites, proton irradiation experiments were conducted, with composite specifications listed in Table 6.2, to test the proton transmission and monitor the secondary neutron production of the composites.

TABLE 6.2: Specifications of composites used in the proton irradiation experiments.

Sample	Area (cm^2)	Thickness (μm)	Density (g cm^{-3})
ABPBI	1	280	1.315
ABPBI/MWCNT 1 wt. %	1	330	1.558
ABPBI/MWCNT 3 wt. %	1	320	1.612

6.4.2 Secondary Neutron Generation

The proton irradiation experiments were conducted on the composites as outlined in section 6.3.3. Each composite was exposed to a 5 MeV proton beam with a 10 nA beam current (fluence = 2.14×10^{14} protons/cm^2) for 1 hour for each sample. As stated, a higher fluence was used during the experiments than typical in the LEO environment to increase the effective exposure period; i.e. 1 hour of experimental exposure is equivalent to approximately 40 days of real exposure in the LEO environment. This combination of proton energy and fluence was used to stop protons inside the composites, thus ensuring that any neutrons detected during the experiment came from the composites, not the surrounding beamline components. During the proton irradiation experiments, a neutron detector (BF$_3$) was placed behind the samples to measure the secondary neutrons generated by the composites during the irradiation process. In principle, a good shielding material should not only be able to attenuate the secondary neutrons produced by the metallic components of the payload but should have a minimal generation of secondary neutrons[192]. As such, a secondary neutron generation baseline for the

beamline's metallic components was established by taking an initial neutron reading before the samples were moved into the path of the proton beam. Here, the baseline reading serves as an analogue for the secondary neutron generated by the metallic components of the spacecraft. This baseline value, hereafter referred to as background, is used to assess the effectiveness of the composites at attenuating neutrons, as the neutron reading obtained from the composites, after moving them into the path of the beam, should at least be less than that of the background value. This, in essence, attempts to replicate an instance in which the components of the spacecraft are shielded from proton irradiation by the composites. After recording the background reading, each composite was exposed to the proton beam for 1 hour. A reading of the secondary neutrons generated by the composites was recorded over 5-minute intervals. A comparison of the average secondary neutrons generated over the 1 hour is presented in Fig 6.3.
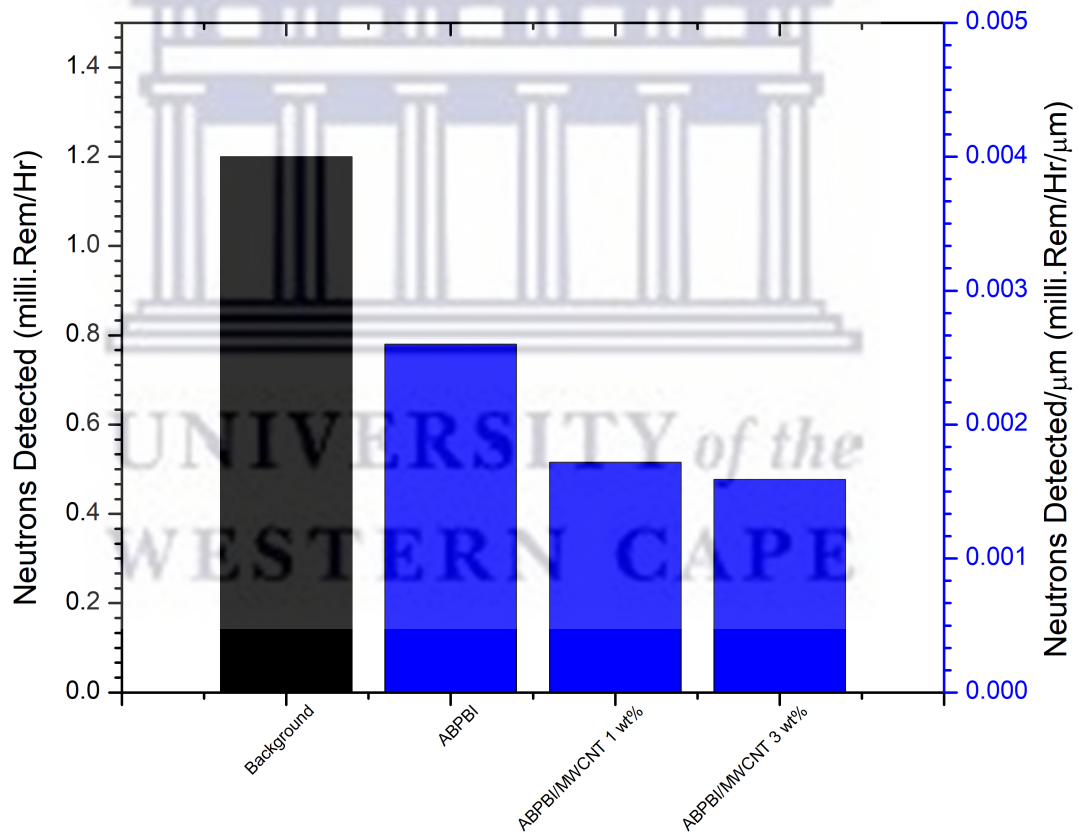
FIGURE 6.3: Neutrons detected per micrometer of film for ABPBI and MWCNT-loaded composites for a 1-hour exposure to a 5 MeV proton beam.

The composites' effectiveness in attenuating secondary neutrons is quantified by the number of secondary neutrons detected for each composite and compared to the background measurement. As shown in Figure 6.3, significantly fewer neutrons are detected for the composites compared to the background reading. Furthermore, the number of secondary neutrons detected decrease as the MWCNT load increases. Based on this,

the addition of MWCNTs to the ABPBI matrix either improves the neutron attenuation ability of the ABPBI, reduces the secondary neutron generation of the polymer matrix, or enhances both the neutron attenuation and the reduction of secondary neutrons in the nanocomposite materials. In both ways, adding MWCNTs to the polymer matrix presented a positive performance regarding neutron shielding.

6.4.3   ABPBI Composite Properties and Radiation-Induced Effects

6.4.3.1   Scanning Electron Microscopy

To ascertain the damage the proton irradiation has on the polymer composites, scanning electron microscopy (SEM) was used to probe the surface morphology of the composites. SEM was performed on both pre-and post-irradiated composites to study any changes to the surface morphology of the composites induced by proton irradiation. The results of this analysis are presented in Fig 6.4, which shows the surface morphology comparison for both pre-and post-irradiation.

From Figs 6.4 (A and C), we observe the pristine ABPBI (A) and the ABPBI/MWCNT 1 wt. % (C) exhibits a relatively smooth and compact surface with no discernible surface defects visible in the images. In comparison, the pre-irradiation ABPBI/MWCNT 3 wt. % composite exhibits an increase in roughness at this MWCNT load, with indentations and valleys visible in the image. Moreover, at this MWCNT load, the composites appear to display a decrease in homogeneity, evident in the polymer clusters scattered throughout the surface of the composite.

The post-irradiation pristine ABPBI membrane, Figure 6.4 (B), shows a drastically different surface topography to that seen in the pre-irradiation membrane. Visible damage from proton irradiation can be seen in the SEM image for this composite, with the formation of pothole defects at the site of the beam spot. These pothole defects vary between 1 and 10 μm in diameter. Also visible in the image was a noticeable increase in surface roughness at the site of the beam spot leading one to speculate that the proton beam has an etching effect on the membrane.

In contrast, when comparing the irradiated ABPBI/MWCNT 1 wt. % and ABPBI/MWCNT 3 wt. % composites in Figure 6.4 (D and F respectively) to their non-irradiated counterparts, no visible pothole defects formed on the surface of the composites. This suggests that MWCNT loading of the polymer increases its radiation damage resistance concerning defect formation. However, proton irradiation of the MWCNT-loaded composites affected the surface topography of the composites. This was determined by the visible increase in roughness seen for the post-irradiation composites.
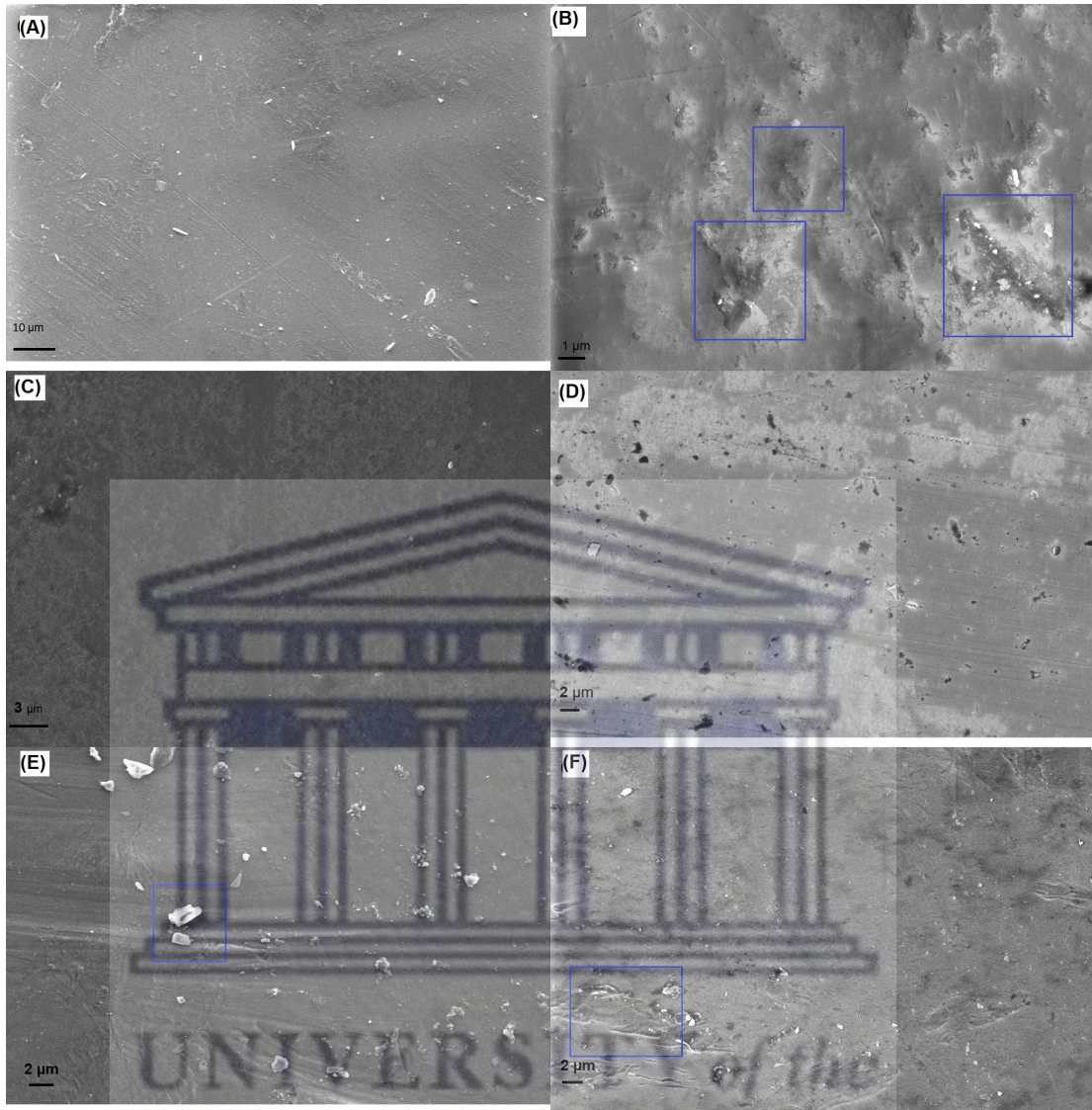
FIGURE 6.4: SEM images for the pre-and post-irradiated composites. ABPBI pre-irradiation (A), ABPBI post-irradiation (B), ABPBI/MWCNT 1 wt. % pre-irradiation (C), ABPBI/MWCNT 1 wt. % post-irradiation (D), ABPBI/MWCNT 3 wt. % pre-irradiation (E) and ABPBI/MWCNT 3 wt. % post-irradiation (F).

Overall, less proton radiation-induced damage was observed by adding MWCNT to the ABPBI polymer matrix.

6.4.3.2 Thermogravimetric Analysis

TGA was performed before and after proton irradiation to ascertain the effects of proton irradiation on the thermal stability of the composites. The TGA analysis was again performed in a N_2 atmosphere between room temperature to 600°C, presented in Figure 6.5.

FIGURE 6.5: TGA plots of ABPBI and irradiated ABPBI (a), ABPBI/MWCNT 1 wt. % and irradiated ABPBI/MWCNT 1 wt. % (b) and ABPBI/MWCNT 3 wt. % and irradiated ABPBI/MWCNT 3 wt. % (c) composites. The TGA curves for all irradiated composites are compared in (d).

From the TGA curves for the pristine ABPBI membranes, Figure 6.5 (a) shows a significant decrease in the irradiated membrane's thermal stability compared to the non-irradiated membrane. While the profiles of the thermal degradation curves are similar, the irradiated sample degrades at a higher rate than observed in the non-irradiated sample. Comparing the $T_{d5\%}$, weight loss of approximately 5%, and $T_{d10\%}$, weight loss of approximately 10%, for the composites, we find that $T_{d5\%}$ occurs at 129.19°C for the pre-irradiated membrane and 115.69°C for the post-irradiated membrane. Similarly, $T_{d10\%}$ occurs at 245.96°C for the pre-irradiated membrane and 214.35°C for the post-irradiated membrane. These evaluations show that the pristine ABPBI membrane is less radiation-resistant concerning its thermal stability.

Conversely, the MWCNT-loaded composites, Fig 6.5 (b and c), presented a better radiation resistance concerning thermal stability maintenance. The ABPBI/MWCNT 1 wt. % and the ABPBI/MWCNT 3 wt. % composites showed better thermal stability in the irradiated composites than in their non-irradiated counterparts. For the ABPBI/MWCNT 1 wt. % composites, the TGA curves presented an almost identical degradation rate for the irradiated and non-irradiated membranes up to 165°C. After

which, the irradiated ABPBI/MWCNT 1 wt. % membrane showed improved thermal stability of around 2%. Similarly, an improvement was observed in the irradiated ABPBI/MWCNT 3 wt. % composite. In the non-irradiated ABPBI/MWCNT 3 wt. %membrane, $T_{d10\%}$ occurred at 201.13°C, while at this same temperature, the irradiated ABPBI/MWCNT 3 wt. % membrane only showed a weight loss of 8.5% . Overall, the irradiated ABPBI/MWCNT 3 wt. % composite showed improved thermal stability of around 3% . Furthermore, when comparing the thermal stability of all the irradiated composites, Figure 6.5 (d), we observe that the MWCNT load composites present an improved thermal resistance than that of the pristine ABPBI membrane. The irradiated ABPBI/MWCNT 1 wt. % and ABPBI/MWCNT 3 wt. % composites presented a very similar degradation rate for temperatures above 325°C, while below this, the ABPBI/MWCNT 3 wt. % composite showed better thermal stability.

6.4.3.3   Differential Scanning Calorimetry

DSC was used to investigate the changes to the thermal properties post-irradiation to ascertain how heat flow changes in the composites. The DSC plots for this analysis are presented in Fig 6.6.

As previously mentioned in the DSC study on the pre-irradiation composites, the temperature range was not sufficiently high enough to identify the glass-transition and decomposition temperatures for the ABPBI composites; however, the temperature range still provides insightful information on the heat-flow characteristics as it relates to the LEO environment. Interestingly, we observe a significant decrease in heat flow for the irradiated composites compared to the pre-irradiated composites. This is believed to result from the proton beam weakening the bonds in the underlying polymer matrix[109]. Consequently, during the ramping phase of the DSC process, substantial cross-linking occurs in the composites leading to the more prominent endothermic peaks observed for the irradiated composites[178]. Surprisingly, the irradiated ABPBI/MWCNT 1 wt. % composite showed the lowest decrease in heat flow compared to other irradiated composites. Figure 6.6 (d) shows the irradiated pristine ABPBI and ABPBI/MWCNT 3 wt. % showed almost identical heat flow patterns. This would suggest that the ABPBI/MWCNT 1 wt. % composite, post-irradiation, becomes less susceptible to increases in temperature as it maintains a relatively constant heat flow profile. This is supported by the TGA results obtained for the post-irradiation composites in which we saw that between room temperature and 400°C, this composite became more thermally stable.
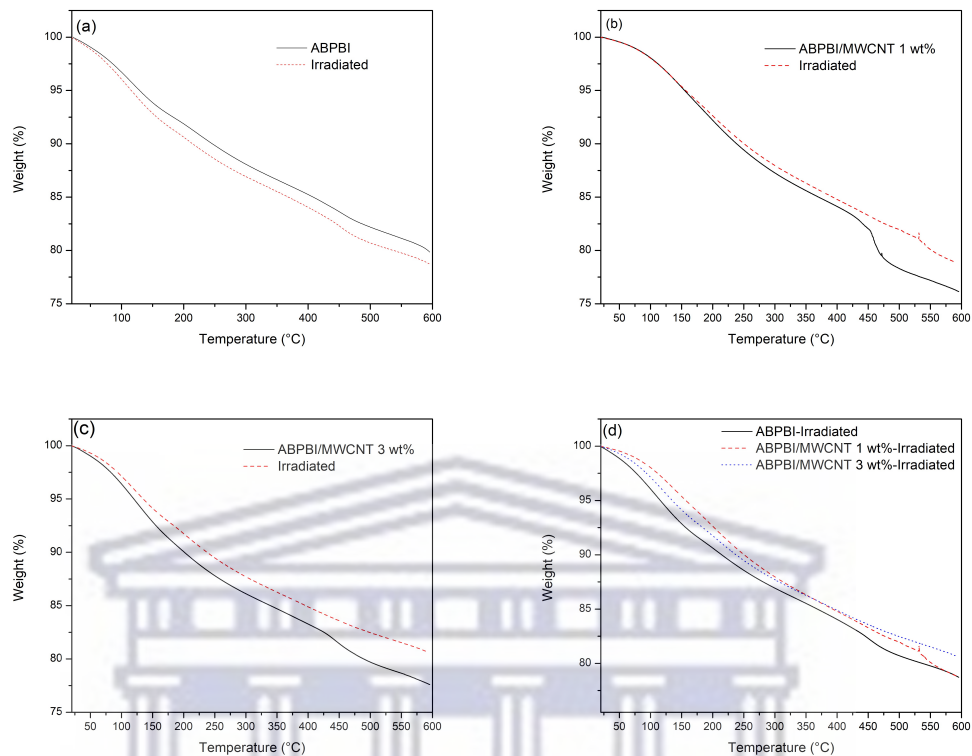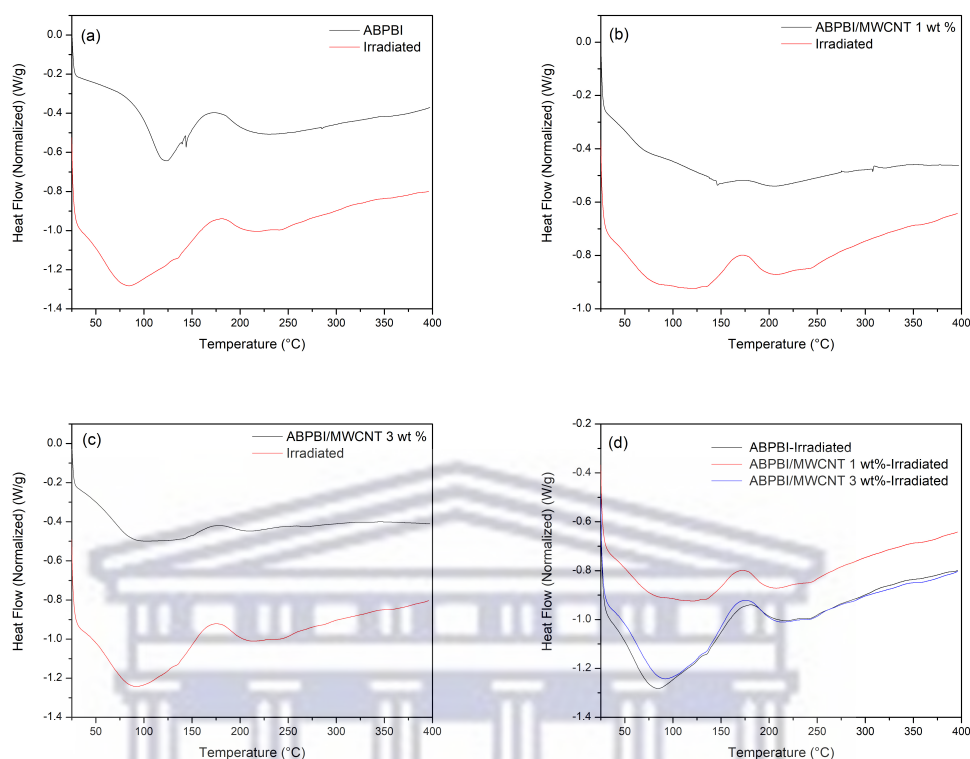
FIGURE 6.6: DSC plots of ABPBI and irradiated ABPBI (a), ABPBI/MWCNT 1 wt. % and irradiated ABPBI/MWCNT 1 wt. % (b) and ABPBI/MWCNT 3 wt. % and irradiated ABPBI/MWCNT 3 wt. % (c) composites. The DSC curves for all irradiated composites are compared in (d). Exothermic heat flow in the positive y-direction (EXO UP).

6.4.3.4 Radiation-Induced Effects

In the following section, the ABPBI/MWCNT 1 wt. % membrane was used to study the effects of proton irradiation on the composition and structure of the composite. This was done to compare and identify any compositional and structural changes that occur in the composite during the irradiation process. Four membranes of the same nanocomposite were used in this section. These include; an un-irradiated sample (Pre-irradiation) that acts as the control, a sample exposed to a 5 MeV proton beam for 20 minutes, a sample exposed to a 5 MeV proton beam for 3 hours and a sample exposed to an 8 MeV proton beam for 5 minutes.

FTIR spectroscopy was performed to ascertain the effects of proton radiation exposure time and energy have on the composites' molecular composition (see Figure 6.7). Two of the composites used in this section of the study were exposed to a 5 MeV proton beam for varying time intervals to ascertain the effects of exposure times on the composites. The third was exposed to an 8 MeV proton beam to determine the impact of energy on the composites. It is also important to note that at 8 MeV, given the thickness of

the composite was only 340 μm; protons were passing through the composite as the stopping range for this energy is around 500 μm. This implies that the incident proton beam affects this composite over a larger volume than the composites exposed to lower energies.
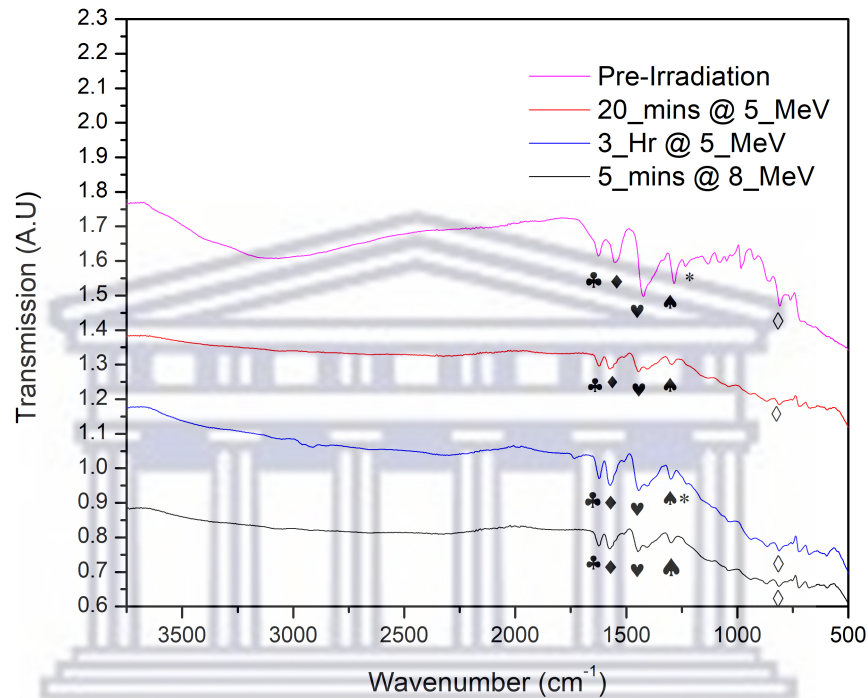
FIGURE 6.7: Comparison of FTIR spectra for ABPBI/MWCNT 1 wt. % composites at longer exposure times and higher proton beam energies.

The first key difference observed in the FTIR spectra between the pre-and post-irradiated samples was the O—H stretching band reduction due to absorbed water between 3666 and 2500 cm^{-1}. This suggests that either the loosely bound water in the composites was removed during the irradiation process as the sample is heated or irradiation causes a reduction in the hygroscopic nature of the composites, i.e. the composite losses its propensity to absorb water after exposure to proton irradiation.

Furthermore, although the characteristic backbone of the ABPBI composite is still present in the spectra, denoted by the peak identifiers (symbols) in Figure 6.7, in the post-irradiated composites, these peaks present at a relatively lower intensity than that of the pre-irradiated samples. This is believed to result from radiation-induced damage to the composites during the proton irradiation process causing a reduction in the functional group associated with each characteristic peak. However, since the characteristic backbone of the post-irradiated composites is still present, it is evident that the polymer maintained its chemical composition integrity. This suggests that the composites could

perform their radiation shielding functions for longer durations and at higher energies. Moreover, when comparing the post-irradiated composites, the composites exposed to the proton irradiation for 3 hours at 5 MeV showed an almost identical spectrum to that of the composite exposed for 5 minutes at 8 MeV, which shows that the compositional integrity of the composites is maintained even at higher radiation energies. Table 6.3 provides an overview of the peak identifiers and their assignments in Figure 6.7 [178, 183].

TABLE 6.3: FTIR Peak Assignments for pre- and post-irradiated ABPBI/MWCNT 1 wt. % composites, based on Figure 6.7.

Peak Identifier	Peak Assignment
♣	C=C/C=N stretching.
♦	Ring vibration due to conjugation between benzene and imidazole rings.
♡	In-plane deformation of benzimidazole rings.
♠	In-plane C-H deformation.
∗	Breathing mode of the imidazole rings.
◇	Out-of-plane C-H bending of the benzene rings.

This study aims to characterise the effects of proton irradiation on the structure of the composites compared to the pre-irradiated composite. Similar to the FTIR study, the XRD patterns for pre-and post-irradiated ABPBI/MWCNT 1 wt. % composites are presented in Figure 6.8.

All four composites presented two characteristic peaks in their respective spectra. The first is attributed to an increase in crystallinity or ordering in the composites, and the second is to stacking of ABPBI chains. However, relatively large shifts in the 2θ value, around $2\theta = 10°$, are observed for the first peak in the post-irradiation composites. This peak shifts to around $2\theta = 18°$ across all post-irradiated composites, irrespective of exposure time or proton beam energy. The reduction in d-spacing, from 8.53 to around 4.73 Å, observed for these peaks are believed to be a consequence of the proton irradiation introducing defects in the polymer matrix that affects the crystallisation tendency of the polymer. Proton irradiation is known for causing such defects in materials during the irradiation process[196]. It is yet unclear how this small change to the semi-crystalline structure of the composites will effect the lifetime of the material however, based on their aforementioned proton shielding and secondary neutron attenuation performances, I believe this change to be negligible concerning their radiation shielding functions.

Conversely, the second peak, around $2\theta = 26°$, in all pre-and post-irradiated composites remains relatively unaffected, with minimal change in the 2θ values and lattice spacing observed for this set of peaks. Since this set of peaks is attributed to the stacking of ABPBI chains in the polymer matrix, it can be deduced that the proton irradiation does

not affect the underlying structural composition of the composites. The analysis of the XRD patterns in Figure 6.8 is presented in Table 6.4.
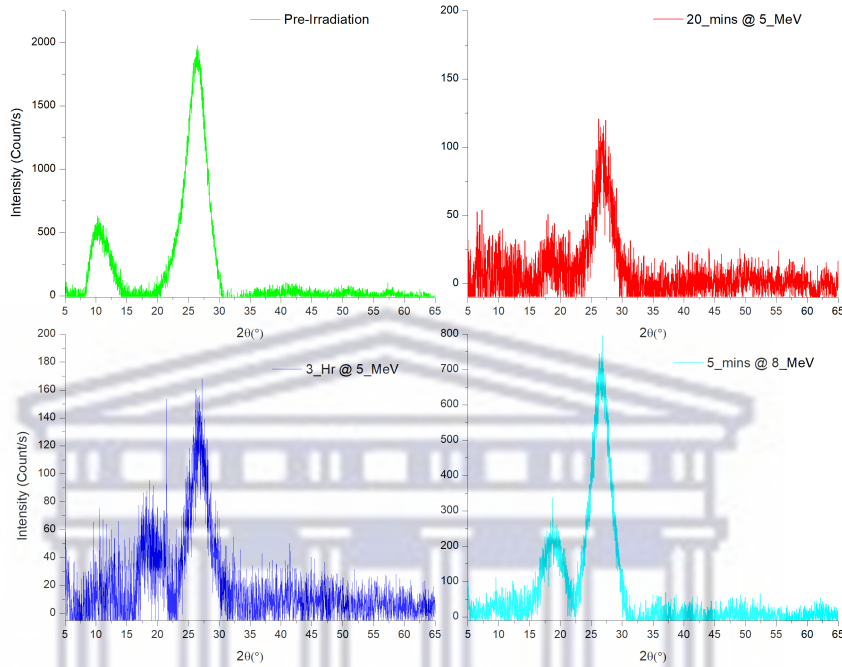
FIGURE 6.8: Comparison of XRD patterns for ABPBI/MWCNT 1 wt. % composites at longer exposure times and higher proton beam energies.

TABLE 6.4: XRD analysis for pre- and post-irradiated ABPBI/MWCNT 1 wt. % composites.

	1st Peak in Sample			2nd Peak in Sample		
Sample	2θ (°)	d-spacing (Å)	FWHM (°)	2θ (°)	d-spacing (Å)	FWHM (°)
Pre-Irradiation	10.37	8.53	4.12	26.42	3.37	3.44
20 mins @ 5 MeV	18.77	4.73	3.75	26.88	3.32	3.47
3 Hours @ 5 MeV	18.71	4.74	3.91	26.76	3.33	3.81
5 mins @ 8 MeV	18.73	4.74	3.81	26.63	3.35	4.24

For further analysis of the XRD patterns concerning crystallite sizes and strain, the Williamson-Hall method, outlined in section 5.4.2, was again employed. The Williamson-Hall analysis for pre-and post-irradiated ABPBI/MWCNT 1 wt. % composites are presented in Table 6.5.

TABLE 6.5: Crystallite size and strain for pre- and post-irradiated ABPBI/MWCNT 1 wt. % composites.

Sample	L (nm)	ε
Pre-Irradiation	2.62	0.01928
20 mins @ 5 MeV	2.57	0.01428
3 Hours @ 5 MeV	2.17	0.00329
5 mins @ 8 MeV	2.68	0.02386

From the crystallite size data obtained using the Williamson-Hall method, we observe a trend in which the crystallite size decreases for more prolonged exposures of the composite to the proton beam with an energy of 5 MeV. The composite exposed to the 8 MeV proton beam shows an increase in crystallite size, becoming more significant than the pre-irradiated composite. This is further evidence of the broadening observed in the spectra due to an increased strain on the composites. Following a similar trend to the crystallite sizes, the calculated strain values decrease with an increased exposure time while increasing when the beam energy is increased. As per Dixit *et al.*[197], we deduce that the proton irradiation reduces the intrinsic strain in the composites as the exposure time increases, most likely due to an increase in ordering throughout the composites. The increase in ordering consequently decreases the crystallite size resulting in the trend observed across the 5 MeV proton beam irradiated composites. We attributed he increase in intrinsic strain observed for the composite exposed to the 8 MeV proton beam to the composite radiation-induced degradation. At this energy and fluence, during the irradiation process, the composites are heated by the incident proton beam resulting in an expansion of the ABPBI polymer matrix, as outlined in work by Takenaka *et al.* on the thermal expansion of various matrix composites [198]. This expansion is believed to cause the crystallite sizes and the intrinsic stress of the composite to increase. As previously mentioned, at 8 MeV, protons were passing through the composite. This means the incident proton beam induced heating over a larger volume of the composite in comparison with the composites exposed to lower energies. Knowing this, given that the intrinsic strain and crystallite size values are comparable to that of the pre-irradiated composite, we deduce that the beam had little impact on the underlying structure of the ABPBI matrix.

6.5 Conclusion

This work tests the ABPBI polymer composite loaded with MWCNT for its radiation shielding capabilities. Proton irradiation experiments were conducted on the composites to ascertain their secondary neutron attenuation capabilities and to study the effects of proton irradiation on the material's properties. The analysis of the results from this section showed that proton irradiation had almost no impact on the composition of the nanocomposites. The proton irradiation increased ordering in the nanocomposites, decreasing the composite's crystallite sizes and intrinsic strains. The MWCNT-loaded nanocomposites also proved to be more resistant to radiation-induced damage. The thermal analysis showed that proton irradiation enhanced the thermal stability of the composites, which improved with an increase in MWCNT load. From the secondary neutron generation study, we observed that the MWCNT-loaded composites showed a significantly reduced secondary neutron generation rate, an improved neutron attenuation capability, or both. This functionality improved as the MWCNT load in the ABPBI matrix was increased.

Given the outcomes mentioned above in our experiments, this work will pave the way for applying ABPBI/MWCNT nanocomposites as an effective proton shielding material on missions to the LEO region of space.

Chapter 7

Conclusion/Summary of Findings

Aluminium (Al) has been considered the most effective radiation shielding material currently in use in the space industry for the longest time. However, Al, and its associated metallic alloys, suffer greatly from issues related to weight and secondary radiation generation from their interactions with ionising radiation. Both issues add to the overall cost of the mission. Moreover, secondary radiation directly threatens the crew's lives and the payload aboard the spacecraft. This led to exploring of other materials that could be used in space radiation applications that would mitigate the risk posed by secondary radiation generation. Insufficient shielding effectiveness, low function-to-weight ratios, high costs, and difficulties with large scale fabrication and maintenance limit other materials from currently being used in space applications. This led to the review of other nano-technologies to overcome some of these shortcomings highlighted by the previous generation of shielding materials. Among these, polymer-based nanocomposites possess particularly desirable material properties for space applications. Polymer-based nanocomposites also offer the ability to modify the material's properties by introducing different nano-filler materials into the matrix of the underlying polymer. Carbon nanotubes (CNTs) were quickly targeted as the nano-filler material for consideration in space applications due to their superior and comprehensive material properties. It was believed and later shown that using CNTs in fabricating polymer nanocomposites would significantly increase the radiation shielding effectiveness of said polymer.

Furthermore, it was suggested by Liu *et al.*[194] that using CNTs with multiple walls would significantly increase the radiation-induced damage resistance on the nanocomposites. Subsequently, this advocated using multi-walled carbon nanotubes (MWCNT) over their single-walled (SWCNT) counterparts. The MWCNTs offer a unique balance between mechanical and thermal properties with high resistance to chemical erosion, making it a suitable candidate for nanocomposite fabrication.

94

This work explores using a polymer nanocomposite for space radiation shielding applications in the low earth orbit (LEO) environment. The polymer used for this investigation was poly(2, 5)benzimidazole (ABPBI), the simplest member of the polybenzimidazole (PBI) family. ABPBI was selected for its inherently high material properties, hydrogen content, and low weight characteristics. Moreover, the fabrication of high quality membranes of ABPBI is easily achieved in a significantly more inexpensive manner than other aromatic polymers. To form a nanocomposite from the ABPBI polymer, MWCNTs were introduced into the polymer matrix at different weight percentages (wt. %) loads, to create the ABPBI/MWCNT 1 wt. % and ABPBI/MWCNT 3 wt. % nanocomposites, respectively. The ABPBI and ABPBI/MWCNT nanocomposite membranes used in this work were fabricated using an immersion precipitation membrane casting method. An *in-situ* introduction of the MWCNTs was used to fabricate the ABPBI/MWCNT nanocomposites.

Before work commenced on the fabrication and characterisation of the ABPBI and ABPBI/MWCNT nanocomposites, a computational investigation was conducted. This investigation was to ascertain the feasibility of using the plasma-enhanced chemical vapour deposition (PECVD), at the University of the Western Cape to produce the required MWCNT nano-filler material used later in this work. A 2-d axisymmetric fluid model is presented that solves the continuity equations for charged species and electron energy using the COMSOL multiphysics software. From this work, we determined the exact deposition parameters required for the growth of MWCNTs in the PECVD system. A notable finding of this investigation was the ability to determine the growth rate, in nm/s, for carbon-based materials in the system. With this, you can control the length of the MWCNTs, as this length plays a vital role in the overall properties of the MWCNT itself.

As part of the first investigation relating to the nanocomposite materials, the effects of the addition of MWCNT into ABPBI on the underlying polymer matrix was determined. Two nanocomposite membranes, ABPBI/MWCNT 1 wt. % and ABPBI/MWCNT 3 wt. % were fabricated, characterised, and their properties were compared to pristine ABPBI. First, it was determined that the addition of MWCNT made the nanocomposites less hygroscopic than the pristine ABPBI membrane, evident from the reduction in the intensity of the absorbed water band in their respective FTIR spectra. Also, the composition of the underlying ABPBI polymer matrix remained unaffected by the addition of MWCNT, as the characteristic molecular fingerprint of the ABPBI matrix was observed across all the composites. When comparing the structures of the pristine ABPBI and the MWCNT-loaded composites, we found that adding MWCNTs increased the intrinsic strain within the nanocomposites. This strain increased with an increased MWCNT load. Fortunately, the rest of the structure of the nanocomposites remained

relatively unchanged. Next, the thermal stability of the pristine ABPBI and its associated nanocomposites were evaluated and compared. From this, we could determine that adding MWCNTs improved the thermal properties of the ABPBI matrix; this increase was proportional to the MWCNT load in the nanocomposite. Lastly, we demonstrated that adding MWCNTs to the ABPBI polymer matrix, even in small quantities, significantly improves the mechanical properties of the polymer. Having shown that the ABPBI polymer matrix responds favourably to the addition of MWCNT, we moved on to test the proton radiation shielding effectiveness of the composites.

To test the proton radiation shielding effectiveness of the nanocomposites, pristine ABPBI and its associated MWCNT-loaded nanocomposites of optimised thickness were exposed to a 5 MeV proton beam (fluence = 2.71×10^{14} protons/cm^2) for one hour. The selection of proton energy and corresponding fluence was made in accordance with measured values from the LEO environment. During the irradiation of each polymer sample, the secondary neutron generation by the composites is recorded and compared to a baseline reading generated by the beamline and each other. Following irradiation, all irradiated polymer composites were characterised and compared to their non-irradiated counterparts to ascertain the effects proton radiation has on the nanocomposites. These experiments showed that the generated secondary neutrons decreased significantly with increased MWCNT load in the ABPBI polymer matrix.

Furthermore, proton irradiation was found not to affect the composition of the pristine ABPBI or the MWCNT-loaded nanocomposites. However, it was determined that proton irradiation induced ordering in the composites, decreasing their intrinsic strain. The MWCNT-loaded nanocomposites also proved more resistant to radiation-induced damage than their unloaded counterpart. Lastly, the thermal stability of the post-irradiation composites was determined and compared to their pre-irradiation counterparts. Interestingly, the thermal stability of the polymer composites increased post-irradiation.

As far as the authors know, ABPBI and, more specifically, ABPBI/MWCNT nanocomposites have yet to be tested for proton radiation shielding applications. Therefore, the authors believe that the overall characteristics of the ABPBI/MWCNT nanocomposite presented in this thesis make it a promising shielding candidate in the LEO environment and advocate for its use in the space industry.

7.1 Future Work

Before the ABPBI/MWCNT nanocomposites can be used in radiation shielding applications in the LEO environment, the nanocomposites must be tested for the resistance to atomic-oxygen (AO). Around 80 % of the radiation mixture in LEO is AO. Moreover, AO is known for its corrosive effects on polymer material due to the production of carbon-oxygen groups. As such, the ABPBI/MWCNT nanocomposites have to be exposed to AO irradiation to quantify their resistance to AO erosion.

The ABPBI/MWCNT nanocomposites should also be tested for high proton energy radiation shielding applications in the outer space environment. These tests would require thickness optimisations of the ABPBI/MWCNT nanocomposites to be completed to ensure the maximum function-to-weight ratio is obtained.

Bibliography

[1] Alberto Stabile. *Design methodologies for radiation-hardened memories in CMOS technology*. PhD thesis, 01 2010.

[2] Gautam D Badhwar. The radiation environment in low-earth orbit. *Radiation research*, 148(5s):S3–S10, 1997.

[3] Mara Johnson-Groh. Studying the van allen belts 60 years after americas first spacecraft. *NASA. gov*, 31, 2018.

[4] Robert J Walters, Scott Messenger, Jeffrey H Warner, Cory D Cress, Maria Gonzalez, and Serguei Maximenko. Modeling of radiation induced defects in space solar cells. In *Physics and Simulation of Optoelectronic Devices XIX*, volume 7933, pages 129–149. SPIE, 2011.

[5] Christophe Inguimbert and Scott Messenger. Equivalent displacement damage dose for on-orbit space applications. *IEEE Transactions on Nuclear Science*, 59 (6):3117–3125, 2012.

[6] Siyuan Chen. Polymer based nanocomposites as multifunctional structure for space radiation shielding: A study of nanomaterial fabrications and evaluations, 2018.

[7] JE Turner. *Atoms, Radiation, and Radiation Protection. Willey*. VCH Verlag GmbH & Co. KGaA Weinheim, Germany:, 2007.

[8] James C Williams and Edgar A Starke Jr. Progress in structural materials for aerospace systems. *Acta materialia*, 51(19):5775–5799, 2003.

[9] Rosalin Rath, Piyush Kumar, Lakshmi Unnikrishnan, Smita Mohanty, and Sanjay K Nayak. Current scenario of poly (2, 5-benzimidazole)(abpbi) as prospective pem for application in ht-pemfc. *Polymer Reviews*, 60(2):267–317, 2020.

[10] Atif Makhdoom. *Low Temperature Processing Route of Silicon Nanoparticle Layers for Solar Cell Application*. PhD thesis, Friedrich-Alexander-Universität Erlangen-Nürnberg (FAU), 2018.

[11] Differential scanning calorimetry, 2019. URL https://pslc.ws/macrog/dsc.htm.

[12] Experimental method and testing procedures laboratory 10: Thermogravimetric analysis, 2022. URL https://sites.google.com/a/iastate.edu/laboratory-10-thermogravimetric-analysis/experimental-methods.

[13] Yang Chen, Michael F Morris, Borna Obradovic, D Li, Al F Tasch, and JS Swinnea. The impact of crystal cut error on the measured impurity profiles resulting from ion implantation. *IEEE Transactions on Semiconductor Manufacturing*, 13 (2):243–248, 2000.

[14] Scanning electron microscopy, 2022. URL https://www.nanoscience.com/techniques/scanning-electron-microscopy/.

[15] Astm, 2015. URL https://compass.astm.org/EDIT/html_annot.cgi?D638+14.

[16] C Yang, ME Navarro, B Zhao, G Leng, G Xu, L Wang, Y Jin, and Y Ding. Thermal conductivity enhancement of recycled high density polyethylene as a storage media for latent heat thermal energy storage. *Solar Energy Materials and Solar Cells*, 152:103–110, 2016.

[17] AZO. Poly(2, 5)benzimidazole material properties, 2003. URL https://www.azom.com/article.aspx?ArticleID=1866.

[18] The LXCat team. Plasma data exchange project. URL https://nl.lxcat.net/data/set_type.php.

[19] Francis A Cucinotta, Myung-Hee Y Kim, and Lei Ren. Evaluating shielding effectiveness for reducing space radiation cancer risks. *Radiation Measurements*, 41 (9-10):1173–1185, 2006.

[20] Space Studies Board. Report. radiation hazards to crews of interplanetary missions: biological issues and research strategies. national research council, 1996.

[21] John W Wilson, Brooke M Anderson, Francis A Cucinotta, J Ware, and Cary J Zeitlin. Spacesuit radiation shield design methods. *SAE Transactions*, pages 277–293, 2006.

[22] Shruti Nambiar and John TW Yeow. Polymer-composite materials for radiation protection. *ACS applied materials & interfaces*, 4(11):5717–5726, 2012.

[23] Jeffery C Chancellor, Graham BI Scott, and Jeffrey P Sutton. Space radiation: the number one risk to astronaut health beyond low earth orbit. *Life*, 4(3):491–510, 2014.

[24] Eric R Benton and EV Benton. Space radiation dosimetry in low-earth orbit and beyond. *Nuclear Instruments and Methods in Physics Research Section B: Beam Interactions with Materials and Atoms*, 184(1-2):255–294, 2001.

[25] L Heilbronn, T Nakamura, Y Iwata, T Kurosawa, H Iwase, and LW Townsend. Overview of secondary neutron production relevant to shielding in space. *Radiation protection dosimetry*, 116(1-4):140–143, 2005.

[26] Z Li, S Nambiar, W Zheng, and JTW Yeow. Pdms/single-walled carbon nanotube composite for proton radiation shielding in space applications. *Materials Letters*, 108:79–83, 2013.

[27] Perry Sprawls. Physical principles of medical imaging. madison, wis. *Medical Physics Pub*, 1995.

[28] Marco Durante. Space radiation protection: destination mars. *Life sciences in space research*, 1:2–9, 2014.

[29] Francis A Cucinotta, Myung-Hee Y Kim, and Lori J Chappell. Evaluating shielding approaches to reduce space radiation cancer risks. *NASA Technical Memorandum*, 217361, 2012.

[30] Luz S Maria Martines. Analysis of leo radiation environment and its effects on spacecraft's critical electronic devices, 2011.

[31] Jane Reifert. Selling space: Accepting the risk. In *AIAA SPACE 2009 Conference & Exposition*, page 6702, 2009.

[32] JH Adams Jr, DH Hathaway, RN Grugel, JW Watts, TA Parnell, JC Gregory, and RM Winglee. Revolutionary concepts of radiation shielding for human exploration of space. Technical report, 2005.

[33] Jared Bell, Dustin Lail, Chris Martin, and Paul Nguyen. Radiation shielding for a lunar base. *National Aeronautics and Space Adiminstration*, 2011.

[34] AB Groh, KK amd Bruce. Nasa glen research center's materials international space station experiment (misse 1-7): Nasa. Technical report, TM-2008-2154821-39, 2008.

[35] LaNetra M Clayton, Timofey G Gerasimov, Martin Cinke, M Meyyappan, and Julie P Harmon. Dispersion of single-walled carbon nanotubes in a non-polar polymer, poly (4-methyl-1-pentene). *Journal of nanoscience and nanotechnology*, 6(8):2520–2524, 2006.

[36] Raj K Kaul, Abdulnasser Fakhri Barghouty, Benjamin G Penn, and Anthony Bruce Hulcher. Multi-functional layered structure having structural and radiation shielding attributes. 2010.

[37] Radiation Effects. Shielding requirements in human missions to the moon and mars, d. rapp. *Mars*, 2:46–71, 2006.

[38] Xindi Li, David Warden, and Yildiz Bayazitoglu. Analysis to evaluate multilayer shielding of galactic cosmic rays. *Journal of Thermophysics and Heat Transfer*, 32 (2):525–531, 2018.

[39] James R Gaier, Wendie C Hardebeck, Jennifer R Terry Bunch, Michelle L Davidson, and Dwight B Beery. Effect of intercalation in graphite epoxy composites on the shielding of high energy radiation. *Journal of materials research*, 13(8): 2297–2301, 1998.

[40] PA Muisener, L Clayton, J DAngelo, JP Harmon, AK Sikder, A Kumar, AM Cassell, and M Meyyappan. Effects of gamma radiation on poly (methyl methacrylate)/single-wall nanotube composites. *Journal of materials research*, 17 (10):2507–2513, 2002.

[41] Jing Liu, Asif Rasheed, Marilyn L Minus, and Satish Kumar. Processing and properties of carbon nanotube/poly (methyl methacrylate) composite films. *Journal of applied polymer science*, 112(1):142–156, 2009.

[42] Ebrahim Najafi and Kwanwoo Shin. Radiation resistant polymer–carbon nanotube nanocomposite thin films. *Colloids and Surfaces A: Physicochemical and Engineering Aspects*, 257:333–337, 2005.

[43] Sheila A Thibeault, Jin Ho Kang, Godfrey Sauti, Cheol Park, Catharine C Fay, and Glen C King. Nanomaterials for radiation shielding. *Mrs Bulletin*, 40(10): 836–841, 2015.

[44] JA Simpson. Composition and origin of cosmic rays. *Mathematical and Physical Sciences*, 107, 1983.

[45] Lawrence W Townsend. Implications of the space radiation environment for human exploration in deep space. *Radiation protection dosimetry*, 115(1-4):44–50, 2005.

[46] David Berghmans, RAM Van der Linden, Petra Vanlommel, René Warnant, Andrej Zhukov, Eva Robbrecht, Frédéric Clette, O Podladchikova, B Nicula, J-F Hochedez, et al. Solar activity: nowcasting and forecasting at the sidc. In *Annales Geophysicae*, volume 23, pages 3115–3128. Copernicus GmbH, 2005.

[47] Kenneth A LaBel et al. Single event effect criticality analysis. *NASA Headquar-ters/Code QW*, 1996.

[48] Rainer Schwenn. Space weather: The solar perspective. *Living reviews in solar physics*, 3(1):1–72, 2006.

[49] Kristina Rojdev, Steven Koontz, Brandon Reddell, William Atwell, and Paul Boeder. Comparison and validation of fluka and hzetrn as tools for investigat-ing the secondary neutron production in large space vehicles. In *AIAA SPACE 2015 Conference and Exposition*, page 4601, 2015.

[50] Mihail P Petkov. The effects of space environments on electronic components. 2003.

[51] TV Kuznetsova. Long-term spectral components of global, north and south hemi-sphere temperatures over the last millennium and solar-lunar forcing. *Journal of Atmospheric and Solar-Terrestrial Physics*, 211:105393, 2020.

[52] Gerald J Dittberner, Andrew J Gerber Jr, David M Tralli, and Shyam N Bajpai. Medium earth orbit (meo) as a venue for future noaa satellite systems. In *Proceed-ings of the EUMETSAT Meteorological Satellite Conference, Dubrovnik*. Citeseer, 2005.

[53] Mohamed Henini. *Handbook of self assembled semiconductor nanostructures for novel devices in photonics and electronics*. Elsevier, 2011.

[54] Eric R Benton and EV Benton. Space radiation dosimetry in low-earth orbit and beyond. *Nuclear Instruments and Methods in Physics Research Section B: Beam Interactions with Materials and Atoms*, 184(1-2):255–294, 2001.

[55] Lyndon B Johnson Space Center. Advanced life support requirements document. 2002.

[56] Matthew J Beck, Blair R Tuttle, Ronald D Schrimpf, Daniel M Fleetwood, and Sokrates T Pantelides. Atomic displacement effects in single-event gate rupture. *IEEE Transactions on Nuclear Science*, 55(6):3025–3031, 2008.

[57] Raoul Velazco, Pascal Fouillat, and Ricardo Reis. *Radiation effects on embedded systems*. Springer Science & Business Media, 2007.

[58] Laurence R Young and Jeffrey P Sutton. *Handbook of Bioastronautics*. Springer, 2021.

[59] Yuli Li, Wenxian Wang, Jun Zhou, Hongsheng Chen, and Peng Zhang. 10b areal density: A novel approach for design and fabrication of b4c/6061al neutron ab-sorbing materials. *Journal of Nuclear Materials*, 487:238–246, 2017.

[60] Wayne D Newhauser and Rui Zhang. The physics of proton therapy. *Physics in Medicine & Biology*, 60(8):R155, 2015.

[61] Indiana EDU. Interactions of radiation with matter, 2016. URL http://courses.chem.indiana.edu/c460/documents/SEC5-InteractionsofRadiationwithMatter_000.pdf.

[62] Oregan State EDU. Chapter 17 interaction of radiation with matter., 2015. URL http://oregonstate.edu/instruct/ch374/ch418518/Chapter%2017%20Interaction%20of%20Radiation%20with%20Matter-rev.pdf.

[63] Anshu Saxena, Hemlata Singh, Priyanka Agrawal, SK Rathi, and AS Verma. Stopping power of electrons and positrons for c, al, cu, ag, au, pb, fe, u, ge, si and mo. *Applied Physics Research*, 2(2):176, 2010.

[64] Jamaliah Sharif, Wan Md Zin Wan Yunus, Khairul Zaman Hj Mohd Dahlan, and Mansor Hj Ahmad. Preparation and properties of radiation crosslinked natural rubber/clay nanocomposites. *Polymer Testing*, 24(2):211–217, 2005.

[65] Neal Jay Carron. *An introduction to the passage of energetic particles through matter.* Taylor & Francis, 2006.

[66] K Muraleedhara Varier. *Nuclear radiation detection, measurements and analysis.* Alpha Science International Limited, 2009.

[67] Bernard M Rabin, Kirsty L Carrihill-Knoll, and Barbara Shukitt-Hale. Operant responding following exposure to hze particles and its relationship to particle energy and linear energy transfer. *Advances in Space Research*, 48(2):370–377, 2011.

[68] Suraj P Rawal. Metal-matrix composites for space applications. *Jom*, 53(4):14–17, 2001.

[69] Andrew J Piekutowski, KL Poormon, Eric L Christiansen, and Bruce A Davis. Performance of whipple shields at impact velocities above 9 km/s. *International Journal of Impact Engineering*, 38(6):495–503, 2011.

[70] EL Christiansen, Crews-NASA Johnson, JE Williamsen, JH Robinson, and Nolen-NASA Marshall AM. 3m nextel ceramic fabric offers space age protection. *Intl. Journal of Impact Engineering*, 17.

[71] Physics Forums. Heat dissipation in space., 2010. URL http://www.physicsforums.com/showthread.php?t=399450.

[72] Lionel Fabian Fourie and Lynndle Square. Determination of a safe distance for atomic hydrogen depositions in hot-wire chemical vapour deposition by means of cfd heat transfer simulations. *Fluid Dynamic and Materials Processing*, 2020.

[73] A Majumdar et al. Microscale transport phenomena, 1998.

[74] Hyper Physics. Chemical bonds, 2020. URL http://hyperphysics.phy-astr.gsu.edu/hbase/chemical/bond.html.

[75] Kenneth D Fourspring, Zoran Ninkov, Bryan C Fodness, Massimo Robberto, Sally Heap, and Alex G Kim. Proton radiation testing of digital micromirror devices for space applications. *Optical Engineering*, 52(9):091807, 2013.

[76] Juan Antonio Asensio, Salvador Borrós, and Pedro Gómez-Romero. Proton-conducting polymers based on benzimidazoles and sulfonated benzimidazoles. *Journal of Polymer Science Part A: Polymer Chemistry*, 40(21):3703–3710, 2002.

[77] P Gomez-Romero, JA Asensio, and EM Sanchez. Proton-conducting membranes based on benzimidazole polymers for high-temperature pem fuel cells. a chemical quest. *Chem. Soc. Rev.*, 39:3210–3239, 2010.

[78] Ram K Tripathi. Meeting the grand challenge of protecting astronauts health: Electrostatic active space radiation shielding for deep space missions. Technical report, 2016.

[79] Wolfgang Kaiser. *Kunststoffchemie für Ingenieure: von der Synthese bis zur Anwendung*. Carl Hanser Verlag GmbH Co KG, 2021.

[80] Andreas Borggräfe, Michael Quatmann, and Daniel Nölke. Radiation protective structures on the base of a case study for a manned mars mission. *Acta Astronautica*, 65(9-10):1292–1305, 2009.

[81] MIT EDU. Material property database-polyimide., 2004. URL http://www.mit.edu/~6.777/matprops/polyimide.htm.

[82] Dennis B Malpass. *Introduction to industrial polyethylene: properties, catalysts, and processes*. John Wiley & Sons, 2010.

[83] Henri Ulrich. *Introduction to industrial polymers*. Hanser Munich, 1982.

[84] S Guetersloh, Cary Zeitlin, L Heilbronn, Jack Miller, Tatsudo Komiyama, A Fukumura, Y Iwata, T Murakami, and M Bhattacharya. Polyethylene as a radiation shielding standard in simulated cosmic-ray environments. *Nuclear Instruments and Methods in Physics Research Section B: Beam Interactions with Materials and Atoms*, 252(2):319–332, 2006.

[85] MR Shavers, N Zapp, RE Barber, JW Wilson, G Qualls, L Toupes, S Ramsey, V Vinci, G Smith, and FA Cucinotta. Implementation of alara radiation protection on the iss through polyethylene shielding augmentation of the service module crew quarters. *Advances in Space Research*, 34(6):1333–1337, 2004.

[86] Francis A Cucinotta, Myung-Hee Y Kim, and Lei Ren. Evaluating shielding effectiveness for reducing space radiation cancer risks. *Radiation Measurements*, 41 (9-10):1173–1185, 2006.

[87] Andrew Bruce Bocarsly and EV Niangar. Fuel cells-proton-exchange membrane fuel cells— membranes: Elevated temperature. In *Encyclopedia of Electrochemical Power Sources*, pages 724–733. Elsevier, 2009.

[88] Amit Bhattacharya. Radiation and industrial polymers. *Progress in polymer science*, 25(3):371–401, 2000.

[89] Courtney Harrison, Sean Weaver, Craig Bertelsen, Eric Burgett, Nolan Hertel, and Eric Grulke. Polyethylene/boron nitride composites for space radiation shielding. *Journal of applied polymer science*, 109(4):2529–2538, 2008.

[90] Pulickel M Ajayan. Bulk metal and ceramics nanocomposites. *Nanocomposite science and technology*, pages 1–75, 2003.

[91] M Samaras, PM Derlet, H Van Swygenhoven, and M Victoria. Radiation damage near grain boundaries. *Philosophical magazine*, 83(31-34):3599–3607, 2003.

[92] Y Chimi, A Iwase, N Ishikawa, M Kobiyama, T Inami, and S Okuda. Accumulation and recovery of defects in ion-irradiated nanocrystalline gold. *Journal of Nuclear Materials*, 297(3):355–357, 2001.

[93] Y Chimi, A Iwase, N Ishikawa, M Kobiyama, T Inami, T Kambara, and S Okuda. Swift heavy ion irradiation effects in nanocrystalline gold. *Nuclear Instruments and Methods in Physics Research Section B: Beam Interactions with Materials and Atoms*, 245(1):171–175, 2006.

[94] MIT EDU. Introduction to crystallography., 2014. URL https://ocw.mit.edu/courses/materials-science-and-engineering/3-091sc-introduction-to-solid-state-chemistry-fall-2010/crystalline-materials/15-introduction-to-crystallography/.

[95] WH Zhong, G Sui, S Jana, and J Miller. Cosmic radiation shielding tests for uhmwpe fiber/nano-epoxy composites. *Composites Science and Technology*, 69 (13):2093–2097, 2009.

[96] Minoru Okamoto, Tsuyohiko Fujigaya, and Naotoshi Nakashima. Individual dissolution of single-walled carbon nanotubes by using polybenzimidazole, and highly effective reinforcement of their composite films. *Advanced functional materials*, 18 (12):1776–1782, 2008.

[97] ES Choi, JS Brooks, DL Eaton, MS Al-Haik, MY Hussaini, H Garmestani, D Li, and K Dahmen. Enhancement of thermal and electrical properties of carbon nanotube polymer composites by magnetic field processing. *Journal of Applied physics*, 94(9):6034–6039, 2003.

[98] Amy M Marconnet, Namiko Yamamoto, Matthew A Panzer, Brian L Wardle, and Kenneth E Goodson. Thermal conduction in aligned carbon nanotube–polymer nanocomposites with high packing density. *ACS nano*, 5(6):4818–4825, 2011.

[99] Peter J Boul, Kathryn Turner, Jing Li, Merlyn X Pulikkathara, RC Dwivedi, Edward D Sosa, Yijiang Lu, Oleksandr V Kuznetsov, Padraig Moloney, R Wilkins, et al. Single wall carbon nanotube response to proton radiation. *The Journal of Physical Chemistry C*, 113(32):14467–14473, 2009.

[100] PP Neupane, MO Manasreh, BD Weaver, RP Rafaelle, and BJ Landi. Proton irradiation effect on single-wall carbon nanotubes in a poly (3-octylthiophene) matrix. *Applied Physics Letters*, 86(22):221908, 2005.

[101] Vladimir A Basiuk, Kensei Kobayashi, Takeo Kaneko, Yoichi Negishi, Elena V Basiuk, and José-Manuel Saniger-Blesa. Irradiation of single-walled carbon nanotubes with high-energy protons. *Nano Letters*, 2(7):789–791, 2002.

[102] S Mathew, TK Chan, D Zhan, K Gopinadhan, A-R Barman, MBH Breese, S Dhar, ZX Shen, T Venkatesan, and John TL Thong. The effect of layer number and substrate on the stability of graphene under mev proton beam irradiation. *Carbon*, 49(5):1720–1726, 2011.

[103] Rob H Telling, Chris P Ewels, Ahlam A El-Barbary, and Malcolm I Heggie. Wigner defects bridge the graphite gap. *Nature materials*, 2(5):333–337, 2003.

[104] AV Krasheninnikov and FJNM Banhart. Engineering of nanostructured carbon materials with electron or ion beams. *Nature materials*, 6(10):723–733, 2007.

[105] MA Ortiz-Zarama, BH Camacho-Diaz, AR Jiménez-Aparicio, and J Solorza-Feria. Effect of sodium dodecyl sulfate on the physical properties of gelatin/multi-walled carbon nanotubes solutions and films. *Revista Mexicana de Ingeniería Química*, 16(1):307–319, 2017.

[106] Suchismita Ghosh, Wenzhong Bao, Denis L Nika, Samia Subrina, Evghenii P Pokatilov, Chun Ning Lau, and Alexander A Balandin. Dimensional crossover of thermal transport in few-layer graphene. *Nature materials*, 9(7):555–558, 2010.

[107] S Mathew, UM Bhatta, J Ghatak, BR Sekhar, and BN Dev. The effects of 2 mev ag ion irradiation on multiwalled carbon nanotubes. *Carbon*, 45(13):2659–2664, 2007.

[108] S Mathew, B Joseph, BR Sekhar, and BN Dev. X-ray photoelectron and raman spectroscopic studies of mev proton irradiated graphite. *Nuclear Instruments and Methods in Physics Research Section B: Beam Interactions with Materials and Atoms*, 266(14):3241–3246, 2008.

[109] Zhenhao Li, Siyuan Chen, Shruti Nambiar, Yonghai Sun, Mingyu Zhang, Wanping Zheng, and John TW Yeow. Pmma/mwcnt nanocomposite for proton radiation shielding applications. *Nanotechnology*, 27(23):234001, 2016.

[110] Wen Cai, Qi Chen, Nerine Cherepy, Alex Dooraghi, David Kishpaugh, Arion Chatziioannou, Stephen Payne, Weidong Xiang, and Qibing Pei. Synthesis of bulk-size transparent gadolinium oxide–polymer nanocomposites for gamma ray spectroscopy. *Journal of Materials Chemistry C*, 1(10):1970–1976, 2013.

[111] Ş Gözde İrim, Abdulmounem Alchekh Wis, M Aker Keskin, Oktay Baykara, Guralp Ozkoc, Ahmet Avcı, Mahmut Doğru, and Mesut Karakoc. Physical, mechanical and neutron shielding properties of h-bn/gd2o3/hdpe ternary nanocomposites. *Radiation Physics and Chemistry*, 144:434–443, 2018.

[112] Sigma-Aldrich. Alddrich. gadolinium(iii) oxide., 2022. URL `//www.sigmaaldrich.com/catalog/product/aldrich/637335?lang=en&region=CA`.

[113] Sigma-Aldrich. Alddrich. bismuth(iii) oxide., 2022. URL `//www.sigmaaldrich.com/catalog/product/aldrich/637017?lang=en&region=CA`.

[114] Chen-Feng Kuan, Hsu-Chiang Kuan, Chen-Chi M Ma, and Chia-Hsun Chen. Mechanical and electrical properties of multi-wall carbon nanotube/poly (lactic acid) composites. *Journal of Physics and Chemistry of Solids*, 69(5-6):1395–1398, 2008.

[115] Zdenko Spitalsky, Dimitrios Tasis, Konstantinos Papagelis, and Costas Galiotis. Carbon nanotube–polymer composites: chemistry, processing, mechanical and electrical properties. *Progress in polymer science*, 35(3):357–401, 2010.

[116] Shin-Yi Yang, Wei-Ning Lin, Yuan-Li Huang, Hsi-Wen Tien, Jeng-Yu Wang, Chen-Chi M Ma, Shin-Ming Li, and Yu-Sheng Wang. Synergetic effects of graphene platelets and carbon nanotubes on the mechanical and thermal properties of epoxy composites. *Carbon*, 49(3):793–803, 2011.

[117] Shantanu Bhowmik and R Benedictus. Performance of space durable polymeric nano composite under electromagnetic radiation at low earth orbit. *2007 IEEE Applied Electromagnetics Conference (AEMC)*, pages 1–4, 2007.

[118] SL Ruan, Ping Gao, Xin G Yang, and TX Yu. Toughening high performance ultra-high molecular weight polyethylene using multiwalled carbon nanotubes. *Polymer*, 44(19):5643–5654, 2003.

[119] G Williams, R Trask, and I Bond. A self-healing carbon fibre reinforced polymer for aerospace applications. *Composites Part A: Applied Science and Manufacturing*, 38(6):1525–1532, 2007.

[120] Huasi Hu, Qunshu Wang, Juan Qin, Yuelei Wu, Tiankui Zhang, Zhongsheng Xie, Xinbiao Jiang, Guoguang Zhang, Hu Xu, Xiangyang Zheng, et al. Study on composite material for shielding mixed neutron and gamma-rays. *IEEE Transactions on Nuclear Science*, 55(4):2376–2384, 2008.

[121] Cheol Park, Zoubeida Ounaies, Kent A Watson, Kristin Pawlowski, Sharon E Lowther, John W Connell, Emilie J Siochi, Joycelyn S Harrison, and Terry L St Clair. Polymer-single wall carbon nanotube composites for potential spacecraft applications. *MRS Online Proceedings Library (OPL)*, 706, 2001.

[122] Motoo Fujii, Xing Zhang, Huaqing Xie, Hiroki Ago, Koji Takahashi, Tatsuya Ikuta, Hidekazu Abe, and Tetsuo Shimizu. Measuring the thermal conductivity of a single carbon nanotube. *Physical review letters*, 95(6):065502, 2005.

[123] Yonggang Zou, Guojun Liu, Lin Li, Zhanguo Li, and Mei Li. Carbon nanotubes and thermal properties. In *2010 Academic Symposium on Optoelectronics and Microelectronics Technology and 10th Chinese-Russian Symposium on Laser Physics and Laser TechnologyOptoelectronics Technology (ASOT)*, pages 72–75. IEEE, 2010.

[124] Alexander A Balandin, Suchismita Ghosh, Wenzhong Bao, Irene Calizo, Desalegne Teweldebrhan, Feng Miao, and Chun Ning Lau. Superior thermal conductivity of single-layer graphene. *Nano letters*, 8(3):902–907, 2008.

[125] Aiping Yu, Palanisamy Ramesh, Xiaobo Sun, Elena Bekyarova, Mikhail E Itkis, and Robert C Haddon. Enhanced thermal conductivity in a hybrid graphite nanoplatelet–carbon nanotube filler for epoxy composites. *Advanced Materials*, 20(24):4740–4744, 2008.

[126] Reto Haggenmueller, Csaba Guthy, Jennifer R Lukes, John E Fischer, and Karen I Winey. Single wall carbon nanotube/polyethylene nanocomposites: thermal and electrical conductivity. *Macromolecules*, 40(7):2417–2421, 2007.

[127] Hongliang Zhong and Jennifer R Lukes. Interfacial thermal resistance between carbon nanotubes: Molecular dynamics simulations and analytical thermal modeling. *Physical Review B*, 74(12):125403, 2006.

[128] Hyoung-Juhn Kim, Sung Yong Cho, Sung Jin An, Yeong Chan Eun, Ju-Yong Kim, Hae-Kwon Yoon, Ho-Jin Kweon, and Kyoung Han Yew. Synthesis of poly

(2, 5-benzimidazole) for use as a fuel-cell membrane. *Macromolecular rapid communications*, 25(8):894–897, 2004.

[129] Juan Antonio Asensio and P Gómez-Romero. Recent developments on proton conduc-ting poly (2, 5-benzimidazole)(abpbi) membranes for high temperature poly-mer electrolyte membrane fuel cells. *Fuel Cells*, 5(3):336–343, 2005.

[130] Juan Antonio Asensio, Salvador Borrós, and Pedro Gómez-Romero. Proton-conducting membranes based on poly (2, 5-benzimidazole)(abpbi) and phosphoric acid prepared by direct acid casting. *Journal of Membrane Science*, 241(1):89–93, 2004.

[131] Liliana A Diaz, Graciela C Abuin, and Horacio R Corti. Water and phosphoric acid uptake of poly [2, 5-benzimidazole](abpbi) membranes prepared by low and high temperature casting. *Journal of Power Sources*, 188(1):45–50, 2009.

[132] Sung-Kon Kim, Tae-Ho Kim, Jung-Woo Jung, and Jong-Chan Lee. Polybenzimidazole containing benzimidazole side groups for high-temperature fuel cell applications. *Polymer*, 50(15):3495–3502, 2009.

[133] Palanichamy Krishnan, Jin-Soo Park, and Chang-Soo Kim. Performance of a poly (2, 5-benzimidazole) membrane based high temperature pem fuel cell in the presence of carbon monoxide. *Journal of Power Sources*, 159(2):817–823, 2006.

[134] JA Asensio, S Borros, and P Gomez-Romero. Batteries, fuel cells, and energy conversion-polymer electrolyte fuel cells based on phosphoric acid-impregnated poly (2, 5-benzimidazole) membranes. *Journal of the Electrochemical Society*, 151 (2):A304, 2004.

[135] Qingting Liu. *Poly (2, 5-benzimidazole) based polymer electrolyte membranes for high temperature fuel cell applications*. PhD thesis, Loughborough University, 2010.

[136] José J Linares, Cassandra Sánches, Valdecir Antônio Paganin, and Ernesto R González. Poly (2, 5-benzimidazole) membranes: physico-chemical characterization and high temperature pemfc application. *ECS Transactions*, 41(1):1579, 2011.

[137] Jose J Linares, Cassandra Sanches, Valdecir A Paganin, and Ernesto R Gonzalez. Poly (2, 5-bibenzimidazole) membranes: physico-chemical characterization focused on fuel cell applications. *Journal of The Electrochemical Society*, 159(7):F194, 2012.

[138] Jaedong Cho, John Blackwell, Sergei N Chvalun, Morton Litt, and Yuan Wang. Structure of a poly (2, 5-benzimidazole)/phosphoric acid complex. *Journal of Polymer Science Part B: Polymer Physics*, 42(13):2576–2585, 2004.

[139] Liliana A Diaz, Graciela C Abuin, and Horacio R Corti. Acid-doped abpbi membranes prepared by low-temperature casting: Proton conductivity and water uptake properties compared with other polybenzimidazole-based membranes. *Journal of The Electrochemical Society*, 163(6):F485, 2016.

[140] Federico Viva, Nayra Heredia, Sofia Pagani Palmbaum, Liliana Diaz, Juan De Diego, Matias Lozano, Mariano Bruno, and Horacio Corti. Spray-casting abpbi membranes for high temperature pem fuel cells. *Journal of The Electrochemical Society*, 164(7):F866, 2017.

[141] Wolf Vielstich, Arnold Lamm, and Hubert Gasteiger. Handbook of fuel cells. fundamentals, technology, applications. 2003.

[142] Ratikanta Nayak, Tapobrata Dey, Prakash C Ghosh, and Arup R Bhattacharyya. Phosphoric acid doped poly (2, 5-benzimidazole)-based proton exchange membrane for high temperature fuel cell application. *Polymer Engineering & Science*, 56(12):1366–1374, 2016.

[143] Harshal D Chaudhari, Rajith Illathvalappil, Sreekumar Kurungot, and Ulhas K Kharul. Preparation and investigations of abpbi membrane for ht-pemfc by immersion precipitation method. *Journal of Membrane Science*, 564:211–217, 2018.

[144] Ftir analysis, 2022. URL https://rtilab.com/techniques/ftir-analysis/.

[145] Siyuan Chen. Polymer based nanocomposites as multifunctional structure for space radiation shielding: A study of nanomaterial fabrications and evaluations. 2018.

[146] Peer reviewed scientific video journal - methods and protocols. URL https://www.jove.com/science-education/10446/x-ray-diffraction.

[147] Portland state university lecture on xrd, 2016. URL https://web.pdx.edu/~pmoeck/phy381/Topic5a-XRD.pdf.

[148] Angel Ochoa Brezmes and Cornelia Breitkopf. Fast and reliable simulations of argon inductively coupled plasma using comsol. *Vacuum*, 116:65–72, 2015.

[149] S-B Wang and AE Wendt. Ion bombardment energy and sio 2/si fluorocarbon plasma etch selectivity. *Journal of Vacuum Science & Technology A: Vacuum, Surfaces, and Films*, 19(5):2425–2432, 2001.

[150] Hyo-Chang Lee, Jin-Young Bang, and Chin-Wook Chung. Effects of rf bias power on electron energy distribution function and plasma uniformity in inductively coupled argon plasma. *Thin Solid Films*, 519(20):7009–7013, 2011.

[151] Charles K Birdsall and A Bruce Langdon. *Plasma physics via computer simulation.* CRC press, 2018.

[152] Christophe De Bie, Bert Verheyde, Tom Martens, Jan van Dijk, Sabine Paulussen, and Annemie Bogaerts. Fluid modeling of the conversion of methane into higher hydrocarbons in an atmospheric pressure dielectric barrier discharge. *Plasma Processes and Polymers*, 8(11):1033–1058, 2011.

[153] Dimitris P Lymberopoulos and Demetre J Economou. Two-dimensional self-consistent radio frequency plasma simulations relevant to the gaseous electronics conference rf reference cell. *Journal of research of the National Institute of Standards and Technology*, 100(4):473, 1995.

[154] HC Kim, Felipe Iza, SS Yang, M Radmilović-Radjenović, and JK Lee. Particle and fluid simulations of low-temperature plasma discharges: benchmarks and kinetic effects. *Journal of Physics D: Applied Physics*, 38(19):R283, 2005.

[155] Mark J Kushner. Hybrid modelling of low temperature plasmas for fundamental investigations and equipment design. *Journal of Physics D: Applied Physics*, 42 (19):194013, 2009.

[156] Cheng Jia, Ji Linhong, Zhu Yu, and Shi Yixiang. Fluid model of inductively coupled plasma etcher based on comsol. *Journal of Semiconductors*, 31(3):032004, 2010.

[157] Yoshinori Takao, Kenji Matsuoka, Koji Eriguchi, and Kouichi Ono. Pic-mcc simulations of capacitive rf discharges for plasma etching. In *AIP Conference Proceedings*, volume 1333, pages 1051–1056. American Institute of Physics, 2011.

[158] TH Chung, HS Yoon, and JK Lee. Scaling laws verification for capacitive rf-discharge ar plasma using particle-in-cell simulations. *Journal of applied physics*, 78(11):6441–6447, 1995.

[159] Hyung-Yong Kim, Deuk-Chul Kwon, Nam-Sik Yoon, Hee-Hwan Choe, and Jung-Hyung Kim. Development of new method for fluid simulation of capacitively coupled plasma discharge. *Journal of the Korean Physical Society*, 49(5):1967, 2006.

[160] Balaji Jayaraman and Wei Shyy. Modeling of dielectric barrier discharge-induced fluid dynamics and heat transfer. *Progress in Aerospace Sciences*, 44(3):139–191, 2008.

[161] Uwe Kortshagen and Brian G Heil. Kinetic two-dimensional modeling of inductively coupled plasmas based on a hybrid kinetic approach. *IEEE transactions on plasma science*, 27(5):1297–1309, 1999.

[162] CCR Technology. Corpa gte plasma beam source user manual.

[163] BOLSIG. Boltzmann solver for the siglo series 1.0 cpa toulouse kinema software, 1996.

[164] Angel Ochoa Brezmes and Cornelia Breitkopf. Simulation of inductively coupled plasma with applied bias voltage using comsol. *Vacuum*, 109:52–60, 2014.

[165] Babak Shokri, Maziar S Yaghmaee, and Abdollah Sarani. On the plasma chemistry of ch4 h2 ar system relevant to diamond deposition process by plasma enhanced chemical vapor deposition. *Plasma Processes and Polymers*, 6(S1):S450–S457, 2009.

[166] S Rebiai, H Bahouh, and S Sahli. 2-d simulation of dual frequency capacitively coupled helium plasma, using comsol multiphysics. *IEEE Transactions on Dielectrics and Electrical Insulation*, 20(5):1616–1624, 2013.

[167] J-P Boeuf. Numerical model of rf glow discharges. *Physical review A*, 36(6):2782, 1987.

[168] GJM Hagelaar and L C Pitchford. Solving the boltzmann equation to obtain electron transport coefficients and rate coefficients for fluid models. *Plasma sources science and technology*, 14(4):722, 2005.

[169] COMSOL. Comsol 4.4 userbook (user), . URL https://comsol.com.

[170] COMSOL. Comsol 4.3 gec icp reactor, argon/oxygen chemistry, . URL https://comsol.com.

[171] A. Pahl. Electron energy distribution function., 2014. URL https://www.comsol.com/blogs/electron-energy-distribution-function/.

[172] VA Godyak, RB Piejak, and BM Alexandrovich. Electron energy distribution function measurements and plasma parameters in inductively coupled argon plasma. *Plasma Sources Science and Technology*, 11(4):525, 2002.

[173] EV Stenson, J Horn-Stanja, MR Stoneking, and T Sunn Pedersen. Debye length and plasma skin depth: two length scales of interest in the creation and diagnosis of laboratory pair plasmas. *Journal of Plasma Physics*, 83(1), 2017.

[174] Thomas Keller. Recent all-composite and hybrid fibre-reinforced polymer bridges and buildings. *Progress in Structural Engineering and Materials*, 3(2):132–140, 2001.

[175] Suprakas Sinha Ray and Masami Okamoto. Polymer/layered silicate nanocomposites: a review from preparation to processing. *Progress in polymer science*, 28 (11):1539–1641, 2003.

[176] Anna C Balazs, Todd Emrick, and Thomas P Russell. Nanoparticle polymer composites: where two small worlds meet. *Science*, 314(5802):1107–1110, 2006.

[177] T Ramanathan, AA Abdala, S Stankovich, DA Dikin, M Herrera-Alonso, RD Piner, DH Adamson, HC Schniepp, XRRS Chen, RS Ruoff, et al. Functionalized graphene sheets for polymer nanocomposites. *Nature nanotechnology*, 3 (6):327–331, 2008.

[178] Ji-Ye Kang, Soo-Mi Eo, In-Yup Jeon, Yeong Suk Choi, Loon-Seng Tan, and Jong-Beom Baek. Multifunctional poly (2, 5-benzimidazole)/carbon nanotube composite films. *Journal of Polymer Science Part A: Polymer Chemistry*, 48(5):1067–1078, 2010.

[179] Yi-Cheng Chiang, Dah-Shyang Tsai, Yen-Heng Liu, and Chun-Wei Chiang. Pem fuel cells of poly (2, 5-benzimidazole) abpbi membrane electrolytes doped with phosphoric acid and metal phosphates. *Materials Chemistry and Physics*, 216: 485–490, 2018.

[180] Enrique M Jackson, Paul E Laibinis, Warren E Collins, Akira Ueda, Charles D Wingard, and Benjamin Penn. Development and thermal properties of carbon nanotube-polymer composites. *Composites Part B: Engineering*, 89:362–373, 2016.

[181] A Almajid, L Sorochynska, K Friedrich, and B Wetzel. Effects of graphene and cnt on mechanical, thermal, electrical and corrosion properties of vinylester based nanocomposites. *Plastics, Rubber and Composites*, 44(2):50–62, 2015.

[182] Ketan S Khare, Fardin Khabaz, and Rajesh Khare. Effect of carbon nanotube functionalization on mechanical and thermal properties of cross-linked epoxy–carbon nanotube nanocomposites: role of strengthening the interfacial interactions. *ACS applied materials & interfaces*, 6(9):6098–6110, 2014.

[183] P Musto, FE Karasz, and WJ MacKnight. Fourier transform infra-red spectroscopy on the thermo-oxidative degradation of polybenzimidazole and of a polybenzimidazole/polyetherimide blend. *Polymer*, 34(14):2934–2945, 1993.

[184] Anthony Wereta Jr, Matatjahu T Gehatia, and Donald R Wiff. Morphological and physical property effects for solvent cast films of poly-2, 5 (6) benzimidazole. *Polymer Engineering & Science*, 18(3):204–209, 1978.

[185] Shanfeng Wang, Gaobin Bao, Zhibao Lu, Pingping Wu, and Zhewen Han. Effect of heat treatment on the structure and properties of poly (2, 6-benzothiazole)(abpbt) and poly (2, 5-benzoxazole)(abpbo). *Journal of materials science*, 35(23):5873–5877, 2000.

[186] Xiaoxiao Zhang, Qingting Liu, Lei Xia, Dongyang Huang, Xudong Fu, Rong Zhang, Shengfei Hu, Feng Zhao, Xiao Li, and Xujin Bao. Poly (2, 5-benzimidazole)/sulfonated sepiolite composite membranes with low phosphoric acid doping levels for pemfc applications in a wide temperature range. *Journal of membrane science*, 574:282–298, 2019.

[187] Juan Antonio Asensio, Salvador Borrós, and Pedro Gómez-Romero. Polymer electrolyte fuel cells based on phosphoric acid-impregnated poly (2, 5-benzimidazole) membranes. *Journal of the electrochemical society*, 151(2):A304, 2004.

[188] W H Hall. X-ray line broadening in metals. *Proceedings of the Physical Society. Section A*, 62(11):741, nov 1949. doi: 10.1088/0370-1298/62/11/110. URL https://dx.doi.org/10.1088/0370-1298/62/11/110.

[189] M Raja Reddy. Effect of low earth orbit atomic oxygen on spacecraft materials. *Journal of Materials Science*, 30(2):281–307, 1995.

[190] Timothy C May and Murray H Woods. A new physical mechanism for soft errors in dynamic memories. In *16th International Reliability Physics Symposium*, pages 33–40. IEEE, 1978.

[191] Shruti Nambiar and John TW Yeow. Polymer-composite materials for radiation protection. *ACS applied materials & interfaces*, 4(11):5717–5726, 2012.

[192] William Atwell, Kristina Rojdev, Daniel Liang, and Matthew Hill. Metal hydrides, mofs, and carbon composites as space radiation shielding mitigators. 2014.

[193] James F Ziegler, Matthias D Ziegler, and Jochen P Biersack. Srim–the stopping and range of ions in matter (2010). *Nuclear Instruments and Methods in Physics Research Section B: Beam Interactions with Materials and Atoms*, 268(11-12):1818–1823, 2010.

[194] Guanghai Liu, Laifei Cheng, and Xingang Luan. Radiation damage behavior of carbon/carbon composite in low earth orbit environment. *Ceramics International*, 45(13):16088–16096, 2019.

[195] Penghui Cao, Kang Pyo So, Yang Yang, Jong Gil Park, Mingda Li, Long Yan, Jing Hu, Mark Kirk, Meimei Li, Young Hee Lee, et al. Carbon nanotube (cnt)

metal composites exhibit greatly reduced radiation damage. *Acta Materialia*, 203: 116483, 2021.

[196] K Sahre, K-J Eichhorn, F Simon, D Pleul, A Janke, and G Gerlach. Characterization of ion-beam modified polyimide layers. *Surface and Coatings Technology*, 139(2-3):257–264, 2001.

[197] Manasvi Dixit, Deepika, Mahesh Baboo, Kananbala Sharma, NS Saxena, DK Avasthi, and Pawan K Kulriya. Effect of 50 mev li+ 3 ion beam irradiation on thermomechanical properties of pmma/pc blend films. *International Journal of Polymeric Materials*, 59(11):873–890, 2010.

[198] Koshi Takenaka and Masayoshi Ichigo. Thermal expansion adjustable polymer matrix composites with giant negative thermal expansion filler. *Composite Science and Technology*, pages 47–51, 2014.